Hall A Status Report - 2002

Edited by Eric Voutier and Kees de Jager

December 2002

Contents

1 Introduction **15**

2 Standard Hall A Facilities **19**
2.1 Beam Line . . . 19
2.1.1 Compton Polarimeter . . . 19
2.2 Target . . . 23
2.2.1 Status Report on the Cryogenic Target . . . 23
2.2.2 Hall A Bremsstrahlung Radiator Status Report . . . 24
2.2.3 Status Report on the Polarized ^{3}He Target . . . 25
2.3 Spectrometers . . . 28
2.3.1 Spectrometer High Resolution Test . . . 28
2.3.2 High Resolution Trigger Counter S2m . . . 31
2.3.3 HRS Optics News . . . 35
2.4 Data Handling . . . 36
2.4.1 Hall A Analysis Software . . . 36
2.4.2 MCEEP . . . 40
2.4.3 SIMC . . . 46

3 Specific Instrumental Developments **51**
3.1 Operational Systems . . . 51
3.1.1 Dual Analyzer in Hall A FPP . . . 51
3.1.2 RCS Calorimeter Performance and Future Applications . . . 52
3.1.3 The Hall A RICH Detector . . . 58
3.2 Detector Developments . . . 65
3.2.1 BigBite Spectrometer . . . 65
3.2.2 The DVCS/E00-110 Experimental Setup . . . 67
3.2.3 Preparations for Hall A Parity-Violation Experiments . . . 73
3.3 Software Developments . . . 80
3.3.1 Software for High Voltage Control . . . 80
3.4 Look Into Future . . . 81
3.4.1 Medium Acceptance Device . . . 81

4 Summaries of Experimental Activities **87**
4.1 Experiment E89-028 . . . 87
4.2 Experiment E89-044 . . . 90
4.3 Experiment E91-011 . . . 93
4.4 Experiment E93-049 . . . 98
4.5 Experiment E93-050 . . . 101
4.6 Experiment E94-010 . . . 105
4.7 Experiment E94-104 . . . 109
4.8 Experiment E97-103 . . . 112

4.9 Experiment E97-111 115
4.10 Experiment E98-108 116
4.11 Experiment E99-114 119
4.12 Experiment E99-117 121
4.13 Experiments E00-007 & E00-107 125
4.14 Experiment E00-102 127
4.15 Experiment E01-001 130
4.16 Experiment E01-020 133
4.17 The 12 GeV Upgrade 136

5 References **151**

6 Hall A Collaboration Member List **159**

7 Publications **167**
7.1 Journals 167
7.2 Hall A Internal Reports 167

8 Conferences **171**

9 Thesis **177**

List of Figures

1 Green points: Compton measurements for the A_1^n and g_2^n experiments. Only the statistical uncertainty is represented. Typical systematic errors of table1 must be added in quadrature. Blue points: rejected Compton measurements due to background or inconsistent calibration. Black points: Moller measurements, stat+syst error bars. 20

2 Example of electron analysis at 4 GeV. The 3 plots show the compton asymmetry versus strip number for each plane of the electron detector. Red, blue and green points correspond to left, right and off laser state respectively. 21

3 Polarized ^{3}He target performance during E99-117 and E97-103 26

4 Missing energy spectrum from the ^{12}C(e,e′p) reaction. A 4.7 GeV/c beam was used with an electron scattering angle of 16.1° and a hadron scattering angle of 45°. The electron momentum was 3.796 GeV/c and the hadron momentum was 1.489 GeV/c. The beam energy spread was determined to be approximately 5.0 × 10^{-5}. 28

5 Correlation between missing energy and trajectory angles (θ and ϕ) for left and right arms; flatness of the missing energy lines indicates the quality of the momentum reconstruction tensor D_{ijkl}. 29

6 Time-of-flight spectra in ^{16}O(e,e'p) experiment at large (negative) missing momenta (-410 MeV/c). The real coincidence peak at time of 170 ns has width of 1 ns. . . 32

7 Time-of-flight spectra in H(e,e′K) experiment. 32

8 The design of the S2m paddle. 33

9 Layout of the S2m plane. 33

10 The details of PMT housing. 34

11 Results obtained with the high-precision VDC tracking code for the reconstructed target quantities δ (momentum), y (in-plane position), θ (out-of-plane angle), and ϕ (in-plane angle). The data are from an optics study that used a 9-foil carbon target and the sieve slit collimator on the left HRS. More details can be found in the text. Black histograms are results from the C++ analyzer, and red (lighter colored) histograms were obtained with ESPACE. 37

12 Sieve slit pattern reconstructed with the C++ analyzer. The data are from the same run as those in Fig. 11. Only events originating from the center target foil ($|y_{tg}| < 0.01$) are included. 38

13 Sieve slit pattern reconstructed with ESPACE using the same analysis parameters as with Fig. 12. 39

14 Focal plane distributions for the electron (top) and proton (bottom) arms in H$(e, e'p)$. The coordinates refer to the standard Transport system which is the plane perpendicular to the central ray. The solid histograms are for the data and the dashed are for MCEEP using the **old** SNAKE based transfer functions. Note that some of the data distributions have been offset slightly to account for spectrometer misalignments. 41

15 Focal plane distributions for the electron (top) and proton (bottom) arms in H$(e, e'p)$. The coordinates refer to the standard Transport system which is the plane perpendicular to the central ray. The solid histograms are for the data and the dashed are for MCEEP using the **new** SNAKE based transfer functions. Note that some of the data distributions have been offset slightly to account for spectrometer misalignments. 42
16 Focal plane distributions for the electron (top) and proton (bottom) arms in H$(e, e'p)$. The coordinates refer to the standard Transport system which is the plane perpendicular to the central ray. The solid histograms are for the data and the dashed are for MCEEP using the recently implemented COSY model. Note that some of the data distributions have been offset slightly to account for spectrometer misalignments. 44
17 Distributions of the R-function values for the electron arm (top) and proton arm (bottom) for the old (dashed histogram) and new (dotted histogram) SNAKE based transfer functions, for the COSY model (dot-dashed histogram) and for the data (solid histogram). For the data, the updated R-functions were used. All results are for the 6.0 msr collimators. The data have been scaled by a factor of 1.11 to bring the integral into rough agreement with the simulations. 45
18 Ratio of the R-function distribution for each model to that of the data. The top panel shows the distributions for the electron arm and the bottom for the proton arm for the old (solid histogram) and new (dashed histogram) SNAKE based transfer functions and for the COSY model (dotted histogram). 45
19 Online, preliminary analyzing power data for e99-114. The top plot shows the analyzing power for CH_2 (carbon) versus scattering angle of the proton in the CH_2 (carbon) with the dual analyzer in RCS. The middle plot compares the analyzing power for CH_2 measured in RCS to previous measurement during E99007. The bottom compares the analyzing power for carbon measured in RCS to previous measurement during E93027. 52
20 The rate of the signal from 25 block calorimeter vs. threshold. 53
21 The geometry of RCS calorimeter. 54
22 The HV settings for calorimeter PMTs. 55
23 The ADC pedestal width for individual PMTs for the run 2293 with the calorimeter at 37°, on 8.8 meters from the target, beam energy of 5.76 GeV, beam current of 30 μA, and a 15 cm LH2 target with 6% X_0 radiator. 56
24 The blue light attenuation in 4 cm of the lead glass vs distance from the front face for the block. 57
25 The event display with the pion event. Configuration : beam energy is 3.48 GeV, beam current is 3.5 μA, 15 cm LH target with 6% X_0 radiator, proton spectrometer has $\theta_p = 45.7^o$, $P_p = 1.254$ GeV/c, calorimeter position is 31° at distance of 4 meters from the target, trigger in the calorimeter has threshold at $E_{calo} > 390$ MeV. 58
26 The evaporation facility. 59
27 The Quantum Efficiency measurement system. 60

28 Average measured Quantum Efficiency as compared to the CERN extrapolation from in beam data. 61
29 Quantum efficiency as function of CsI thickness. Different curves correspond to different wavelength. 62
30 Quantum efficiency as function of thickness for different condition of contamination (see text). Different curves correspond to different wavelength. 63
31 On beam tests: a) Typical event, b) Overlapping of pions and protons rings. Kaons are in between. 64
32 Shown above is the Jefferson Lab CAD drawing of the auxiliary plane. This detector, which was built by Tel Aviv University, has been built, tested, and is ready for operation. 65
33 Shown above is the Jefferson Lab CAD drawing of the BigBite trigger plane. This detector, which was built by the University of Glasgow, has been built, tested, and is ready for operation. 66
34 Hall A floor map, showing the location of the scintillator array and the calorimeter. The rightspectrometer (not shown) is parked at a large angle. The support frame for both detectors is not shown. 68
35 Full view of the DVCS arm in the current state of the design showing the proton array, the calorimeter and the black box protecting the calorimeter from the light (the walls are not shown). 68
36 CAD drawing of 5-element "tower" from proton array. We tested a prototype tower in March 2002. 69
37 Elastic proton peak height spectra, recorded in one proton array scintillator in coincidence with the $S0$ electron trigger. The two groups of three peaks correspond to HV -762 and -862 V on a Photonis VD109 base and XP2972 PMT, together with an external $\times 8$ amplifier. In each group of three, the elastic proton recoil momenta are 560 (blue), 600 (red), and 640 MeV/c (black). After accounting for the 0.5" Al absorber and the Birks formula quenching in the scintillator, these correspond to deposited electron equivalent energies of 115, 135, and 160 MeV, respectively. . . 70
38 The resolution of the nine-cell PbF_2 test calorimeter as a function of energy. The data has been fit with the function $\sigma/E = a + b/\sqrt{E}$. 72
39 Typical waveform recorded by an ARS channel, yielding two pulses. A waveform analysis is performed to get the information about the two separate pulses. 73
40 The control of the charge asymmetry and the convergence of the average charge asymmetry during a run from tests in June, 2002 demonstrate the effectiveness of feedback using the IA cell. 75
41 Time dependence of the charge asymmetry across the 33 ms helicity-flipping window. 77
42 The two-segment HAPPEX detector. 78
43 Transverse and dispersive envelopes. 82

44 The double ratio, $(P'_x/P'_z)_D/(P'_x/P'_z)_H$, consisting of the ratio of transverse to longitudinal polarization for ^{2}H$(\vec{e}, e'\vec{p})$n divided by the same ratio for ^{1}H$(\vec{e}, e'\vec{p})$. The dot-dashed curve is for PWBA, the dotted curve is for DWBA, the dashed curve includes MEC and IC and the solid curve is the full calculation which also includes relativistic corrections (RC). The open circles are for the MIT-Bates data [49] and the filled squares are preliminary results from the present experiment. . . 88

45 Preliminary results for the ratio of $(P'_x/P'_z)_D$ at $Q^2 = 1.0$ (GeV/c)^2 and $p_m = 160$ MeV/c to $(P'_x/P'_z)_D$ at $Q^2 = 1.0$ (GeV/c)^2 and $p_m = 0$ MeV/c. The p_m value of 160 MeV/c corresponds to the cross section weighted average whereas the central value was 174 MeV/c. The theoretical points shown here have been acceptance averaged and radiatively folded. 89

46 ^{3}He(e,e′p)d cross-sections for $\mathrm{p_{miss}} = 0$ MeV/c. 91

47 Missing energy spectrum. 92

48 Continuum cross section data in the global $(\mathrm{E_{miss}}, \mathrm{p_{miss}})$ phase space of the considered kinematics (left) and for selected momentum transfer region as compared to a PWIA calculation; the red curve on the left panel indicate the correlation bewteen $\mathrm{E_{miss}}$ and $\mathrm{p_{miss}}$ if the interaction occurs on a quasi-deuteron inside the nucleus. . 92

49 Preliminary cross section data are compared with recent models and a multipole fit. The panels are labeled by ϕ. 94

50 Preliminary data for response functions are compared with recent models and a multipole fit. The top set contribute within the scattering plane while the bottom set requires out-of-plane acceptance. The unpolarized cross sections were included in the multipole fit also but were not decomposed into response functions for this purpose. 96

51 Preliminary 1+ multipole fits. Fitted amplitudes for $Q^2 = 0.9$ or $Q^2 = 1.1$ (GeV/c)^2 are shown as filled or open circles, respectively. Baseline (MAID2000) amplitudes for these sets are shown as solid or dashed curves. The corresponding amplitudes for the DMT model are shown in red. 97

52 Superratio R/R_{PWIA} as a function of Q^2 for this experiment and for the Mainz experiment [69]. R is defined as the double ratio $(P'_x/P'_z)_{He}/(P'_x/P'_z)_H$. In PWIA (short-dashed curve) this superratio is identically unity, barring acceptance-averaging effects. The dashed curve shows the results of the full relativistic calculation of Udias *et al.* [70]. The dot-dashed curve shows the results of Laget's full calculation, including two-body currents [71]. The solid curve indicates the full relativistic calculation of Udias including medium modifications as predicted by a quark-meson coupling model [60]. For $Q^2 > 1.8$ (GeV/c)^2 the Udias calculations maintain a constant relativistic optical potential and are indicated as short-dashed curves. Lines connect the acceptance-averaged theory calculations and are to guide the eye only. 99

53 Low Energy Theorem extraction of structure functions $P_{LL} - P_{TT}/\epsilon$ and P_{LT} at $Q^2 = 1$ and 1.9 GeV^2. The two plots present $\Delta\mathcal{M}/v_{LT}$ as a function of the ratio v_{LT}/v_{TT}. (see Eq. 6–10). The extracted slope is P_{LT} and the intercept is $P_{LL} - P_{TT}/\epsilon$. 102

54 Q^2-dependent polarizabilities, including preliminary results from Jefferson Lab E93050 (blue points), Mainz VCS results from J. Roche *et al.* [78] (red point), world average of RCS results [77] (black point), and kinematics of Bates experiment (green arrow) [79]. The solid blue curves are the prediction of the Dispersion Relations, including just πN intermediate states. The contributions to α_E and β_M beyond πN intermediate states are parameterized by two dipole functions $\Delta\alpha_E(0)/[1+Q^2/\Lambda_\alpha^2]^2$ and $\Delta\beta_M(0)/[1+Q^2/\Lambda_\beta^2]^2$ (dashed blue curves). These are fit to the $Q^2=0$ GeV^2 and 1 GeV^2 points. The black lines are the full DR calculations. The DR curves show that the πN states, including the Δ, strongly overpredict the magnetic polarizability. A strong diamagnetic contribution is required from the sum over all other (higher energy) channels. The red curve is the proton electric form factor, normalized to the the $Q^2=0$ point. The green curve is the Chiral Perturbation Theory result [80]. 104

55 Integral of $g_1(x,Q^2)$ for the neutron at several fixed values of Q^2. The results of this experiment are shown in solid circles (green) and the band located around zero represents the size of systematic errors. The red solid circles are data from SLAC E143 [85] experiment dominated by the resonance region, the red solid triangle pointing down represents SLAC E142 [86] result while the red diamond shows SLAC E143 result [85]. The red solid triangle pointing up represents SLAC E154 [87] result. All blue square are Hermes experiment results [88]. At low Q^2 the solid lines corresponds to χPT calculations by Bernard *et. al.* [89] (green) without vector mesons and by Bernard *et. al.* [90] (blue curve) with vector mesons, respectively. The dashed line is a calculation by Ji *et. al.* [91,92] (black dashed line) using heavy baryon χPT. The solid black line represents the GDH result. At moderate and large Q^2 two calculations, one by Soffer and Terayev[93] (purple solide curve), the other by Burkert and Ioffe[94] (orange solid curve) are plotted. At large Q^2 the red line represents the evolution [96] of the world's deep-inelastic data due to the changing coupling constant α_S Soffer and Terayev assume that the integral over g_1+g_2 varies smoothly from high Q^2 where $g_2\approx 0$ down to $Q^2=0$. Using their simple prediction for this integral and subtracting the contribution from g_2 using the BC sum rule [95]. Burkert and Ioffe consider the contributions from the resonances using the code AO, and the nonresonant contributions using a simple higher-twist-type form fitted to the deep-inelastic data. Their model is constrained to fit both the GDH and the deep-inelastic limits, and it describes the data quite well. 106

56 Integral of the neutron structure function $g_2(x,Q^2)$ extracted in E94-010 (red solid circles) at several Q^2 values reported along the SLAC E155X [98] proton (red open square) and neutron (blue open circle) results. The green band at zero represents the systematic uncertainty of this experimental result. The red curve is an evaluation of the integral using MAID [82]. Reasonable agreement between the data and the MAID prediction is observed. 107

57 d_2 matrix element at several values of Q^2. The results of this experiment are shown as the red solid circles and the green band represents their corresponding sytematic uncertainty. The SLAC E155X [98] proton (red open circle) and neutron (blue open square) results are also shown. The blue curve corresponds to the MAID calculation[82]. The red curve is a Heavy Baryon χPT calculation[83] valid only a low Q^2. The Lattice prediction at $Q^2 = 5$ GeV^2 for the neutron d_2 matrix element not shown here is negative but close to zero. We note that all models predicts d_2^n to be negative or zero. The moderate Q^2 data of E94-010 show a positive d_2^n but decreasing perhaps to zero at high Q^2. The SLAC data also shows a positive d_2^n but with a rather large error bar. 108

58 The scaled differential cross section $s^7 \frac{d\sigma}{dt}$ versus center-of-mass energy for the $\gamma p \to \pi^+ n$ (upper plot) and $\gamma n \to \pi^- p$ (lower plot) at $\theta_{cm} = 90°$. The data from JLab E94-104 are shown as solid circles. The error bars for the new data and Anderson *et al.*'s data [104], include statistical and systematic uncertainties, except that those in the insets only include point-to-point uncertainties to highlight the possible oscillatory scaling behavior. Other data sets are shown with only statistical errors. The open triangles in the lower plot were averaged from data at $\theta_{cm} = 85°$ and 95° [105]. 110

59 The cross section ratio of π^- to π^+ photoproduction versus center-of-mass energy 111

60 Preliminary results from E97-103 showing errors only. Also shown are calculations of the g_2^{ww} using various fits to the world data on g_1. 113

61 The online missing mass yield taken in March 2002 at $Q^2 = 1.9$ (GeV/c)^2, $W = 1.95$ GeV and $t = t_{min}$. 116

62 Shown on the left are the preliminary H(e,e′K$^+$) cross section results as a function of the invariant mass, W. On the right is the published real photon data of Bockhorst *et al.* from SAPHIR plotted with the same empirical fit to the W-dependence. . 117

63 Shown are the preliminary H(e,e′K$^+$) separated cross section versus $/varepsilon$. Final error bars will be 4–5 times smaller. 118

64 Kinematic coverage of E99-114 measurements. 119

65 Polarization transfer in the RCS process. The labels on the curves are KN for the asymmetry in the hard subprocess; the pQCD calculations [115] with AS for asymptotic distribution amplitudes, CZ for Chernyak-Zhitnitsky, COZ for Chernyak-Ogloblin-Zhitnitsky, and KS for King-Sachrajda; hand-bag for calculations in Soft overlap approach [116]. 120

66 A_1^n results compared with theoretical predictions. Curves: predictions of g_1^n/F_1^n from pQCD HHC based BBS parametrization (1) and LSS(BBS) parameterization (2), g_1^n/F_1^n from LSS 2001 parametrization at Q^2 = 5 (GeV/c)^2 (3); predictions of A_1^n from constituent quark model (light shaded band), statistical model at Q^2 = 4 (GeV/c)^2 (3), local duality (4), chiral soliton model at Q^2 = 3 (GeV/c)^2 (5), and E155 fit at Q^2 = 4 (GeV/c)^2 (6). Data from Hermes and SLAC are original values without being re-analyzed for the new nuclear corrections. 122

67 $(\Delta u + \Delta\bar{u})/(u + \bar{u})$, $(\Delta d + \Delta\bar{d})/(d + \bar{d})$ Hermes data error bars are statistical only. Error band in the middle shows the uncertainty due to neglecting s, $\bar{s}$ contribution. 123
68 Projected A_{LT} data in comparison to calculation of Udias et al. The solid squares are the E89-003 data obtained in slightly different kinematics. The open circles represent the anticipated data from E00-102. Figure courtesy J.M. Udias 127
69 The experiment kinematics. HRS_l was fixed at 12.5^o throughout the experiment. HRS_r rotated about the $\vec{q}$. 128
70 Projected uncertainties for E01-001 (blue squares), along with a global analysis of the Rosenbluth data (green circles), and the polarization transfer measurements from Hall A (red crosses). 130
71 Kinematics for E01-001. Each line represents a different beam energy, and the solid points are the ϵ values measured. 131
72 Proton momentum, relative to expected momentum for elastic scattering. The solid line is the data, while the green and red lines represent the simulated elastic peak and background spectrum (the blue line is the total spectrum). 132
73 Kinematic setting measured; the various colors represent the Q^2 values: $Q^2 = 0.8$ $(GeV/c)^2$ (blue), $Q^2 = 2.35$ $(GeV/c)^2$ (red) and $Q^2 = 3.5$ $(GeV/c)^2$ (yellow). . . 133
74 Time of flight spectrum for the Q1_f40l kinematics ($Q^2 = 0.8$ $(GeV/c)^2$). 134
75 Time of flight spectrum for the Q3_f40l kinematics ($Q^2 = 3.5$ $(GeV/c)^2$). 135

List of Tables

1 Systematic errors of Compton polarimetry using electron only data (A_1^n and g_2^n experiments) 19
2 Crude estimate of the expected missing energy resolution. 30
3 Distribution of paddles on time resolution. 34
4 Ratios of the coincidence data yield data divided by the MCEEP yield for each of the optics models. All simulations used the dipole nucleon form factors. 43
5 Calorimeter energy resolution. 56
6 The table shows the estimated performance parameters based on Transport calculations of the optical properties. For y_0, as much as $\pm$ 20 cm makes it through the spectrometer, but the ϕ_0 centroid shifts. The error estimates assume a 0.5 mrad angle determination and 100 μm position determination. 81
7 The first order Transport matrix in natural units (m, rd) for the 35° configuration. 82
8 The first order matrix for the 20° configuration. 83
9 The first order matrix for the 12° configuration. 83
10 Expected resolutions: both δ and θ are reconstructed well better than the anticipated resolution; y and ϕ still require some work. 84
11 Parallel kinematics measured in the experiment. 90
12 The left arm detector stack used in the experiment. 126

Introduction

1 Introduction

The Hall A collaboration can look back on FY02 as another successful and very productive year, as for instance evidenced by the continuing production of refereed publications, Ph. D. Theses and conference presentations, but also by the volume of this report. The only setback was the ongoing delay in the delivery of the septum magnets. The experimental schedule for FY02 had to be readjusted several times to accommodate that. Because of two failures of the cryo-target, the Hall A availability dropped to just under 80 %, but it is thanks to the dedication and expertise of our technical support group that it did not drop further.

In October/November experiment E00-120 (Bertozzi, Fissum, Saha, Weinstein), testing the limits of the single-particle model in ^{16}O$(e, e'p)$, was successfully run. The December/January shut down was used to remove the waterfall target system and install the cryogenic target system, the Focal Plane Polarimeter (FPP) and the lead-glass calorimeter with its associated charged-particle sweep magnet required by experiment E99-114 (Hyde-Wright/Nathan/Wojtsekhowski). E99-114 carried out precise measurements of Real Compton Scattering at high luminosity. Following E99-114, E98-108 (Baker, Chang, Frullani, Iodice, Markowitz), electro-production of kaons up to $Q^2 = 3$ (GeV/c)^2, was completed in February. Experiment E01-001 (Arrington/Segel) ran in May. E01-001 performed a new measurement of G_E^p/G_M^p, using an improved version of the Rosenbluth separation technique by detecting the recoiling proton. In June the first half of E01-020 (Boeglin, Jones, Klein, Ulmer, Voutier), electro-disintegration of the deuteron, was completed. Then, when it became clear that the septum magnets would not be delivered during the summer down, experiments E00-107 and E00-007 (Gilman, Holt, Meziani for both) were scheduled for September. Because of problems with the cryo-target E00-107 could not run, but E00-007 was completed successfully. In October/November E01-020 was successfully completed.

In November/December the polarized ^{3}He target will be installed at the standard interaction point to allow E01-012 (Chen, Choi, Liyanage), a study of spin duality in ^{3}He, to run. One septum magnet is expected to be ready for installation during the February/March shutdown, when also the polarized ^{3}He target will be moved 80 cm upstream to the septum interaction point. This will allow to run E97-110 (Chen, Deur, Garibaldi), Forward-angle GDH, in April/May. The second septum magnet will then be installed, together with the cryotarget, in May/June, followed by running E00-114 (Armstrong, Michaels) for a week and E99-115 (Kumar, Lhuillier), HAPPEX-II, to completion in July-September. After replacing the cryo-target by the waterfall target, E94-107 (Frullani, Garibaldi, LeRose, Markowitz, Hashimoto), a study of hypernuclear spectroscopy, has been scheduled to run in November/December. On completion of E94-107 the septa will be removed and Big Bite will be installed for commissioning and running of the first experiment.

It should be emphasized that the schedule described above and intentions for

the farther future imply a large design effort, which is only (and even then barely) possible thanks to the hard work of our design group.

Finally, the completion of the Hall A pCDR for the 12 GeV upgrade merits special attention. It describes in great detail the research program and the associated instrumentation upgrade envisioned for Hall A when the 12 GeV upgrade is implemented. Although a large group has contributed to this effort, special mention should be made of the coordinating efforts of Jian-ping Chen.

Standard Hall A Facilities

2 Standard Hall A Facilities

2.1 Beam Line

2.1.1 Compton Polarimeter

Contributed by D. Lhuillier

Introduction

The hall A Compton polarimeter is a 15 meters long magnetic chicane made of 4 dipoles. At the center the CEBAF electron beam crosses an IR laser beam whose power is amplified by a factor 5000 into an optical cavity. This apparatus allows non invasive measurements of the electron beam polarization, simultaneously of the running experiment.
We report here results of the A_1^n and g_2^n polarimetry and progress of the online data analysis. We list few possible options for upgrade at lower or higher beam energy.

Polarimetry for hall A experiments

First results of the Compton polarimeter (HAPPEx experiment) have been published [1]. An article on the analysis of coincidence events, first developed for the G_p^e and $N-\Delta$ experiments, is in preparation.
About 100 runs have been taken during the A_1^n and g_2^n experiments in summer 2001. The analysis has been performed using the electron data only. The electron detector consist in 3 planes of 48 μstrips located few mm above the primary electron beam between the third and the fourth dipoles. This method relies on the fit of the theoretical asymmetry with the experimental asymmetries for each

Source	Typical relative error per run (%)		
	at 3.5 GeV	at 4.6 GeV	at 5.7 GeV
Stat.	1.5	1.0	1.0
Calibration	3.0	2.5	2.0
Beam fluctuations	1.3	0.8	0.6

Table 1: Systematic errors of Compton polarimetry using electron only data (A_1^n and g_2^n experiments)

strip. The main systematic effect comes from the determination of the Compton edge which is used to calibrate the detector (see table1). The associated relative error scales with the mean Compton asymmetry.
Polarimetry results for A_1^n and g_2^n are shown in fig.1. They are systematically below the Moller measurements but the observed difference of 4% can be explained by the systematic errors quoted for the two techniques.

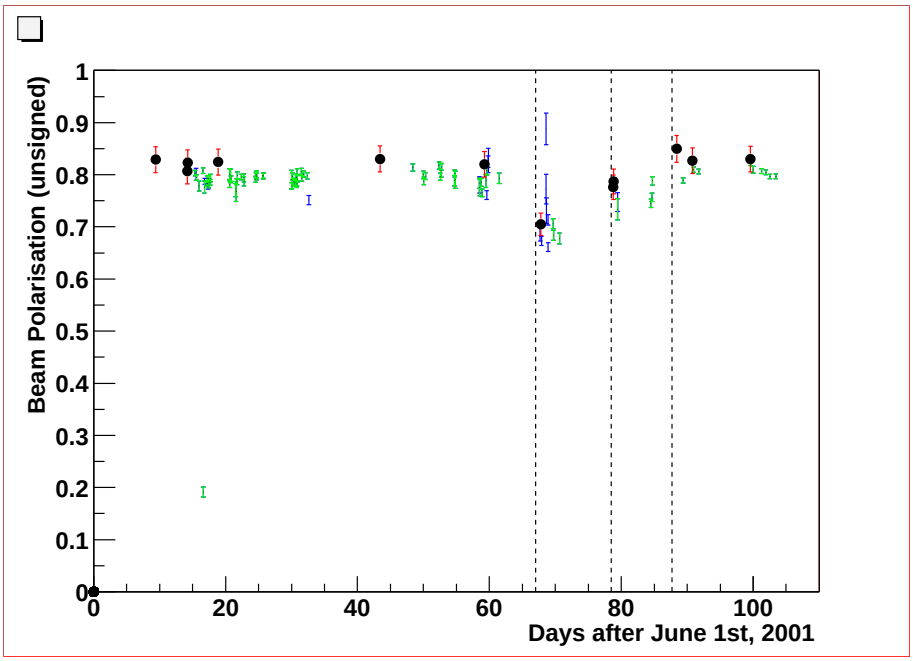

Figure 1: Green points: Compton measurements for the A_1^n and g_2^n experiments. Only the statistical uncertainty is represented. Typical systematic errors of table1 must be added in quadrature. Blue points: rejected Compton measurements due to background or inconsistent calibration. Black points: Moller measurements, stat+syst error bars.

Online analysis

The best accuracy obtained so far was the result of a quite tedious analysis using the electron detector as a photon energy tagger to determine the response function of the photon detector [2]. Once this function is known the mean analyzing power can be accurately computed.

The "electron only" analysis although leading to larger uncertainty due to its sensitivity to calibration is more direct and more suitable for an online analysis. Both methods are now implemented at JLab. The electron analysis runs automatically at the end of each Compton run. Figure 2 illustrates fits on recent electron data taken at 4 GeV for the deuteron photo-disintegration experiment. This new root based software is faster and allows a better online control of the quality of the data. Also comparison between the two methods can easily be tested which offers a powerful cross-check of the polarization measurements.

Upgrades for a larger energy range

The upper bound of the Compton polarimeter energy range is set by the maximum field available in the dipoles of the magnetic chicane. These are water-cooled

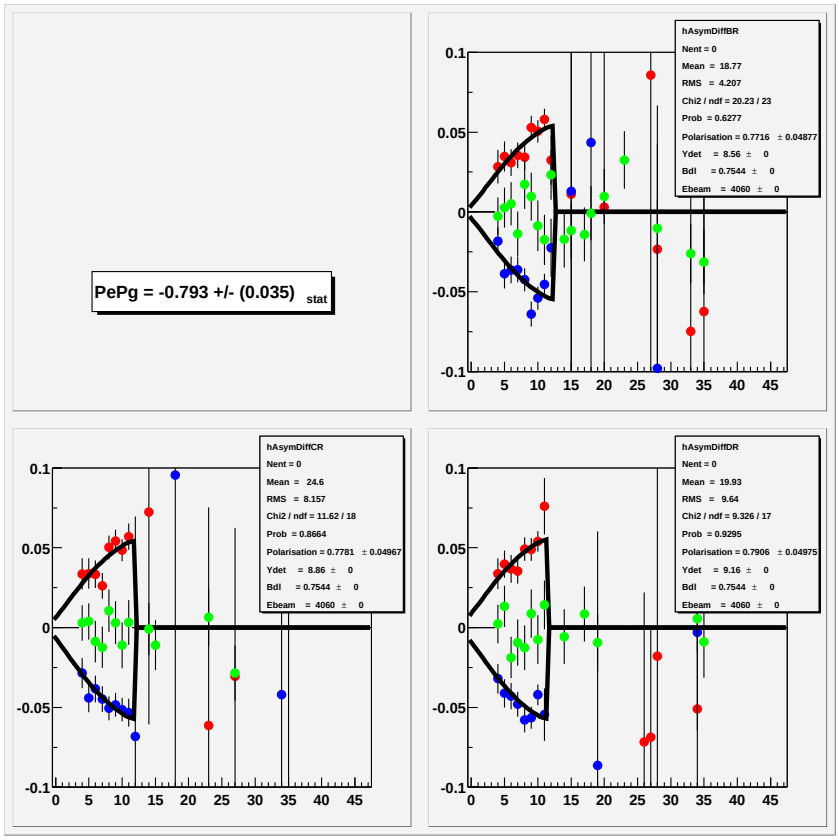

Figure 2: Example of electron analysis at 4 GeV. The 3 plots show the compton asymmetry versus strip number for each plane of the electron detector. Red, blue and green points correspond to left, right and off laser state respectively.

magnets limited to 1.5 T corresponding to a maximum beam energy of 8 GeV. The cheapest way to extend this limit to 11 GeV is to reduce the vertical dispersion of the chicane in the ratio 8/11 [3]. The bottom two dipoles along with the optics cavity and the photon detector would be raised by 8 cm.

The electron detector is a key element for accurate polarization measurements. The gap between the primary electron beam and the first micro-strip is the main parameter driving the lower energy limit. In the current setup, this gap is about 7mm which means no Compton electrons can be detected with hall A beam energy below 2.5 GeV. In order to provide more margin to the next HAPPEx measurements at 3.2 GeV, we plan to move the electron detector 2mm closer to the primary beam. This should increase the number of fired micro-strips from 6 to 9 which is a significant gain.

The Lead parity experiment requires a 1% accuracy on the beam polarization at 850 MeV. Since the figure of merit of Compton polarimetry goes like $1/E^4_{beam}$ this

measurement is a real challenge. The most efficient way to keep a good accuracy would be to go to a green or even UV laser light. This is a major upgrade of the polarimeter which requires to change most of the optical elements and cavity locking system. More segmented electron detector and low threshold photon detection may also help. Possible options are under investigation.

2.2 Target

2.2.1 Status Report on the Cryogenic Target

Contributed by J.-P. Chen

The Hall A cryotarget system [4] consists of 3 loops: loop 1 is usually for gaseous helium (either ^{3}He or ^{4}He) at 6K and 15 atm, loop 2 liquid hydrogen at 19K and loop 3 liquid deuterium at 22K. Both the LH_2 and LD_2 loops are operating at pressures above 20 psi. Each of the LH_2 and LD_2 loops has two target cells with typical lengths of 15 cm or 4 cm.

In year 2002, the cryotarget system was used for a number of experiments: Real Compton Scattering (RCS), Kaon Electro-production, Super-Rosenbluth to measure G_E^p/G_M^p, D(e,e'p) at high Q^2, and D(γ,p)n. All the experiments used the new machined cells, which have a smaller diameter (1.5 inches) than that of the 'beer can' cell (2.5 inches). Using a radiator mounted on the target cell block, much closer to the target cell than the previously used radiator, the photon beam experiments were able to use the small diameter machined cells without much problem with respect to background.

A number of improvements were done by the JLab cryotarget group. The pressure sensors were changed to a new type. It improved but did not completely get rid of the problem that the pressure read-outs drift with time due to radiation. New Graphic User Interfaces (GUIs) based on the standard JLab MEDM replaced the original Tcl/Tk GUIs for most parts of the target GUIs. A beam replacement algorithm was added to the high power heater PID control. The computer control of the J-T valves (for the coolant control) was made to work and the manual control box was removed.

The main problem encountered during this period was the motion system failure. Because of the experimental schedule change due to the delay in the Septum magnets delivery, the planned cryotarget re-work of the motion system was only partially done. The motion system problem has not yet been completely fixed. One such a failure happened at the start of the experiment after the summer down time. The motion system failure caused the target ladder to slide to the bottom of the scattering chamber, resulting in significant damage to the target loops. The repair work took about 2 weeks. Complete motion system re-work has been planned when the cryotarget is available for service.

Another cryotarget incident happened before the summer down time when a software mix-up caused a vent valve to be opened and later when the target was cooled down, the loop went to sub-atmospheric and air went into the loop. Frozen water vapor blocked the supply and return lines. When the target warmed up after the experiment was over, the pressure build-up caused the target cell upstream window to rupture. The software controlled vent valve has been removed. Some emergency buttons and a new procedure were added to prevent similar incidents from happening again.

Also worth mentioning are the problems we had encountered with the loop fans. Twice this year, one loop fan was not working properly and produced excessive heat. The first time the problem was traced to the power supply leads which were swicthed, causing the fan to rotate in the wrong direction. The second time the problem was caused by the differencial pressure bypass valve which was left open. Bothe times the fan problems went away once the mistake was corrected.

Work is on-going to get ready for two parity experiments using 20 cm long cells for high pressure Helium and for LH_2 running. The Cal State LA group has produced one 20 cm race-track shaped aluminum cell with wall and window thickness of 0.010 inch (for a high pressure Helium target), and three 20 cm race-track cell with window thickness of 0.005 inch (for LH_2 target). The Helium cell was tested to 500 psi and the LH_2 cells were tested to 100 psi. The matching cell blocks are being manufactured by the JLab cryotarget group. A set of 'beer can' cells and cell block will also be used for the LH_2 parity experiment. Density fluctuation is a major concern for the parity experiments, especially the LH_2 parity. Several tests were done[5], showing that the machined 15 cm cell had significant density fluctuations at beam currents greater than 30 μA at nominal raster size (2mm by 2 mm), beam intrinsic spot size and loop fan speed (60 Hz). Tests during the first HAPPEX experiment showed that the 15 cm 'beer can' cell has marginally acceptable density fluctuation. A calculation[6] was performed by the cryotarget group indicated that the bulk boiling and the wall boiling both contributed to the density fluctuation. For the race-track shaped cell, it is expected that its flow, being transverse,should improve over that of the 'beer can' or the machined cell. However, no density fluctuation study has been done yet for the race-track cells.

Another issue for the Helium parity experiment is the 4K cooling power. To be able to get enough cooling, the first issue is the return coolant pressure. A workable solution was proposed by the JLab cryo group to have a re-distribution of the return lines. However, even with the solution, due to the limitation of the CLAS magnet return pressure, the total cooling power is still limited. An estimation was given by the cryo group that when Hall B is running, assuming the coolant consumption of the other systems are not excessive, the maximum available 4K cooling will allow the Hall A high power helium target to take no more than 75μA. The current can be raised to 100 μA if Hall B is not running.

2.2.2 Hall A Bremsstrahlung Radiator Status Report

Contributed by D. Meekins

A new type of Bremsstrahlung radiator was developed to accommodate the needs of the Real Compton Scattering (RCS) experiment. This radiator consists of a set of thin copper foils attached directly to the front of the cryogenic target cells. The radiator material is 99.996% copper (Cu63 69.09%)+(Cu65 30.91%). The typical thickness of these foils is 0.81 g/cm^2 ($\sim$ 6% radiation lengths). These

properties are similar to the 6% upstream radiator designed and installed by Rutgers University, Florida State University, and Jefferson Lab. The Rutgers radiator is about 75 cm upstream from the center of the target. The geometry of the entrance window of the machined style cell is such that a radiator this far upstream would not be acceptable (due to multiple scattering of the electron beam and opening angle of the high energy bremsstrahlung flux). While the new radiator thickness cannot be changed or removed without warming up the target (a flexibility that is often desired) and replacing or removing the foils, it does eliminate the concerns of having a radiator too far upstream. Much of the background from electrons multiply scattered in the radiator and interacting with the target materials (i.e. cell blocks and cell walls) is also eliminated. The new radiator also has the advantage that it is attached to the target cell/cell block mass which has a constant temperature of roughly 20K thus, there is no need for additional cooling as is the case for the Rutgers radiator. The new radiator is also extremely simple to fabricate and install (when the target is warm). Care must be taken however when selecting these radiators for an experiment. Both the radiator thickness and cell lengths must be determined and cannot be changed without warming up the target. Additionally, it has become standard practice to subtract backgrounds by taking data on the same length cell without the radiator. Thus, two cells of the same length must be installed on the same loop. This conflicts with the standard configuration of the cryotarget and limits overall flexibility. The radiator performed well during the RCS experiment and was essential to the performance of experiment E00-007 which due to time constraints could not rely on the Rutgers radiator.

2.2.3 Status Report on the Polarized ^{3}He Target

Contributed by J.-P. Chen

The Hall A polarized ^{3}He target [7] was built in 1998 and was successfully used for the experiments E94-010 [8] and E95-001 [9] in 1998-1999, and after upgrade, successfully used for two more experiments E99-117 [10] and E97-103 [11] in the summer of 2001.

The polarized ^{3}He target uses optically pumped Rubidium vapor to polarize ^{3}He nuclei via spin exchange. Two sets of Helmholtz coils provide a 25 Gauss holding field for any direction in the scattering (horizontal) plane. Target cells are usually 40 or 25 cm long with density of about 10 amg (10 atm at 0°). Beam currents on target range from 10 to 15 μA to keep the beam depolarization effect small and the cell survival time reasonably long (> 3 weeks). The luminosity is about 10^{36} nuclei/s/cm^2, which is the world highest polarized luminosity. The in-beam average target polarization achieved with $\approx 12\mu$A is over 40%. Two kinds of polarimetry, NMR and EPR (Electron-Paramagnetic-Resonance), are used to measure the polarization of the target.The uncertainty achieved for each method is

less than 4% relative and the methods agree well within errors. The analysis of the polarimetry data from E99-117 and E97-103 was completed. Figure 1 shows the target performance during the period of E99-117 and E97-103 experiments. The polarization measurements were independently checked by measuring the elastic scattering asymmetry. The ratio of the measured asymmetry to the world data gives a measure of the product of the beam polarization and the target polarization. The deduced target polarization is in good agreement with the NMR and EPR results.

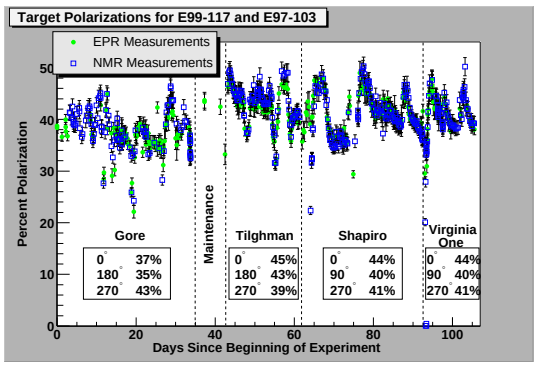

Figure 3: Polarized ^{3}He target performance during E99-117 and E97-103

Work has been focused on getting the polarized ^{3}He target system ready for the upcoming E97-110 (Small Angle GDH) experiment. The main modification is the target cell changed from cylindrical to ice-cream-cone shaped to minimize the material thickness in the path of the scattered particles. A comprehensive effort was made for the R&D work for the new shaped cell. Both glassblowers from Princeton and UVa, and both polarized ^{3}He target groups at UVa and William and Mary have worked almost continuously for many months. Over twenty cells were produced, but only two were tested to have lifetimes above 40 hours. Unfortunately only one of the two survived testing and can reach maximum polarizations of over 40%. Two more cells have lifetimes around 30 hours and could be back-up cells. The rest of the cells either have lifetimes less than 20 hours or were broken during the manufacturing or testing process. Tests are continuing to identify problems and to improve the success rate for producing good cells.

The target ladder and the supporting mechanical structure were modified to accommodate the new cell geometry and to support several sets of collimators designed to keep the cell end window contributions from going into the spectrometers.

The target lab is fully functional. EPR system has been improved to have optical fiber path instead of a cumbersome optical system. The laser spectroanalyzer will also use optical fiber to replace the optical mirror system. All the target cells were extensively tested. Usable cells were fully characterized: density

was measured with the pressure broadening optical method, and wall thickness was measured with laser interferometer method. Some were cross-checked with similar measurements performed by the UVa group.

2.3 Spectrometers

2.3.1 Spectrometer High Resolution Test

Contributed by J.J. LeRose, D.W. Higinbotham and G. Chang

On June 30, 2003 a "High Resolution Test" was made using the HRS pair in Hall A. In this test, the two spectrometers were vacuum coupled to the scattering chamber and missing mass spectra were taken for the ^{12}C(e,e′p) reaction using a 20 mil graphite target. The original motivation for the test was the observation that achieved missing mass resolutions using an extended cryotarget with its attendant windows etc. gave significantly worse resolution, by as much as a factor of two, than was expected from simulations. The test was formulated with the intention to eliminate complications from the target configuration and test what the spectrometers themselves were capable of delivering in terms of missing energy resolution.

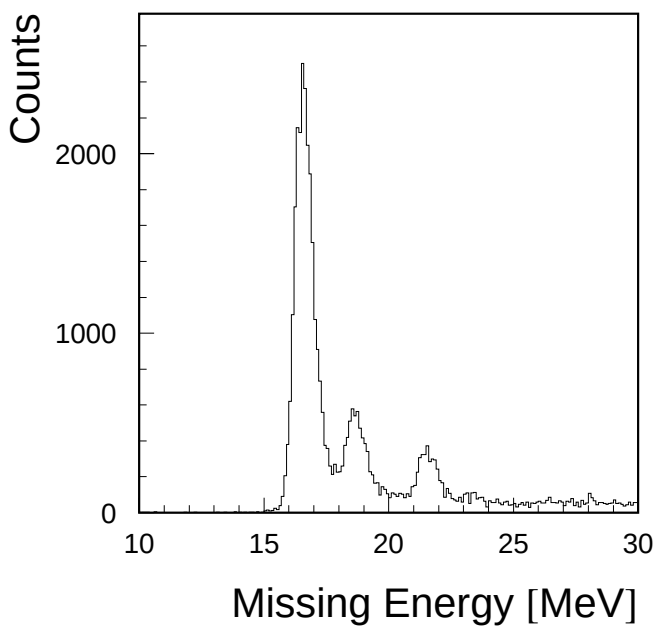

Figure 4: Missing energy spectrum from the ^{12}C(e,e′p) reaction. A 4.7 GeV/c beam was used with an electron scattering angle of 16.1° and a hadron scattering angle of 45°. The electron momentum was 3.796 GeV/c and the hadron momentum was 1.489 GeV/c. The beam energy spread was determined to be approximately 5.0×10^{-5}.

Shown in Fig. 4 is the energy spectrum from the ^{12}C(e,e′p) reaction. The FWHM of the ground state is 800 keV. Fig. 5 shows the correlation between focal plane trajectory parameters and the missing energy. It was generated on-line, during data taking, using the standard optics database (i.e. no special optimiza-

tion was done for this analysis). Imperfections in the reconstruction tensor would manifest themselves as a departure from flat horizontal lines in the plots. Things appear to be very well in hand.

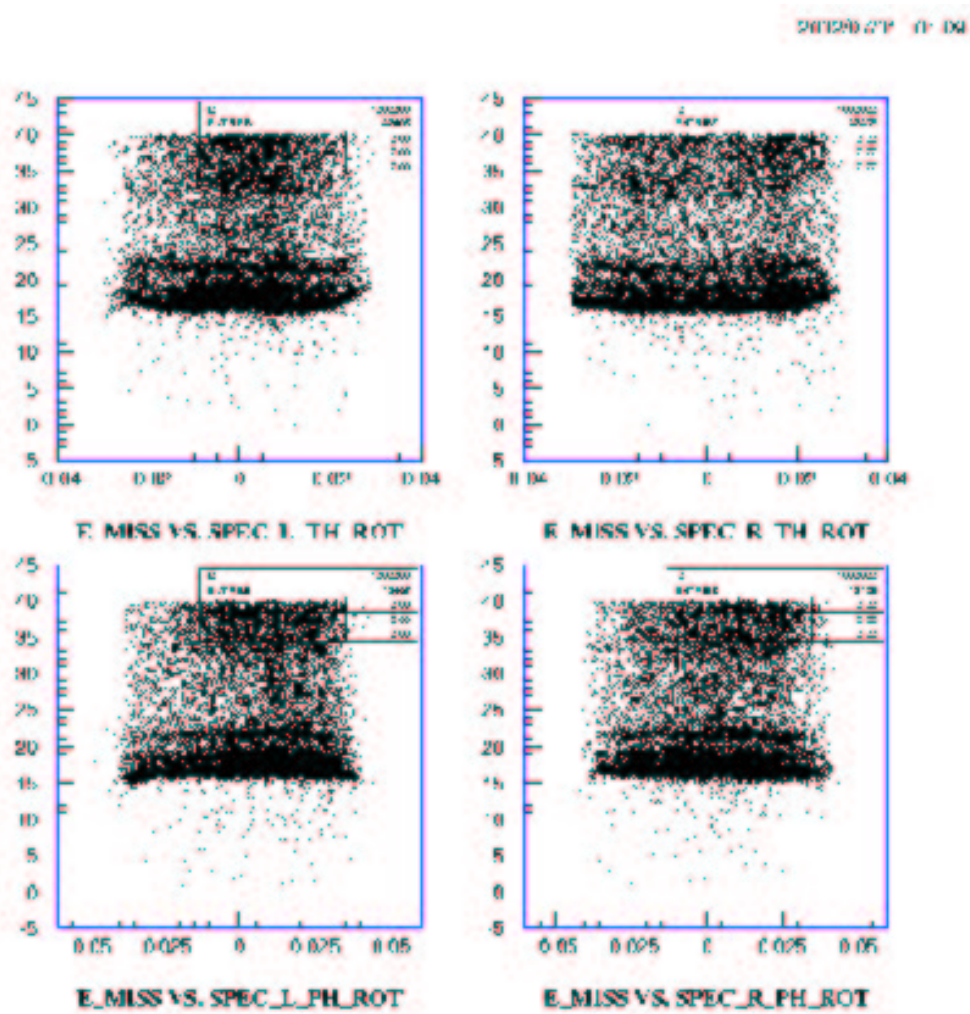

Figure 5: Correlation between missing energy and trajectory angles (θ and ϕ) for left and right arms; flatness of the missing energy lines indicates the quality of the momentum reconstruction tensor D_{ijkl}.

Expected resolution

A rough estimate based on a series of "back of the envelope" (Tab. 2) calculations of the approximate amplitude of various contributing factors added in quadrature, assuming δE/E $= 5 \times 10^{-5}$ (3.2×10^{-5}) for the beam, would give 720 keV (581

keV).

	Electrons	Protons
P (MeV/c)	3796.2	1489.0
θ (°)	16.1	45.0
Spectrometer multiple scattering (FWHM (keV)) (exit window and detector stack)	**342**	**196**
Vertical angle resolution $\sigma\theta_0$	0.0011	0.0017
σE/E from $\sigma\theta_0$	0.0452	0.0105
FWHM (keV)	**106**	**25**
Horizontal angle resolution $\sigma\phi_0$	0.0003	0.0004
σE/E from $\sigma\phi_0$	0.0059	0.0038
FWHM (keV)	**0.7**	**0.9**
Total FWHM (keV)	**358**	**198**
Electron arm + Proton arm	**409**	
Beam		
E (MeV)	4703.26	4703.26
σE/E	3.2×10^{-5}	5.0×10^{-5}
σE (MeV)	0.150504	0.235163
Total beam FWHM (keV)	**354**	**554**
Target straggling FWHM (keV)	**211**	**211**
Missing mass resolution (FWHM (keV))	**581**	**720**

Table 2: Crude estimate of the expected missing energy resolution.

A MCEEP simulation [12] for the measured spectrum predicts a FWHM missing energy resolution of 643 keV. The calculation included: energy loss and multiple scattering in the target foil (corrected for mean energy loss, as ESPACE normally does), gaussian distributed beam energy distribution with FWHM of 1.2×10^{-4}, multiple scattering in the exit window of the spectrometer and the air between the window and VDC (as a gaussian distribution), resolution and scattering effects in the VDC's, based on gaussian distributions and input from Nilanga Liyanage [13], errors induced by forward and then reverse mapping via new transfer functions, no collimators, a beam spot size of zero, and perfect spectrometer

alignment and beam alignment.

In conjunction with this test a GEANT simulation [14] of the same reaction was performed. The simulation took into account: multiple scattering in the spectrometer exit window and subsequent air and detectors, spectrometer optics, beam energy spread, and all energy loss processes in the target (dE/dx, external and internal Bremsstrahlung). This calculation predicts a FWHM of 800-830 keV (640-660 keV) for beam energy spread $\sigma E/E = 5 \times 10^{-5}$ (3.2×10^{-5}).Unfortunately, a comparison of the effects of the various components of that calculation with those presented in Tab. 2 show some serious discrepancies, leaving the possibility that the agreement between the simulation and experiment may be fortuitous. Work continues on the resolution of those discrepancies.

Conclusion

In conclusion of the "High-Resolution Test", the spectrometers performed essentially according to expectations. The observed resolution was somewhat worse than predicted by simulation, but no factors of two were evident. Significant contributors to the missing energy resolution include:energy spread of the beam (350 - 550 keV at 4.7 GeV), ionization losses in the target (200 keV), and multiple scattering in the spectrometer exit windows and VDC's (350 keV for a 3.8 GeV/c electron and 200 keV for a 1.5 GeV/c proton).

2.3.2 High Resolution Trigger Counter S2m

Contributed by B. Wojtsekhowski in collaboration with P. Ambrozewicz, W. Boeglin, P. Markowitz, A. Shahinyan, H. Voskanyan

Two scintillator planes were constructed for use in the HRS spectrometers. They will be used as replacements of the existing S2 planes. The counter is divided into 16 paddles each viewed by two PMT XP2282B.

Introduction

After the initial set of experiments in Hall A were done the demand for better coincidence time resolution become more frequent. Pushing the limits of the shell model ^{16}O(e,e'p) experiment [15] at large missing momentum and the kaon electro production experiment [16] are examples for which the presently available time resolution is not adequate. The existing S2 trigger plane (see reference [18]) consists of 6 large paddles (40 cm x 60 cm), with a thickness of only 5 mm. These two factors (large area and small thickness) limit the time resolution (sigma) at the level of 0.30 ns. Figure 6 shows the level of real to accidental events in time-of-flight spectra from ^{16}O(e,e'p). Figure 7 shows that at a momentum of 2 GeV/c kaon selection will benefit significantly from improvement in the time resolution.

For future studies of kaon production in the DIS regime the improvement in time-of-flight is mandatory.

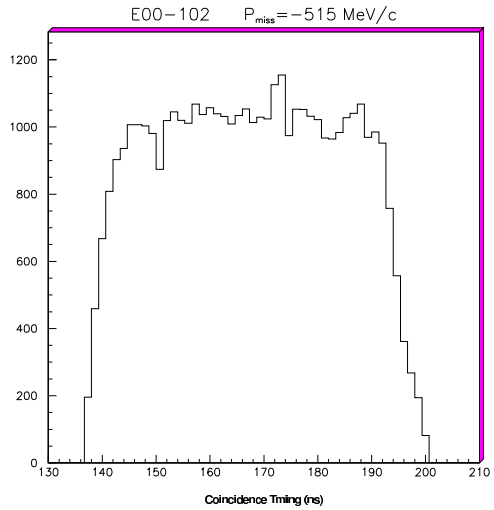

Figure 6: Time-of-flight spectra in ^{16}O(e,e'p) experiment at large (negative) missing momenta (-410 MeV/c). The real coincidence peak at time of 170 ns has width of 1 ns.

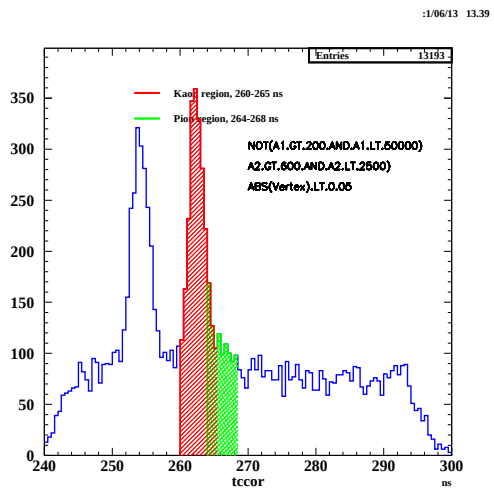

Figure 7: Time-of-flight spectra in H(e,e′K) experiment.

Design Considerations

Because the second trigger plane is located after both the tracking and the PID components of the detector package its thickness can be much larger than in the existing detector S2. The S2m concept for each paddle is similar to the one in the

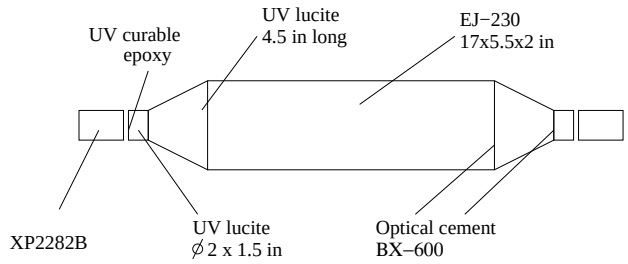

Figure 8: The design of the S2m paddle.

Hall B trigger counters [17]. It has a 2 inch thickness and a simple, trapezoidal light guide on each end (see Fig. 8). The scintillator length of the detector is 43 cm which is shorter than the 60 cm of the existing paddle, but comfortably larger than the Y width of the event distribution at the location of S2. Detector segmentation into 16 paddles leads to a width of each scintillator of 14 cm which allows collection of the large fraction of light with a simple shape for the light guide. We selected fast plastic scintillator EJ-230 [19] (similar to Bicron 420) with a width to the light pulse of 1.3 ns. It has an attenuation length of 140 cm (still much larger than path of the light in the detector). The PMT type (XP2282B [20]) was selected because it has a fast rise time of 1.5 ns and sufficient gain of a few 10^5 at a very competitive cost.

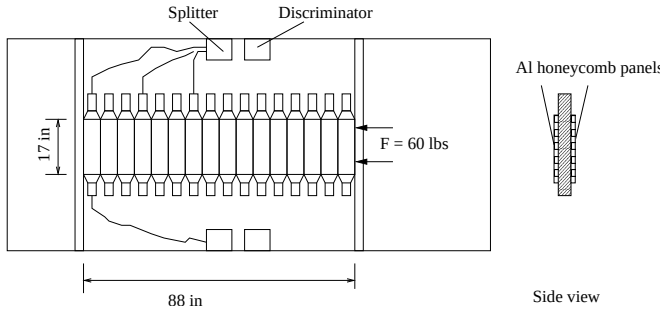

Figure 9: Layout of the S2m plane.

The layout of the paddles is shown in Fig. 9. Two thin aluminum honeycomb panels are used to sandwich the scintillator paddles. The panels allow access to the PMTs and light guides in case the PMT needs replaced without taking full detector apart. The paddles are arranged in the plane without overlap. A force of 60 lbs is applied on the side of the paddles to minimize dead area between adjacent paddles. Individual paddle wrapping consists of 25 μm mylar and 50 μm black tedlar. The wrapping thickness plus measured spacing between adjacent detectors leads to a size for the dead area of 150 - 200 μm.

It was found previously that there is a large content of He in the Hall A

atmosphere which can lead to a dramatic reduction of the PMT life time. To mitigate this problem the PMT is enclosed in a hermetic housing with an input of air which is pumped from outdoor. Figure 10 shows details of the PMT assembly.

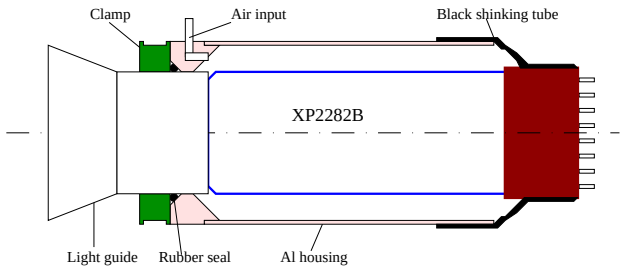

Figure 10: The details of PMT housing.

The anode signal is split into two parts. The main part (90% of the amplitude) is going to the discriminator (a Phillips model 706) with a 10 mV threshold and another signal (10% of the amplitude) to the ADC. Outputs of the discriminator are used for trigger purposes and measurement of the time.

Test results

One paddles was tested on the HRS focal plane where it was connected to channel 4 of the S1 electronics. The observed resolution (sigma) per PMT was 155 ps, which includes contributions from the TDC channel width (100 ns) and jitters in the logical delay line and the discriminator. The MC simulation predicts about 5.7% light collection efficiency in one PMT [21] from which we expected to get 1150 photoelectrons for 20% quantum efficiency of PMT. The observed number of photoelectrons with cosmic rays is about 900 per PMT.

Table 3 shows test results for 26 paddles using cosmic rays with a trigger formed by two narrow (2 cm) counters.

Table 3: Distribution of paddles on time resolution.

resolution (sigma) per PMT, ns	0.140 - 0.175	0.175 - 0.210	0.210-0.245
number of paddles	18	7	1

Acknowledgments

It is a pleasure to thank J. Calarco and W. Hersman for decisive advice in selection of the concept for new trigger detector, E. Pentcheva for preparation of the production drawings, and G. Ron for Monte Carlo simulation of the light collection in the detector.

2.3.3 HRS Optics News

Contributed by J.J. LeRose and J.R. Arrington

New developments in HRS modeling during 2002 include:

- A new, COSY based optics model for the HRS spectrometers was developed. So far, the model uses the nominal effective field lengths and magnet settings, but provides a much improved description of the distribution of events at the focal plane compared to the original SNAKE model (see below). In addition, the optics model has been incorporated into a detailed model of the spectrometer, which includes multiple scattering, apertures, fiducial cuts for the detectors. These models can be used with a stand alone event generator or with SIMC to provide accurate models of the acceptance for a variety of physics processes, with options to model particle decay in flight, energy loss in the collimator, and other processes. With feedback from users and some additional sieve slit measurements, the model can be tweaked to reproduce the small deviations seen with the current starting model (percent level field changes or order 1° magnet rotations). See the SIMC status report for further details.

- Improvements in the SNAKE based model giving transfer functions that more accurately reproduce the measured properties of the spectrometers and hopefully give a more accurate representation of the spectrometer acceptance. Usage is the same as before [22].

- Paul Ulmer and Wendy Hinton have implemented both models of the spectrometers in MCEEP. See the MCEEP status report for further details.

2.4 Data Handling

2.4.1 Hall A Analysis Software

Contributed by J.-O. Hansen

The Hall A object-oriented analyzer

Progress on the new C++/ROOT-based object-oriented Hall A data analysis software continued over the last year, and the project is nearing completion. Development has focused on the high-precision VDC tracking code.

Since October 2001, two new versions of the analyzer have been released. Version 0.65 (April 2002) included the following new features:

- High-precision VDC class incorporating drift-time fitting and multi-track analysis.
- Extended functionality of the global variable system that takes advantage of ROOT RTTI information. In particular, this feature automatically determines the data type of variables and allows definition of variables on data stored in objects and collections of objects (*e.g.* `TList`). Basic function calls on objects are supported as well (*e.g.* `GetSize()`).
- A new multi-purpose apparatus called `THaDecData` that contains miscellaneous decoder data and can be used for quick testing of arbitrary signals connected to the DAQ hardware.

For this release, the source code for the analyzer was put under the CVS version control management system. CVS largely automates the process of merging contributions from multiple developers who are working on the sources simultaneously and maintains a complete history of all changes made.

In version 0.70 (October 2002), another set of essential features was implemented:

- Target reconstruction.
- Improved multi-track handling in the VDC code.
- Preliminary version of a dynamic output module, allowing on-the-fly definition of histograms, ntuples, and tree variables.

Now that target reconstruction is available, the analyzer is in principle suitable for physics data analysis. However, more testing and fine-tuning of the tracking algorithm and calibration databases is required and currently in progress.

Examples of results obtained with the analyzer are shown in Fig. 11 and compared with those from ESPACE. The data for this analysis were taken in September 2000 as part of an optics study with a 9-foil carbon optics target and the standard sieve slit collimator on the left-arm HRS. The beam energy was 825 MeV, the

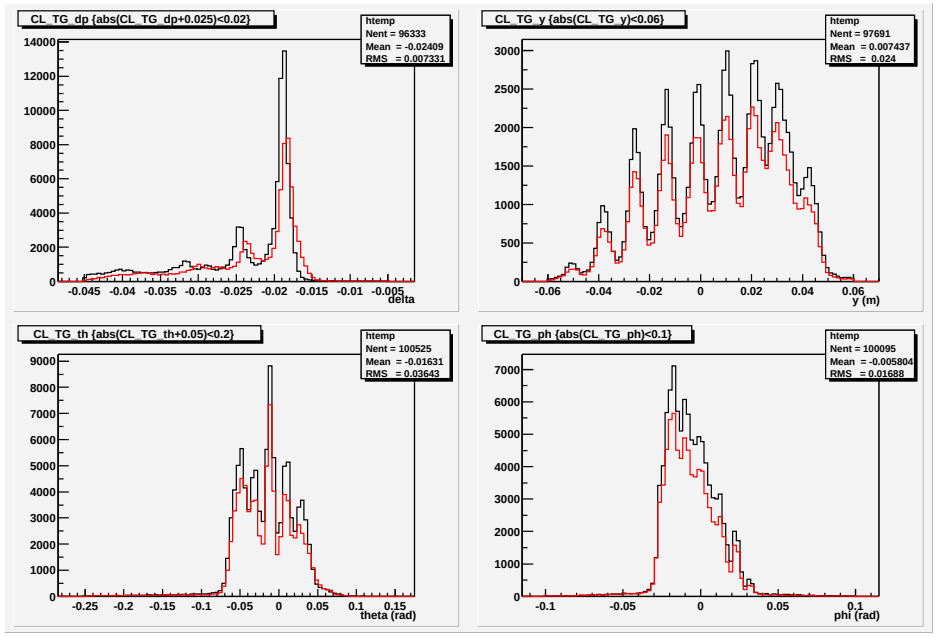

Figure 11: Results obtained with the high-precision VDC tracking code for the reconstructed target quantities δ (momentum), y (in-plane position), θ (out-of-plane angle), and ϕ (in-plane angle). The data are from an optics study that used a 9-foil carbon target and the sieve slit collimator on the left HRS. More details can be found in the text. Black histograms are results from the C++ analyzer, and red (lighter colored) histograms were obtained with ESPACE.

scattering angle, 16°, and the spectrometer central momentum, 838 MeV (elastic kinematics). The same optics database was used for both replays. As one can see, the agreement between two sets of results is generally reasonable although a few problems are evident. In particular, the normalization of the two replays differs, and there is a discrepancy in the scale of the reconstructed momentum (δ). These effects are significant. of course, and must be resolved before committing the C++ analyzer to production. Figs. 12 and 13 show the reconstructed sieve slit pattern for the C++ analyzer and ESPACE replay, respectively. The agreement is excellent, suggesting that the angular reconstruction works well.

Furthermore, before the analyzer is ready for production, it will be highly desirable to add several features to the program that are still missing. These include

- standard "physics" classes, *i.e.* code that calculates basic kinematical quantities such as Q^2;
- more sophisticated standard detector classes (*e.g.* timewalk corrections, PID);
- analysis steering with dynamic cuts/tests;

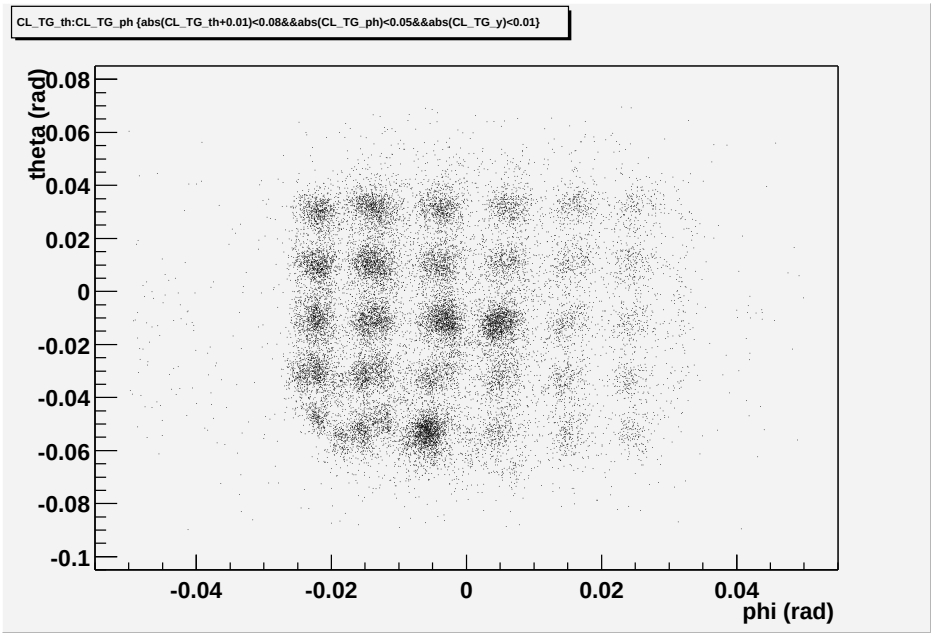

Figure 12: Sieve slit pattern reconstructed with the C++ analyzer. The data are from the same run as those in Fig. 11. Only events originating from the center target foil ($|y_{tg}| < 0.01$) are included.

- improved database system with more efficient handling of time-dependent data;
- support for `autoconf` to simplify the build process on different platforms.

In addition, extensive testing must be done, and documentation must be written. The current plan is to have the C++ analyzer ready for production analysis in the spring of 2003.

Up-to-date information about this project can be found on the Web [23]. Manpower is tight, and volunteers are welcome to join, especially those with a good background in C++ programming. The work reported here was carried out in collaboration with R. Michaels from Hall A and ERULF summer student S. Dobbs from CMU.

ESPACE

Our current FORTRAN-based analysis software ESPACE saw one major development over the past year. The new "left/right" spectrometer naming conventions were finally implemented in the official version of the software thanks to the efforts of Werner Boeglin at FIU (some preliminary contributions came from Mark Jones (JLab) and Wang Xu (MIT)). Since this is a significant change, we decided to bump up the version number of ESPACE to 3.0. ESPACE 3.0 requires that all

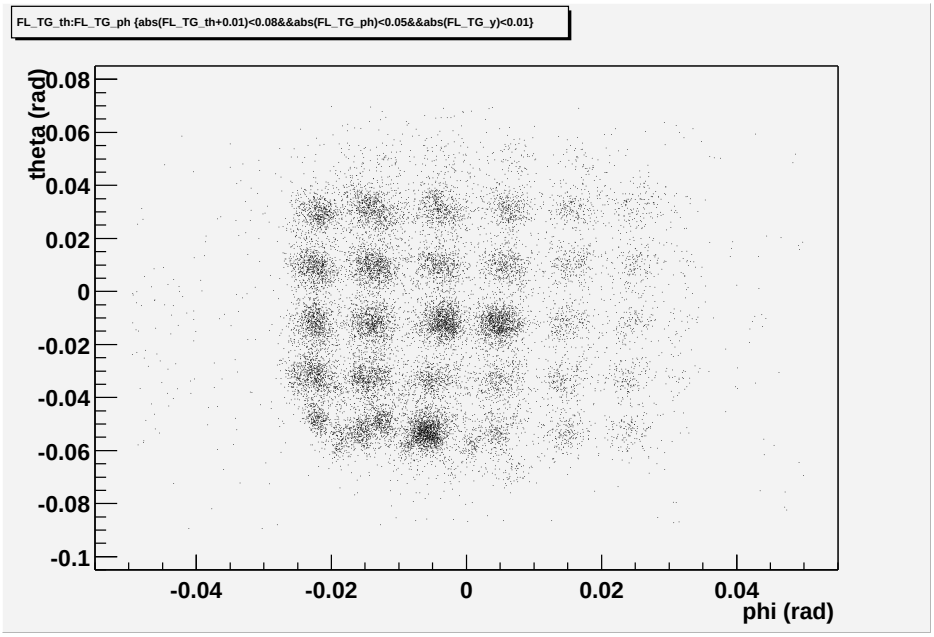

Figure 13: Sieve slit pattern reconstructed with ESPACE using the same analysis parameters as with Fig. 12.

input files (*e.g.* header files, databases) follow the new naming conventions. Old input files do not work with the new version, but can be converted to the new scheme relatively easily.

In addition, ESPACE 3.0 includes various smaller improvements:

- Support for raw data input from the online ET system.
- Improved target energy loss correction.
- Support for a second aerogel detector in each spectrometer arm.
- Support for the pion rejector in the left HRS.
- Support for analysis of two-hadron or two-lepton coincidences.
- Ability to write summary files to a subdirectory, which helps organize analysis output better.
- Additional methods to fit and extract BPM and raster information.
- Better error reporting. Indicates which input file cannot be opened instead of crashing with a cryptic "system error" on Linux.
- Ability to trap floating point errors under Linux if compiled for debugging.

Finally, as with the C++ analyzer, the ESPACE source code has been put under CVS version management control to improve code maintainability and provide automatic documentation of changes. ESPACE 3.0 is currently available from CVS only [24]. We are planning to make the code "officially" available for direct download in November 2002 as we have not yet finished all quality checks.

The track fitting algorithm used in ESPACE has been documented in a section of the upcoming Hall A NIM article [18]. This information will also be made available (in slightly more detail) as a Hall A Technical Note in the near future.

Several items remain on the to-do list for ESPACE: Jeff Templon's suggested FORTRAN code cleanup, Werner Boeglin's faster track fitting routines, new compiler support, a more flexible database format, and improved documentation. Volunteers for these projects are, as always, welcome.

2.4.2 MCEEP

Contributed by P.E. Ulmer

MCEEP [25] is an experiment simulation program, primarily for $(e, e'N)$ reactions, but can also be used to simulate other coincidence reactions as well as single arm elastic and inelastic electron scattering experiments. It incorporates energy loss and multiple scattering effects in target and window materials, internal bremsstrahlung, beam intrinsic spot size and rastering, specification of fairly general detector or spectrometer systems and a variety of physics models for $(e, e'N)$ reactions and (e, e') elastic scattering. In addition to allowing a general spectrometer line to be defined via a stack of elements, including drifts, rotations, transfer functions and mispointing and resolution effects, it includes routines specific to the Hall A setup. These include various Hall A target geometries, magnetic and aperture models for the high resolution spectrometers and resolution/scattering effects in the focal plane vertical drift chambers. In addition, ejectile spin precession in included via a COSY [26] based optics model. The program can run on several Unix platforms, including Linux (g77, Absoft f77 and SGI), Sun, HP, OSF1 (Alpha) and DEC-Ultrix. A MCEEP self-extracting installation package, along with detailed documentation, can be downloaded from the Web [27].

Considerable progress has been made in the past few years on MCEEP. The program has now reached the sophistication required to make detailed comparisons of theory with experiment. Below, I describe only those features implemented since the previous Hall A Status Report.

The magnetic and aperture models for the Hall A high resolution spectrometers were incorporated previously via transfer functions fit to pseudo-data generated from a SNAKE based raytracing model [28]. The initial implementation gave transverse coordinate distributions at the spectrometer focal plane which disagreed substantially with those taken directly from data (see Fig. 14). Recently, an ad hoc modification to this model was made [28] to improve the agreement

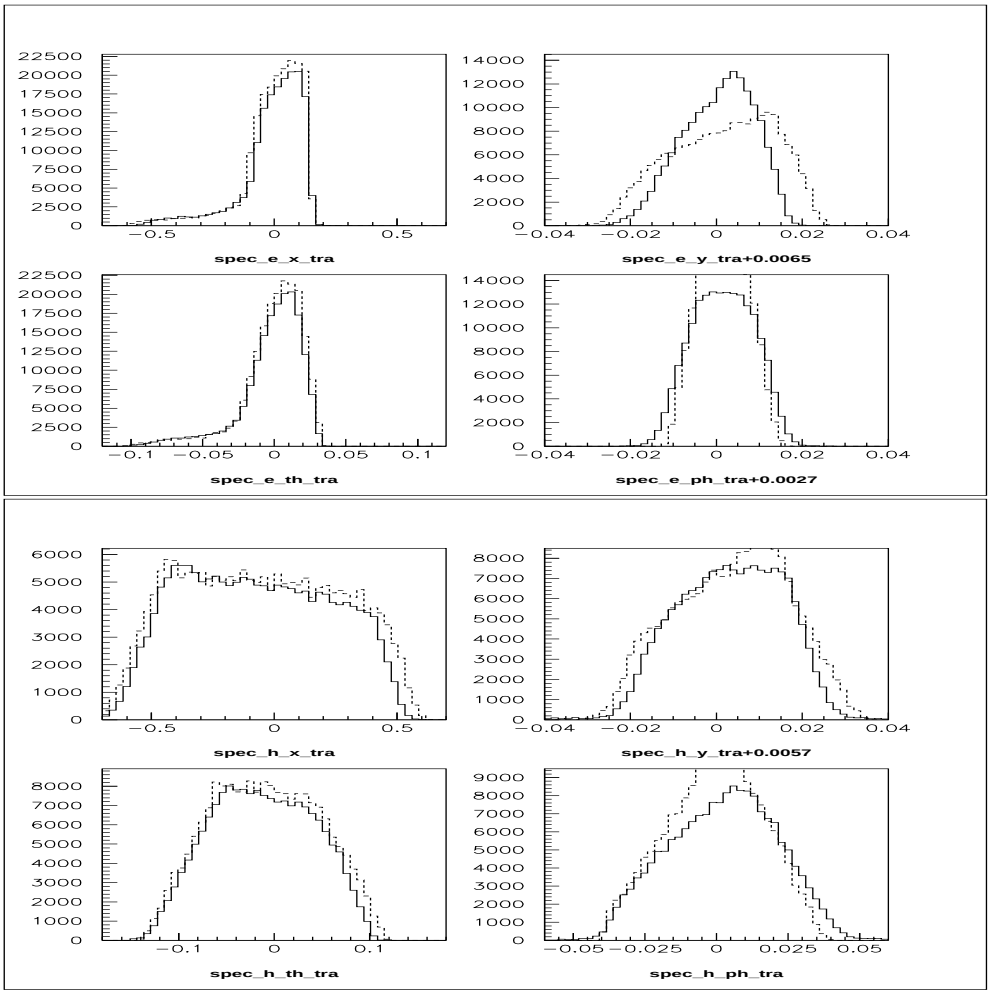

Figure 14: Focal plane distributions for the electron (top) and proton (bottom) arms in H$(e, e'p)$. The coordinates refer to the standard Transport system which is the plane perpendicular to the central ray. The solid histograms are for the data and the dashed are for MCEEP using the **old** SNAKE based transfer functions. Note that some of the data distributions have been offset slightly to account for spectrometer misalignments.

with data (see Fig. 15). The figures compare data and MCEEP for the H$(e, e'p)$ reaction taken with a 15 cm liquid hydrogen target at $Q^2 = 0.67$ (GeV/c)^2 (a calibration measurement for Experiment E94-004 [29]) using the old and the new transfer functions. The data have been corrected for computer deadtime and VDC tracking efficiency (target boiling corrections and electronic deadtimes are estimated to be negligible). All simulations used the dipole proton form factors. This measurement was taken with the nominally 6.0 msr collimators at the entrance of each spectrometer with electrons detected in the LEFT spectrometer

and protons in the RIGHT. For these data, the proton arm limits the coincidence acceptance, so that the electron variables are not completely filled. The elastic kinematics constraints also imply that the proton acceptance is not completely filled either, as the proton momentum and angle are correlated. While, admittedly, the H$(e, e'p)$ reaction is not the ideal candidate for such a study due to these correlations, this does clearly show the improvement in the spectrometer optics model. Recently, an alternate, COSY [26] based, Hall A spectrometer model was

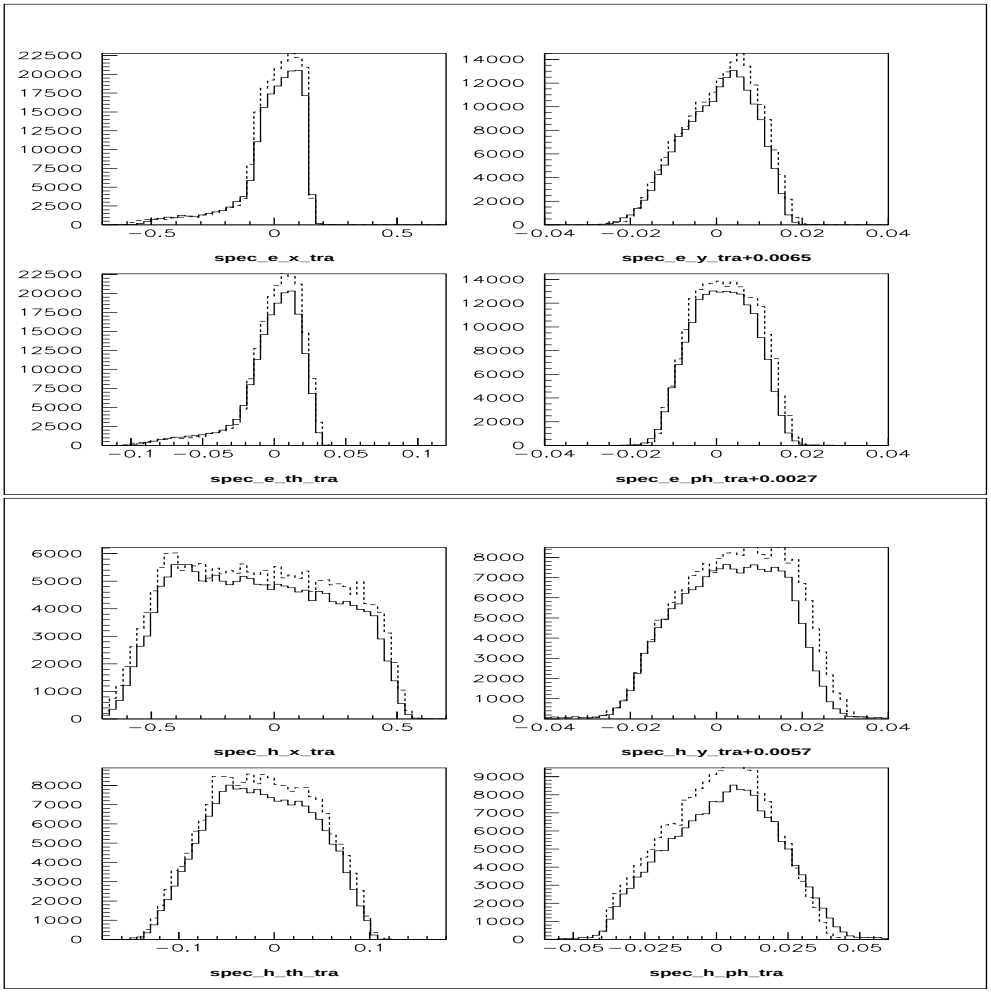

Figure 15: Focal plane distributions for the electron (top) and proton (bottom) arms in H$(e, e'p)$. The coordinates refer to the standard Transport system which is the plane perpendicular to the central ray. The solid histograms are for the data and the dashed are for MCEEP using the **new** SNAKE based transfer functions. Note that some of the data distributions have been offset slightly to account for spectrometer misalignments.

incorporated into MCEEP (based on the Hall A HRS COSY model in SIMC, a

monte carlo simulation program that has been used for several Hall C experiments, and recently modified to simulate Hall A experiments). The version of MCEEP incorporating the COSY spectrometer model is not quite ready for distribution, but has been used to perform a preliminary comparison to the same data set as mentioned above, as shown in Fig. 16. As opposed to the older transfer functions, the COSY model and the updated transfer functions are in reasonable agreement with these data. Ratios of the integrated coincidence yield for the data to each of the models are shown in Table 4. It is seen that, while the distributions at the focal planes may differ, the integrated yields are nearly identical, at least for this particular measurement on $\mathrm{H}(e, e'p)$.

Model	Data/MCEEP
SNAKE-old	0.904
SNAKE-new	0.891
COSY	0.891

Table 4: Ratios of the coincidence data yield data divided by the MCEEP yield for each of the optics models. All simulations used the dipole nucleon form factors.

In addition, the "R-functions" [30] were updated in accord with the new SNAKE based transfer functions. The R-function variable is defined by the distance in radians from a predefined acceptance contour in the target θ and ϕ coordinates at each of a set of grid points in y and δ. Positive values of R imply points within the contour and negative values imply points outside the contour. (By defining a cut in R, one can reject all events from a fixed distance from the contour, thus removing the poorly understood acceptance edges in a more efficient manner than with ordinary "rectangular" cuts.) Distributions of R are shown in Fig. 17 for the old transfer functions, the new transfer functions, the COSY model and for the data (where the values of R for the data were derived using the updated SNAKE model). Again, these results are for the $\mathrm{H}(e, e'p)$ measurement with the 6.0 msr collimators in place. (Whereas, all previous results included only computer deadtime and VDC tracking efficiency corrections to the data, here, the data have been further scaled by a factor of 1.11.) Finally, the ratio of the R-function distribution for each model to that of the data is shown in Fig. 18.

Other improvements in MCEEP over the past year include:

- To cope with the new column-wise Ntuples generated by ESPACE, the MCEEP utility suite was updated to allow adding R-function values to existing column-wise data Ntuples (addition of R-functions to row-wise Ntuples was available previously).

- An aperture and magnetic model (forward only) for the MAD spectrometer and a model of the Hall A polarized ^{3}He target were added.

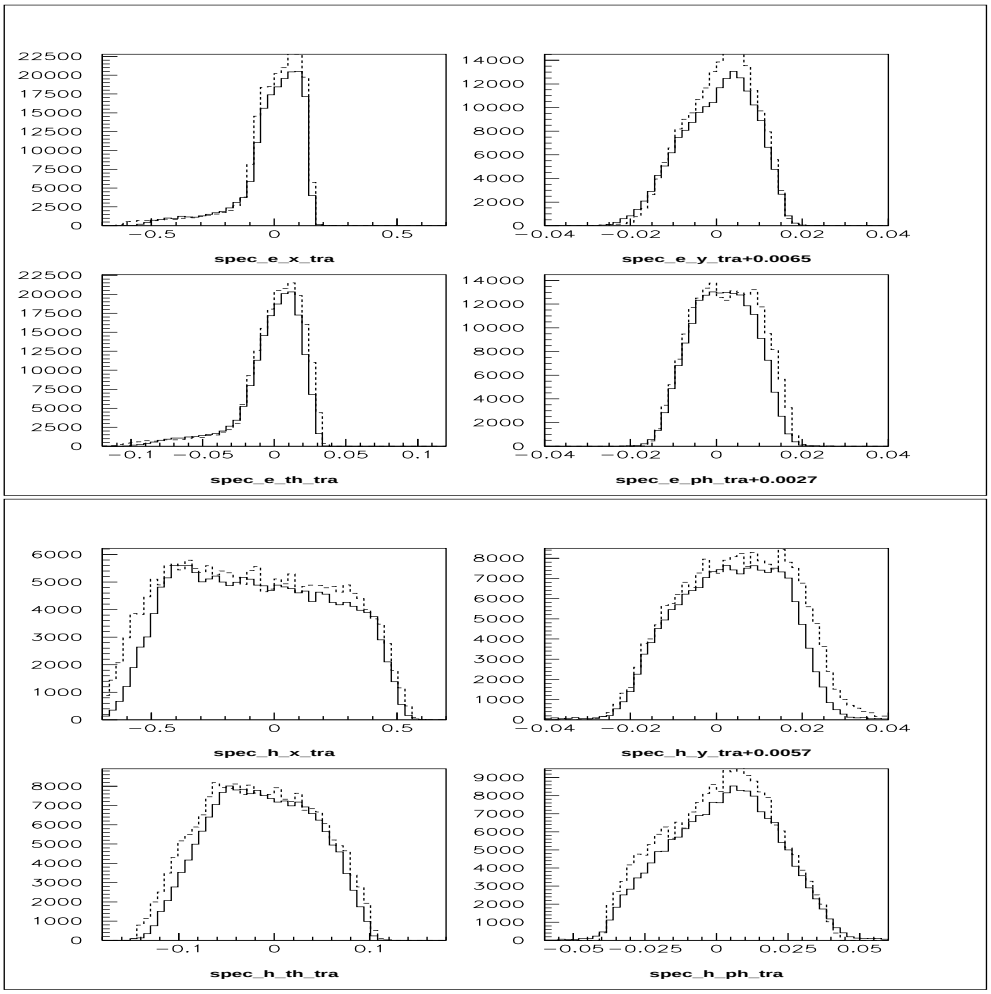

Figure 16: Focal plane distributions for the electron (top) and proton (bottom) arms in H$(e, e'p)$. The coordinates refer to the standard Transport system which is the plane perpendicular to the central ray. The solid histograms are for the data and the dashed are for MCEEP using the recently implemented COSY model. Note that some of the data distributions have been offset slightly to account for spectrometer misalignments.

- A set of tools to analyze kinematics related systematic uncertainties was included in the utilities suite. This allows determination of the derivatives of the cross section with respect to each kinematic quantity from a single Ntuple, properly weighted by acceptance.

I would like to acknowledge the following people who have contributed to the development of MCEEP throughout the years. Thanks to Mina Nozar for her work on the spectrometer analysis routines, to Douglas Higinbotham, Garth Huber, Robert Lourie, Pete Markowitz, Liming Qin, Scott Van Verst and Glen War-

ren for providing some of the physics routines, to Franck Sabatie for work on implementation of the beam raster, to Luminita Todor for work on the radiative effects, to Steffen Strauch for work on the scattering plane polarization observables and to Sabine Jeschonnek for providing her PWBA d$(e, e'p)$n model and documentation. I thank Kevin Fissum for providing code and figures for the ^{16}O spectral functions from Udias and for the ^{208}Pb spectral functions from Lapikas. I also thank Mark Jones for work on the schwinger correction routine and for incorporating COSY spin transport and Joe Mitchell for providing the perl script to process the Arenhövel response function files. I thank John LeRose for providing the HRS spectrometer magnetic-aperture model and also the R-function routines. I thank Kathy McCormick for writing the Hall A MAD spectrometer routines and for incorporating the Hall A ^{3}He polarized target. I thank Riad Suleiman for incorporating the Hall A He tuna can target cells. Thanks to Wendy Hinton for incorporating the COSY based spectrometer models from SIMC and to Dave Meekins for his work on the original COSY routines for Hall A. Finally, I thank Mike Finn for many useful discussions.

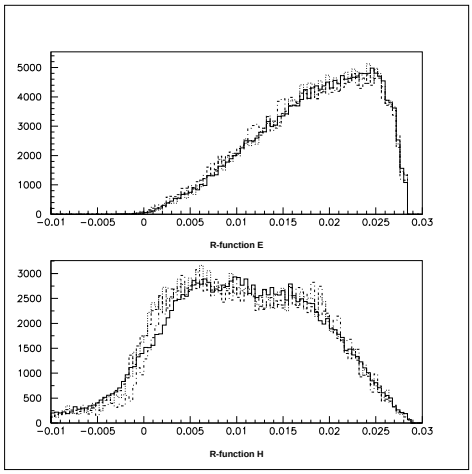

Figure 17: Distributions of the R-function values for the electron arm (top) and proton arm (bottom) for the old (dashed histogram) and new (dotted histogram) SNAKE based transfer functions, for the COSY model (dot-dashed histogram) and for the data (solid histogram). For the data, the updated R-functions were used. All results are for the 6.0 msr collimators. The data have been scaled by a factor of 1.11 to bring the integral into rough agreement with the simulations.

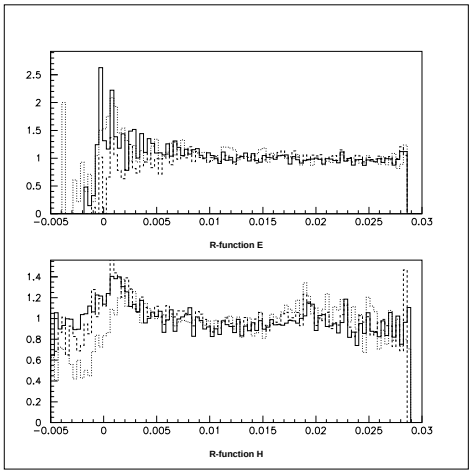

Figure 18: Ratio of the R-function distribution for each model to that of the data. The top panel shows the distributions for the electron arm and the bottom for the proton arm for the old (solid histogram) and new (dashed histogram) SNAKE based transfer functions and for the COSY model (dotted histogram).

2.4.3 SIMC

Contributed by J. Arrington

SIMC is a physics simulation code that has been used extensively in Hall C over the past several years. It has been used to model proton and nuclear elastic scattering, quasielastic scattering, and pion and kaon electroproduction from hydrogen and nuclear targets. In addition, it can be relatively easily modified to be used for other reactions (and in fact has already been done so for the N $\rightarrow \Delta$ measurements upcoming in Hall C next year). Last year, models of the HRS spectrometers were added, making it useful for simulating Hall A experiments. It has already been used for the analysis of one Hall A experiment, E99-008 [31], and is currently being used in the analysis of several others.

In addition to generating events and applying cross section weighting for the various reactions mentioned above, SIMC also applies energy loss, radiative corrections, multiple scattering, coulomb corrections, and particle decay. Detailed models of the HRS spectrometers are included, using a COSY generated model of the optics, along with apertures at each magnet and fiducial cuts for the detectors in order to generate the acceptance. Final-state interactions and collimator punch-through have also been modeled in SIMC, but are not included as default options, because special care to disentangle these contributions from the underlying cross section must be taken if they are used. Additional details and discussion of SIMC features (slides from the analysis workshop) can be found on the Hall A web site: hallaweb.jlab.org/data_reduc/AnaWork2001/johna. The latest version of SIMC and the COSY-based HRS models can be found at: www.jlab.org/~jroche/simc or www.jlab.org/~johna

While designed as a coincidence Monte Carlo, it can be used for single arm reactions by either disabling cuts on one arm, or by using a single-arm event generation code with the HRS model used in SIMC. There are two such single-arm event generators already available, one for acceptance studies (white spectrum event generation), and one used for the deuteron photodisintegration process. Because the event generation is independent of the spectrometer models, the HRS models can be turned off, allowing large detectors to be modeled with geometric cuts, or one of the HRS subroutines can be replaced with either simple or detailed models of new detectors.

SIMC generates events, applies cross sections, and folds in resolution, acceptance, and other effects in a way that is generally similar to MCEEP, although there are several differences in the details of how these are accomplished. At this point, there are no detailed comparisons of the physics included in the codes, because the biggest difference between them at the moment is related to the models of the spectrometer optics. The COSY model better matches the optics of the spectrometers than the original SNAKE transfer functions, clearly improving the distribution of events at the focal plane. The COSY-based model of the

spectrometer is being incorporated into MCEEP, along with an updated set of SNAKE transfer functions (see section on HRS updates). With all three models in MCEEP, we can directly compare the different optics models and apertures used to define the acceptance, in order to optimize the HRS models. Then it will be possible for experiments to make more direct comparisons of MCEEP and SIMC, both to compare the two codes, and to provide independent checks of the physics included in the Monte Carlos.

There are still small details that need to be checked in the Hall A version of SIMC. We have included but still need to double check some parameters related to the target geometry, spectrometer entrance/exit windows, and magnet apertures. In addition, after comparisons to new data have been made, the COSY-based optics models can be improved. Focal plane distributions from sieve slit runs indicate that small tweaks are necessary in the optics model. Small magnet rotations and adjustments to the fields appear to be necessary to improve the detailed agreement of the distributions at the focal plane. Once the starting model has been checked more carefully to existing data, and additional calibration data is taken, we can complete the optimization of the COSY model. If we can reproduce the HRS optics at the same level as has been done for the HMS, the acceptance model should be good enough that it will not be necessary to apply tight cuts to the data in order to understand the acceptance. This is especially important for experiments which measure absolute cross sections, but cannot afford to lose a large part of the data to acceptance cuts.

SIMC is based on the NE18 Monte Carlo code, developed by Tom O'Neill and Naomi Makins. Thanks to Dave Meekins, Rolf Ent, and Dave Potterveld for their work on the HRS model, and to Elaine Schulte, Mitzi Boswell, and Okechukwu Okafor for their work on incorporating the model into SIMC and debugging the results. Thanks also to the long list of students, postdocs, and faculty/staff members who have (willingly or unwillingly) helped to develop and debug the simulation code over the years.

Specific Instrumental Developments

3 Specific Instrumental Developments

3.1 Operational Systems

3.1.1 Dual Analyzer in Hall A FPP

Contributed by M. Jones

Efforts have been undertaken to increase the figure-of-merit (the efficiency times the square of the analyzing power) of the focal plane polarimeter (FPP) in the Hall A left arm spectrometer. In E99-007, which extended the measurement of $\mu G_{Ep}/G_{Mp}$ to $Q^2 = 5.6$ GeV^2, polyethylene (CH_2) was used instead of carbon as the analyzer for the FPP. CH_2 (about 56 cm thick) was placed between the carbon doors and ,in addition, CH_2 (about 44 cm thick) was mounted on a holder in front of the carbon doors. This gave a 100 cm thick CH_2 analyzer between front and rear FPP chambers. The increased figure-of-merit made it possible to do a measurement of *ep* elastic polarization observables at proton momentum of 3.8 GeV/c .

Subsequent to this experiment, it was proposed to build a FPP in Hall C to extend the measurement of $\mu G_{Ep}/G_{Mp}$ to larger Q^2 [32]. The new FPP will consist of two analyzers in series with chambers before and after each analyzer , a dual analyzer. Measurements at Dubna proved that the analyzing power and efficiency were relatively constant when the CH_2 thickness was increased from 40 to 86 cm at a proton momentum of 3.8 GeV/c [33], which supported the idea that it was better to have two analyzers in series rather than one very thick analyzer.

One part of E99-114, the Real Compton Scattering experiment, was measuring the polarization of the outgoing proton at one kinematics. To improve the figure-of-merit of the FPP, it was decided to try the dual analyzer approach by moving the 44 cm thick CH_2 between the VDC and the front FPP chambers while still using the carbon for the second analyzer. The ESPACE software was modified so that scattering angles of the protons in the first CH_2 analyzer could be determined from the VDC track and the track in the first set of FPP chambers while retaining the ability to determine the scattering angles of the protons in the second carbon analyzer. An *ep* elastic measurement was done at $Q^2 = 4.1$ GeV^2 (momentum of 2.98 GeV/c) to calibrate the analyzing power of the carbon and CH_2. In the top plot of Fig. 19, the analyzing power of CH_2 and carbon are plotted as a function of the proton scattering angle. In the middle plot in Fig. 19, comparison is made to analyzing powers measured during e99-007 using 100 cm thick CH_2 at about the same proton momentum. The analyzing power is the same for both thickness which confirms what was measured at Dubna. In the bottom plot, the comparison is made to earlier measurements of the analyzing power of carbon from E93-027 at lower proton momentum. The analyzing power for carbon is dropping off with higher proton momentum. For the carbon scattering events, a cut was placed to restrict the scattering angle in the CH_2 to be smaller than one degree (these

events should mainly be multiple scattering in the CH_2). Studies have to be undertaken to determine whether this is the optimal cut to maximize the FPP's figure-of-merit. A more thorough offline analysis is almost complete.

Recently, in E00-007, "Proton Polarization Angular Distribution in Deuteron Photodisintegration", the dual analyzer FPP system was used for a wide range of proton momentum. Therefore, there should be a database of figure-of-merits for the dual analyzer FPP over a range of proton momentum to help plan future

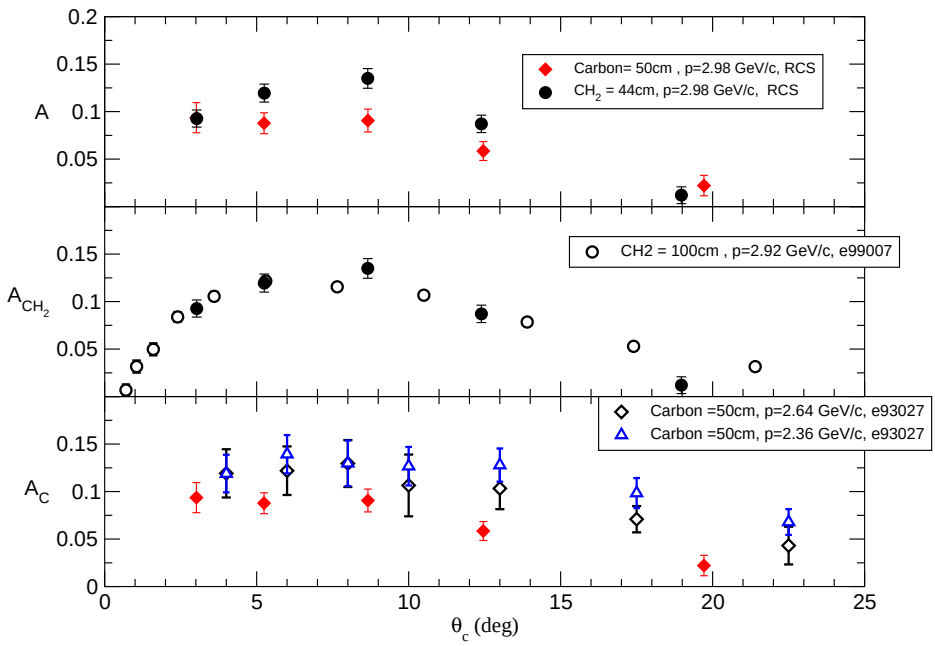

Figure 19: Online, preliminary analyzing power data for e99-114. The top plot shows the analyzing power for CH_2 (carbon) versus scattering angle of the proton in the CH_2 (carbon) with the dual analyzer in RCS. The middle plot compares the analyzing power for CH_2 measured in RCS to previous measurement during E99007. The bottom compares the analyzing power for carbon measured in RCS to previous measurement during E93027.

3.1.2 RCS Calorimeter Performance and Future Applications

Contributed by B. Wojtsekhowski for the E99-114 Collaboration

A 704 block lead glass calorimeter was constructed for use in experiment E99-114. The resolution and other characteristics are presented.

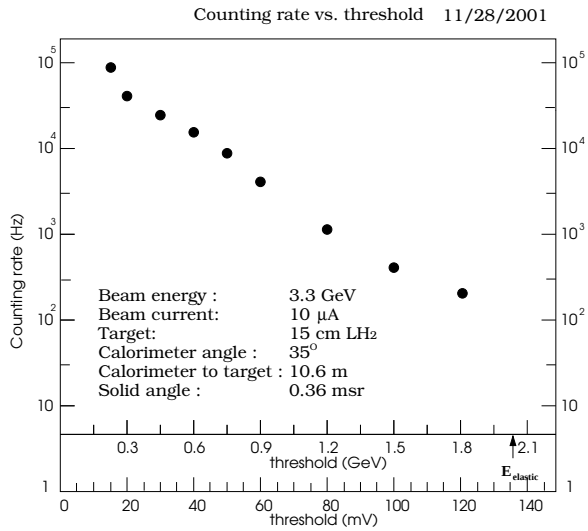

Figure 20: The rate of the signal from 25 block calorimeter vs. threshold.

Introduction

Exclusive reactions at high s, t, and u such as elastic electron and photon scattering from nucleon, pion electro-production, and pion photo-production provide valuable information about Generalized Parton Distributions [34]. To obtain data at high momentum transfer, an experiment must run at large luminosity and use large acceptance detectors. In 1998 in the Hall A an experimental study was done on the rate and signal spectra from a lead glass calorimeter [35] (see Figure 20). It demonstrated that for elastic reactions the luminosity of 10^{38} Hz/cm^2 can be used with large solid angle calorimeter. This report presents characteristics of the large calorimeter in long experiment [36].

Calorimeter

Figure 21 shows the geometry of the RCS calorimeter. It has 22 columns and 32 rows. The front end electronics were located close to the calorimeter. A trigger signal was prepared based on the sums, each of which combined signals from 32 PMTs, whose overlaps insured trigger efficiency. The trigger signal was send to DAQ location via 34 m fast RG-8/U cable, while the analog signals from each PMT were connected to the ADC via 100 m RG-58 cable.

The lead glass block has dimensions 40x40x400 mm. PMT FEU-84/3 was attached with optical grease BC630 and pressed to the lead glass with the force of 1 lbs. Individual lead glass blocks were wrapped in aluminyzed mylar film with thickness 25 μm and black tedlar film with thickness 50 μm. PMTs were equipped with high current (1 mA) high voltage divider to insure linearity of the response.

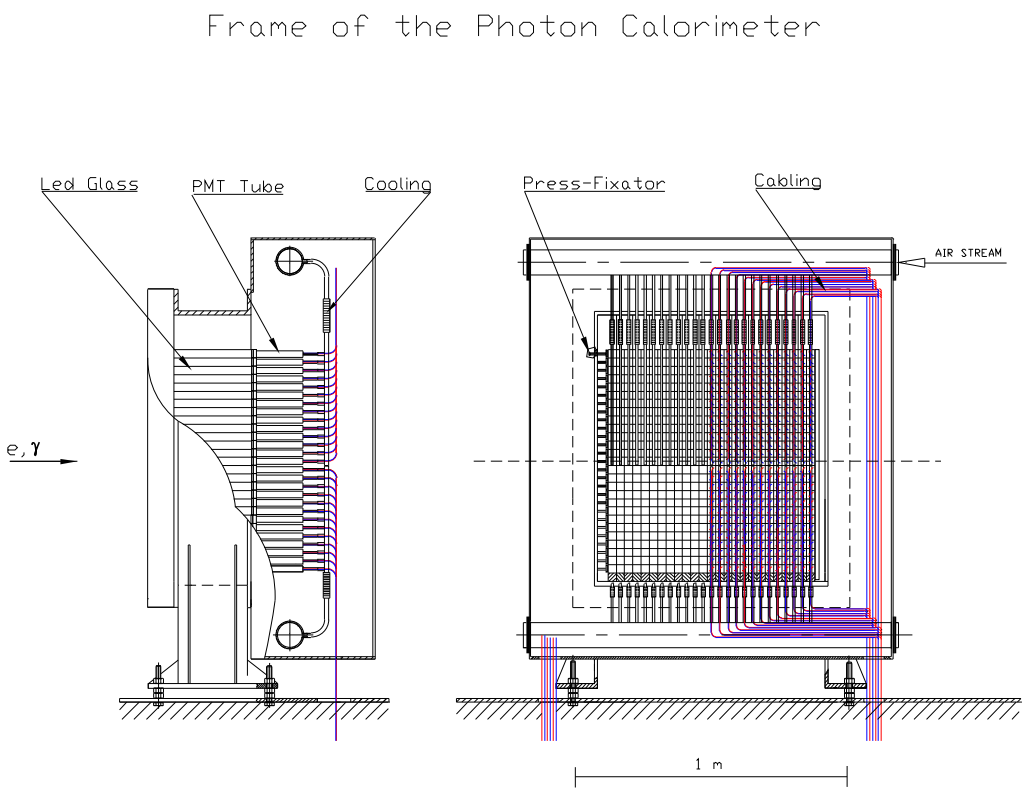

Figure 21: The geometry of RCS calorimeter.

Calibration

Initial calibration of the blocks was done using cosmic rays. About 24 hours is required to collect sufficient statistics. It took 3-4 iterations to match the signals. A fix power gain parameter ($ln(A)/ln(U)$) of 7.5 was used for all PMTs. Calibration by elastic electron scattering was done several times during RCS experiment. The first time HV settings were corrected the most: the PMTs gain were changed up to 30% from the cosmic calibration values. Figure 22 shows the HV settings after the calibration at the beginning and at the end of experiment. The calibration scale, which was 1 MeV per ADC channel at the beginning experiment, was increased to 1.5 for the last calibration run.

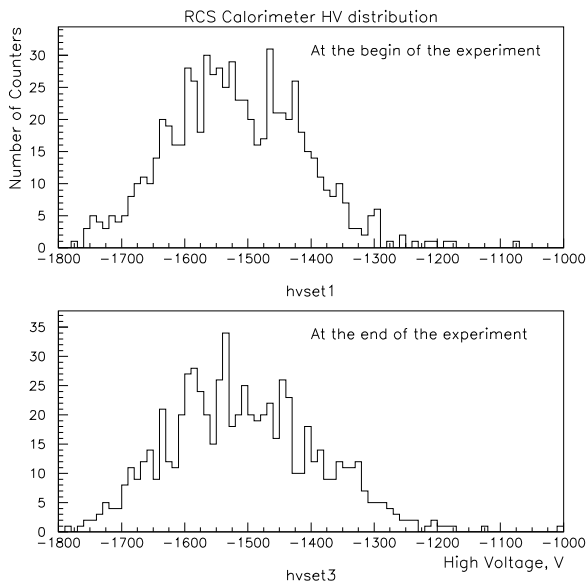

Figure 22: The HV settings for calorimeter PMTs.

Operation

During the experiment, the PMT amplitude spectra were monitored via on-line and off-line analysis codes. Figure 23 shows the on-line result for the pedestal widths for all 704 lead glass blocks. For estimate of the luminosity important to take into account that the radiator (6% radiation length) increases the rates by a factor of 3.

Table 5 shows the history of energy resolution during experiment E99-114. Observed loss of energy resolution is due to radiation damage of the lead glass. Total dose was estimated to be 3-6 krad base on the average width and shift of the pedestals. Because radiator triples the radiation level, one can find that observed radiation effects correspond to 500 hour experiment with a 15 cm LH target and

Table 5: Calorimeter energy resolution.

Runs	Average Energy, GeV	Sigma(E)/E, %	1 GeV %	beam μA	accumulated beam charge, Coloumb
1488	1.32	4.9	5.5	5	0
1811-12	2.78	4.2	7.0	2.5	2.4
1811-18	2.78	4.6	7.7	2.5-20	2.5
1930	3.39	4.2	7.7	40	4.4
2125	2.83	4.9	8.2	25	6.6
2593	1.32	9.9	11.3	38	14.9
3365	1.31	8.4	9.6	41	29.2

50 μA beam. The transparency of 20 lead glass blocks after experiment is shown in Figure 24. This measurement was done with blue LED $\lambda_{max} = 430\,nm$ and Hamamatsu photo diode S1226-44.

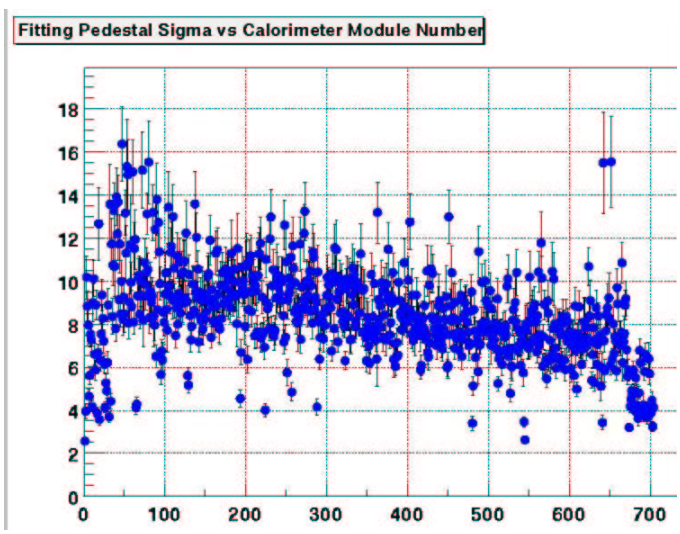

Figure 23: The ADC pedestal width for individual PMTs for the run 2293 with the calorimeter at 37°, on 8.8 meters from the target, beam energy of 5.76 GeV, beam current of 30 μA, and a 15 cm LH2 target with 6% X_0 radiator.

Future Applications

There are exciting possibilities of new experiments based on the use of the lead glass calorimeter. It includes a second RCS experiment in Hall A for mapping of the polarization transfer parameters, several pion production experiments, and elastic form factor measurements.

For example, the experiment on polarization transfer in pion photo-production at large s and t, which is presently limited to the very tip of the photon spectra,

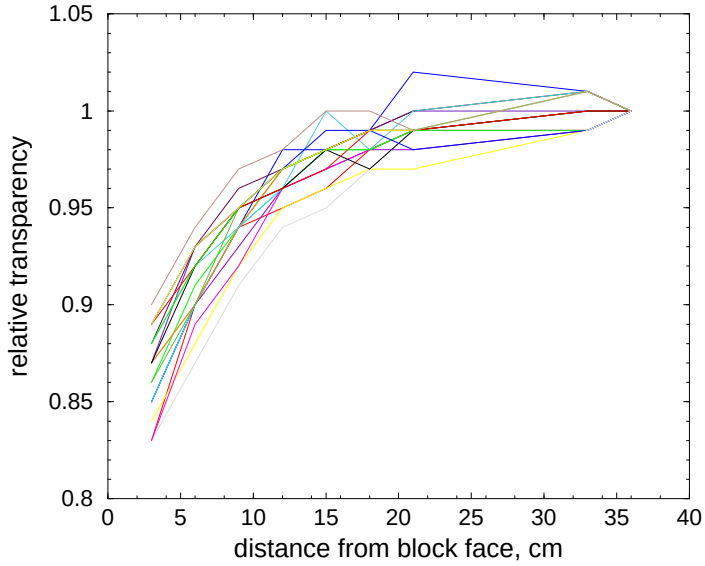

Figure 24: The blue light attenuation in 4 cm of the lead glass vs distance from the front face for the block.

can use a much wider photon energy range and gain about one order of magnitude in counting rate. Due to the large size of the calorimeter, both photons from π^o decay are detected (see Figure 25) which allow clean identification of the exclusive reaction. Use of wide range of photon spectra in pion photo-production allows one to measure the cross section and polarization transfer parameters in the γ, π^o reaction with small steps of the photon energy without adjustment of the electron beam energy. For measurement of the elastic form factors of nucleon (light nuclei) segmented calorimeter can be used as an electron detector. Due to good position resolution and large distance from the target, it can provides quite accurate determination of the scattering angle when the recoils detected in HRS. This way to measure electron scattering angle has accuracy of 0.1 mrad or less of each event and systematics can be few times smaller which is needed in Rosenbluth technique. The calibration of the magnetic optics via elastic ep scattering with lead glass calorimeter is a plan for ChPT experiment E01-014. From electroproduction of π^o in regime of low momentum of the recoil proton and large Q^2 this large calorimeter allow to get data on Deep Virtual Meson Production.

The present calorimeter will be a part of larger assembly "BigCal", which under construction by GEP -III collaboration. The BigCal configuration can be installed in Hall A.

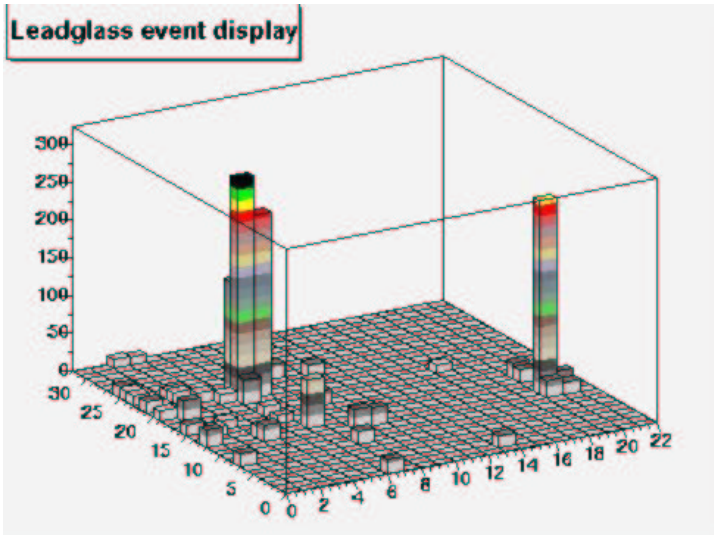

Figure 25: The event display with the pion event. Configuration : beam energy is 3.48 GeV, beam current is 3.5 μA, 15 cm LH target with 6% X_0 radiator, proton spectrometer has $\theta_p = 45.7^o$, $P_p = 1.254$ GeV/c, calorimeter position is 31° at distance of 4 meters from the target, trigger in the calorimeter has threshold at $E_{calo} > 390$ MeV.

Conclusion

The highly segmented lead glass calorimeter is a powerful new instrument for Hall A high luminosity experiments.

3.1.3 The Hall A RICH Detector

Contributed by F. Garibaldi

A RICH detector is needed for strangeness physics in Hall A. In fact it has been shown [37,38] that the standard Hall A hadron identification (TOF and 2 aerogel threshold Cherenkov detectors) is not sufficient for unambiguous kaon identification, especially in the presence of high pion and proton background. A CsI/freon RICH that provides superior PID performances has been built and succesfully tested at CERN (November 2000). The description can be found in the 2001 Hall A Report [38]. Significant progress has been made in 2002 in understanding the photocathode Quantum Efficiency (QE) and the detector performances [39,40].

CsI Evaporator Facility

A dedicated facility has been used for CsI evaporation.(Fig. 26) It consists of a cylindrical stainless steel vessel (110 cm height, 120 cm in diameter) equipped with four crucibles containing CsI powder. The pumping system easily reaches a vacuum of a few 10-7 mbar in less than 24 hours. The prepolished pad plane (a

printed circuit with three layers of metals, nickel, copper, and gold, glued on the vetronite substrate) is housed in the vacuum chamber and heated to 60(, usually for 12 - 24 hours. The location of the crucibles with respect to the photocathode and their relative distance are optimized to ensure a minimun variation in thickness of 10each crucible. The CsI powder evaporates at a temperature of 500(. Since H2O vapor severely affects the performance of the CsI layer, the assembling of the pad planes in the RICH structure is always performed in an argon atmosphere. Following the prescription of the ALICE HMPID evaporation system, we have operated our system in such a way to deposit a 300 nm CsI film. This thickness has been chosen to guarantee "safe" operation of the photocathode. In fact no difference in QE has been observed in the 150 ? 700nm range. The thickness of 300 nm is a compromise for having a 'stable' photocathode, while avoiding charging up problems at high radiation fluxes. An evaporation speed of 2 nm/s has been chosen as a compromise between the need to avoid CsI disassociation (high crucible temperature, high speed) and the need to avoid residual gas pollution on the CsI film surface.

On Line QE Measurement Device

In order to monitor the quality of the evaporation and its uniformity, an on-line QE measuring system has been built and successfully employed for the first time on

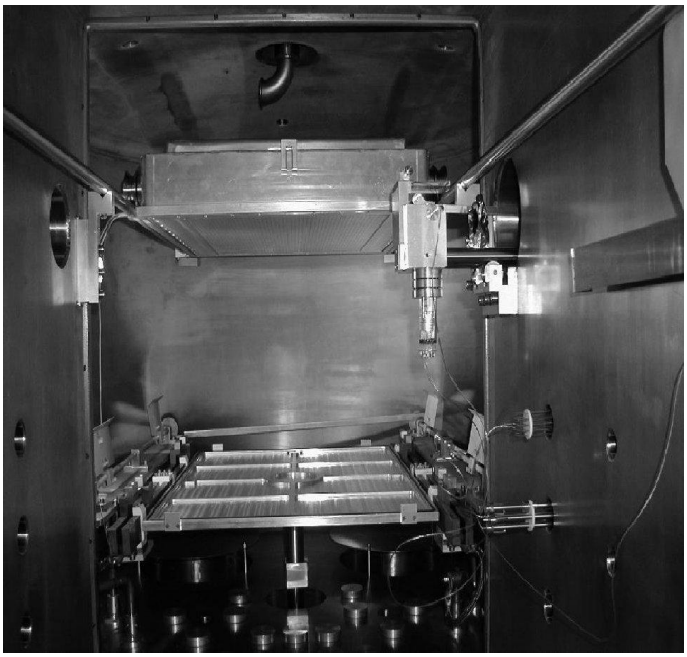

Figure 26: The evaporation facility.

large area CsI photocathodes (Fig. 27). A movement system allows mapping out the entire photocathode. A deuterium lamp has been used as a UV source light. The UV collimated beam (1 cm in diameter) is split by means of a semitransparent mirror in such a way to allow monitoring the lamp emission by measuring the current from a photodiode. Three narrow band filters (25 nm FWHM spread) selecting respectively 160nm, 185nm and 220nm, have been employed, due to the current unavailability of a monocromator. The UV beam is sent, through a rotatable mirror, to the photocathode. The photocurrent, generated by electrons extracted from the CsI film, is detected with a small (5x5cm2) wire chamber located at a distance of 2mm from the photocathode. The wires have a collection voltage of 133 V. A second wire plane, behind the first and oriented perpendicular to it, is kept at ground potential to obtain good charge collection on the first plane. After measuring the wire chamber photocurrent (A2), by rotating the mirror, the light is sent to a calibrated PMT, used in diode mode (A1). The currents (1 - 50nA range) are measured by a picoammeter (KEITHLEY 485). The ratio of the currents A2/A1, multiplied by the PMT QE, gives the absolute QE of the photocathode.

Three series of measurements on different photocathodes have been perfomed. The first one was performed on one of the photocathodes in Rome. The QE measurement results were 25.0+-1.4calibration of the reference PMT are not included

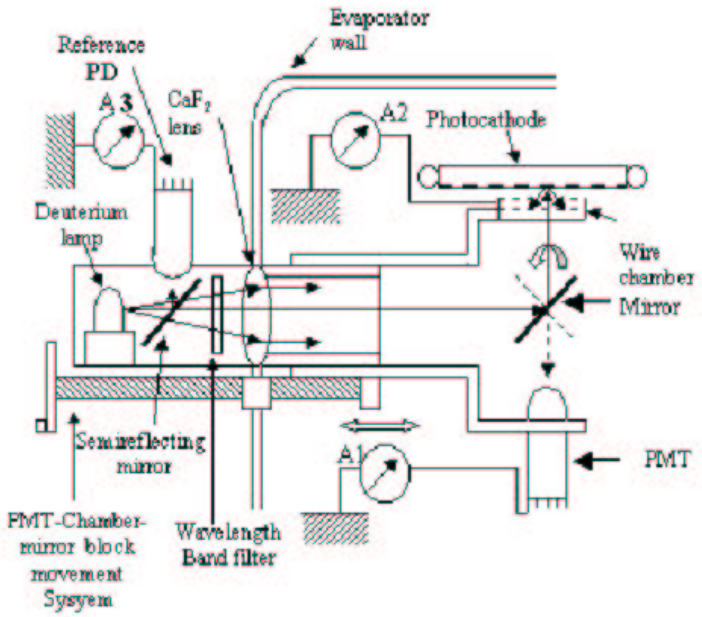

Figure 27: The Quantum Efficiency measurement system.

in the errors. Just after the evaporation the photocathode was transported to CERN for detector tests. Another photocathode was evaporated at CERN, in the HMPID facility. For these tests the wire chamber was operated at 1550 V with an Ar/CH4 (76/24) gas mixture. The results were quite good: the two photocathodes, exposed to a 7 GeV pion beam, showed the same results: 12.5 p.e., that can be easely estrapolated to 15 p.e. with CH4 at 2100 V. The evaporator was transported to JLab. Two other evaporation took place there on photocathodes. The results are consistent with the first evaporation and with the QE values extrapolated from the ALICE in-beam measurements (Fig. 28).

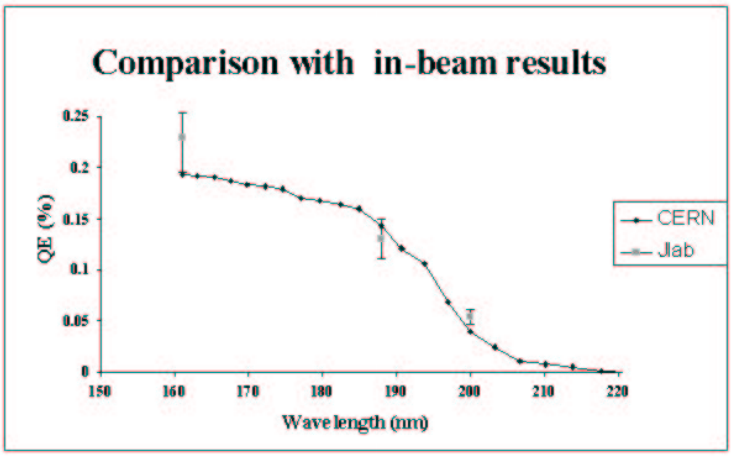

Figure 28: Average measured Quantum Efficiency as compared to the CERN extrapolation from in beam data.

Thickness Dependence

Measurements have been performed to test the QE as function of CsI thickness. We did a non uniform CsI deposition by asymmetric crucible charging (1.2g CsI weight on two crucibles, leaving the other two crucibles empty). According to calculation, a thickness variation along the surface from 50nm (for the part of the photocathode close to the empty crucibles) to 250nm (close to the charged crucibles) should be obtained. Fig. 29 shows the results of QE measurements. It is evident that passing from 50nm to 250nm of CsI the QE constantly increases. This is true for the whole UV spectrum. In addition, it can be noted that the thicker CsI film and longer wavelengths exhibit a stronger thickness dependence. It is not clear if the effect we show actually reflects the CsI thickness dependence. In fact the QE variation could depend on the different deposition speed.

Aging Test

Measurements have been performed to investigate the eventual degradation after contamination and possible recovery of CsI film. One of the photocathodes, just after measuring the QE, was left in the evaporator and the pumping was stopped. After 25 days the vacuum was 0.25 mbar. The pumping was restored reaching (after 2 h) 10-5 mbar. A new QE measurement was performed. After 14 more hours of pumping 10-6mbar was achieved. A second measurement has been performed in this condition. Finally, continuing pumping, a third measurement has been done after heating the film to 60(for 12 h. Results are shown in Fig. 30. Some contamination, probably from outgassing of the evaporator walls and from the photocathode itself, caused a substantial loss of QE (the photocathode was not baked after having it polished by alcohol before evaporation). The recovery of QE with improvement of vacuum condition is evident. Heating the photocathode for 12 h to 60(allowed the complete recovery of the QE, for all the three wavelengths. One conclusion might be that a possible contamination by organic outgassing can be completely recovered by heating the detector. Trying to understand the effect of oxygen and moisture contamination, another test has been done. The evaporator chamber has been slowly filled with 8 mbar of Ar and finally slowly filled with ambient air (19.5(temperature, 41% relative humidity). Then 24 h later the chamber was pumped out again. Another QE measurement was performed in this condition, with the same procedure described above (2 h, 16 h of pumping and further 12 h of heating).The results are shown in Fig.6. It is evident that contam-

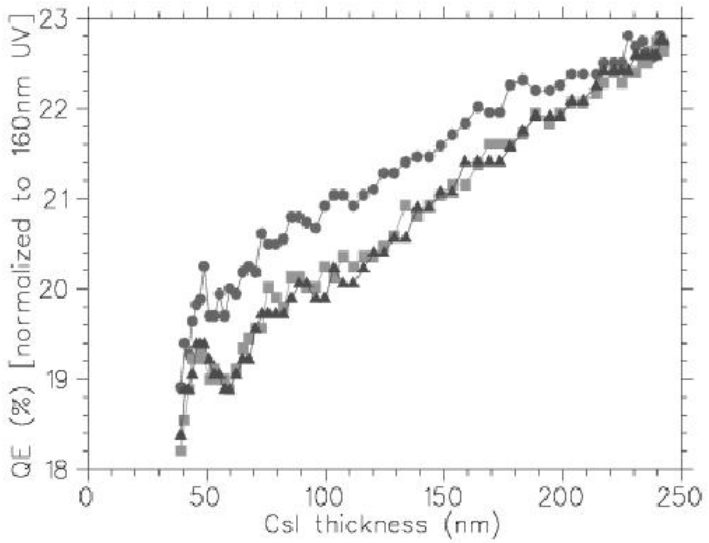

Figure 29: Quantum efficiency as function of CsI thickness. Different curves correspond to different wavelength.

ination by oxygen and moisture can not be completely recovered. It seems that the QE loss (between 50% and 60%) is more pronounced for thinner CsI layer and for longer wavelengths. It should be noted that for thickness above 120 nm at least 50extensive exposure to the ambient air. Subsequent pumping and heating improved the QE, but only restored 1/3 of the loss.

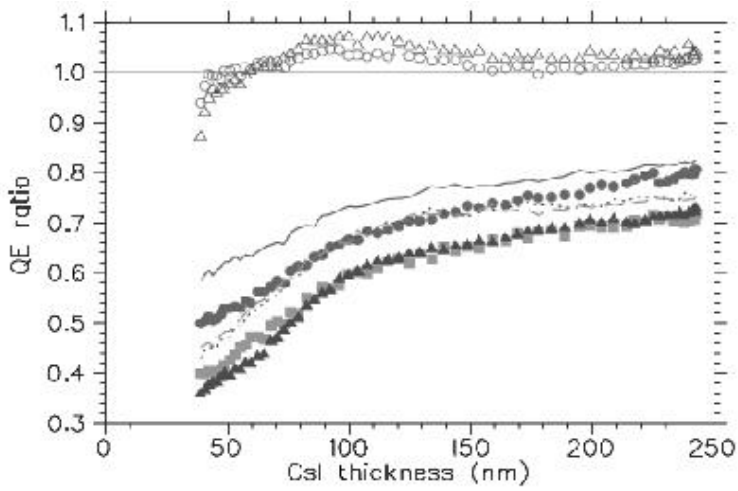

Figure 30: Quantum efficiency as function of thickness for different condition of contamination (see text). Different curves correspond to different wavelength.

In Beam Commissioning

During Jlab experiment E98-108 "Electroproduction of Kaons" the RICH detector was installed in the detector stack of the left HRS. Electron beams with energies of 3.4, 4.2 and 5.6 GeV were incident on 4 cm and 15 cm long liquid hydrogen targets. The standard HRS package was supplemented by two areogel detectors to improve the PID capabilities. The DAQ of the RICH could be operated in either of two different configurations. In the so-called ?stand-alone mode? it ran independently of the HRS DAQ system. In this mode, no tracking information from the HRS detectors was available for the analysis of the RICH data. In the second configuration, the RICH DAQ was integrated into the HRS DAQ system. Raw data from all detector systems were written to the same data files. Therefore full tracking and PID information from the HRS and the RICH were combined. The data without tracking information are not useful to get the right Cherenkov angle. Unfortunately, it was possible to take only a small part of the data in the integrated mode. Fig. 31 shows the data obtained using the small sample of data with tracking information: the cluster distribution for a single event in the RICH and cumulated events showing the proton and the pion rings. Kaons lie

in between. The number of kaons expected in the small statistical sample is too small to allow the extraction of the "kaon signal".

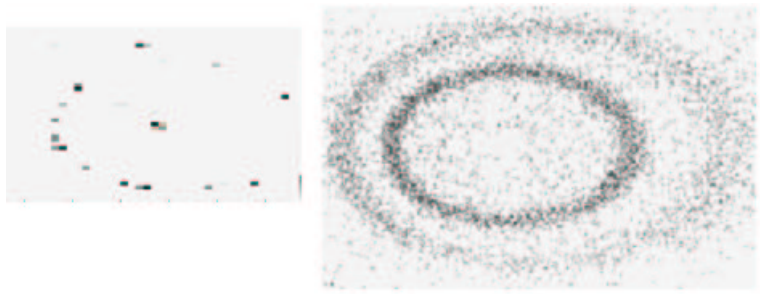

Figure 31: On beam tests: a) Typical event, b) Overlapping of pions and protons rings. Kaons are in between.

3.2 Detector Developments

3.2.1 BigBite Spectrometer

Contributed by D.W. Higinbotham

During the past year, three experiments which will use the BigBite spectrometer were approved by the Jefferson Lab program advisory committee. One is an experiment to determine the neutron electric form factor G_N^E at High Q^2 [41], one is an experiment to use the A_z and A_z asymmetries in quasi-elastic the polarized ^{3}He(e,e$'$d) reaction to better understand the ^{3}He ground state wave function [42], and one is an experiment to study deuteron electrodistintegration near threshold [43]. These are in addition to the already approved BigBite experiment to study the internal small-distance structure of nuclei via the triple coincidence (e,e'p+N) reaction [44] and the experiment to measure electroproduction of π^0 near threshold to test chiral QCD dynamics [45].

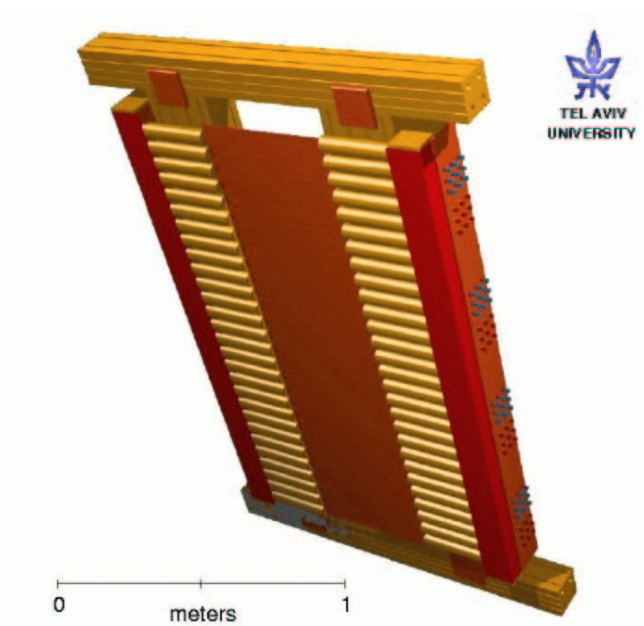

Figure 32: Shown above is the Jefferson Lab CAD drawing of the auxiliary plane. This detector, which was built by Tel Aviv University, has been built, tested, and is ready for operation.

Work on the construction of the BigBite spectrometer has progressed significantly. Shown in Fig. 32 is the auxiliary plane which was built for Hall A by Tel Aviv University. This plane, which will be used instead of a wire chamber for the triple coincidence experiment [44], consists of 56 scintillators bars, each of dimension 350 x25 x 2.5 mm^3. Shown in Fig. 33 is the trigger plane which was built for Hall A by the University of Glasgow. This plane is made up of 3 mm

and 30 mm scintillating layers to provide dE/E particle identification and will have timing resolution better than 0.5 ns. Peter Monaghan of the Massachusetts Institute of Technology along with the Jefferson Jab design group have designed and built a frame to hold the detectors together and in place near the BigBite dipole magnet. Olivier Gayou of the Massachusetts Institute of Technology has been working getting CODA to work with our new VME data acquisition system and also has been working on the new C++ analyzer for BigBite.

Figure 33: Shown above is the Jefferson Lab CAD drawing of the BigBite trigger plane. This detector, which was built by the University of Glasgow, has been built, tested, and is ready for operation.

The University of Virginia has obtained NSF funding to build the scattering chamber (needed for three experiments), special Hydrogen target (needed for one experiment), and wire chambers (needed for four experiments) for the BigBite spectrometer. Nilanga Liyanage is leading the project to build a prototype wire-chamber and Richard Lindgren is working on the completing the final design of the scattering chamber and the Hydrogen target.

In order to run the approved polarized Helium experiments with the BigBite spectrometer, Gordon Cates is leading a major effort to modify the ^{3}He polarized target. One of the nicest changes will be to use light guides to transport the laser

light to the Hall. This will mean that the temporary laser hut will no longer need to be built in the Hall. The University of Virginia is seeking NSF funding for this project.

Additional equipment which is being built in order to run the approved BigBite experiments include two different neutron detector arrays (one for the triple experiment and a much larger one for the G_N^E experiment) and a shower calorimeter which will be added to the BigBite detector package for the G_N^E experiment.

3.2.2 The DVCS/E00-110 Experimental Setup

Contributed by P. Bertin, A. Camsonne, C.E. Hyde-Wright, K. McCormick and F. Sabatié for the DVCS Hall A Collaboration

Introduction

The E00-110 experiment plans to study the *fully exclusive* $ep \to ep\gamma$ reaction in the deeply virtual regime (fixed x_B, large Q^2 and $Q^2 >> -t$, where t is the momentum transfer to the proton). Of particular interest, the beam spin asymetries allow one to measure linear combinations of Generalized Parton Distributions (GPD) through the interference of the Bethe-Heitler diagram where the photon is emitted by one of the electron lines, and the VCS diagram where the photon is emitted by the proton. The exclusivity is enforced by the detection of all 3 final state particles. We will use the left HRS for the detection of the scattered electron, a lead fluoride (PbF_2) calorimeter to detect the emitted photon and an annular scintillator array to detect recoil protons.

The Hall A floor is shown on Fig. 34 where one can see the location of the new detectors. To limit their size and to keep a large acceptance, the detectors will be located very close to the target: the front face of the scintillator will be at an average of 70 cm from the target and the front face of the calorimeter will be at 110 cm from it. Both the calorimeter and the proton array will be held by the same support frame. Note that a new spherical scattering chamber has to be built in order to allow rather low momentum (down to 400 MeV/c) protons to reach the proton array.

Saclay is responsible for the design of the DVCS detector, which is shown on Fig. 35 in its current state. The platform which will allow this detector to be moved at each new setting will be designed by Jefferson Lab. Since the detectors are so close to the target, the alignment should be rather precise to get a sufficient angular resolution. In addition, high rates are expected, and a novel data acquisition has been developed: the use of ARS (Analog Ring Sampler) which act as 1 GHz Flash-ADCs for all the channels of this experiment will allow us to handle pile-up events in a clean manner.

The following subsections will give details for each of the 3 major subsystems of the DVCS experiment in Hall A.

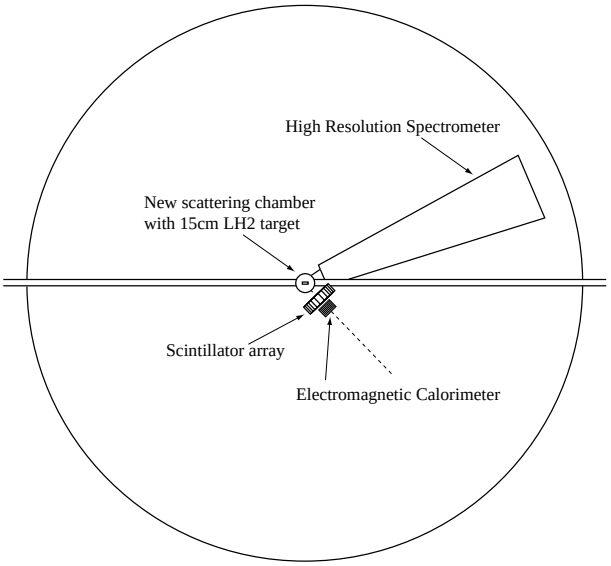

Figure 34: Hall A floor map, showing the location of the scintillator array and the calorimeter. The rightspectrometer (not shown) is parked at a large angle. The support frame for both detectors is not shown.

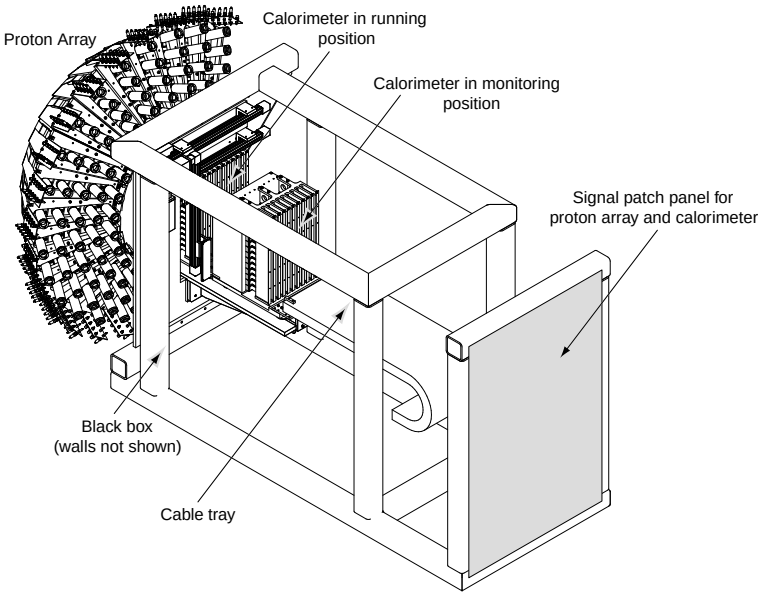

Figure 35: Full view of the DVCS arm in the current state of the design showing the proton array, the calorimeter and the black box protecting the calorimeter from the light (the walls are not shown).

Proton Array (ODU, LPC, Saclay, JLab)

In order to detect the recoil protons, we are constructing a 100 element plastic scintillator array. This array is matched to the out-of-plane acceptance required to measure the beam helicity asymmetry in deeply virtual kinematics. The array subtends polar angles 18 to 38 degrees in five rings around the central $\vec{q}$ direction. Each ring is divided into 20 elements that together subtend azimuthal angles from 45 to 315 degrees (the gap is required for the beam and scattered electron). For each $e\gamma$ coincidence, we can predict the direction of the outgoing proton, under the assumption of a $ep \to ep\gamma$ event. DVCS events will be separated from background according to the separation between the predicted direction of the proton and the direction of the coincident particle (if any) in the proton array. The angular resolution of the proton array is consistent with the convoluted resolutions of the electron spectrometer and photon calorimeter.

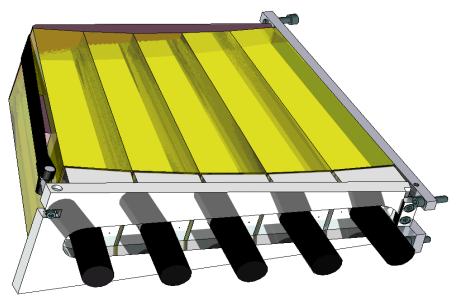

Figure 36: CAD drawing of 5-element "tower" from proton array. We tested a prototype tower in March 2002.

The proton array is constructed of EJ-200 scintillator coupled to Photonis XP2972 1 1/8" PMTs. Each PMT will be read out by one ARS channel. Mechanically, the array is constructed of 20 identical towers (Fig. 36), each spanning 13.5° degrees in azimuth and the polar angles 18–38°.

We tested a prototype tower during a dedicated DVCS test run in March 2002. Fig. 37 displays elastic calibration (peak-height) spectra for one of the blocks. We recorded the proton array waveforms in the ARS in coincidence with the $S0$ trigger in the electron arm, in elastic ep kinematics. The maximum signal we expect from DVCS protons is 200 MeVee (MeV electron equivalent).

During the March test run, we also measured the DC current, and/or PMT gain in the proton array tower elements as a function of luminosity and scattering angle of the proton element. We have a design criterion to maintain the anode DC current below 30 μA to guarantee acceptable PMT lifetime. In order to satisfy

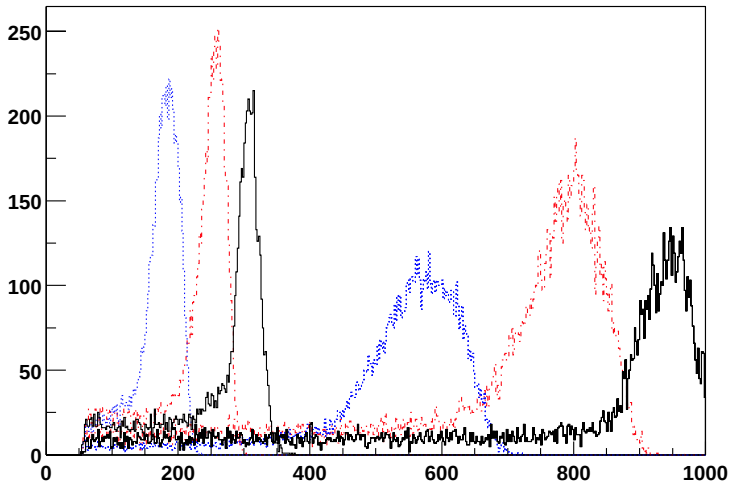

Figure 37: Elastic proton peak height spectra, recorded in one proton array scintillator in coincidence with the $S0$ electron trigger. The two groups of three peaks correspond to HV -762 and -862 V on a Photonis VD109 base and XP2972 PMT, together with an external $\times 8$ amplifier. In each group of three, the elastic proton recoil momenta are 560 (blue), 600 (red), and 640 MeV/c (black). After accounting for the 0.5" Al absorber and the Birks formula quenching in the scintillator, these correspond to deposited electron equivalent energies of 115, 135, and 160 MeV, respectively.

this limit, we will adjust the light collection, PMT gain, and external gain.

Using a reference PMT calibrated at LPC–Clermont-Ferrand, we calibrated the gain of the PMT in Fig. 37 to be $55 \cdot 10^3$ and $20 \cdot 10^3$ at 762 and 862 Volt, respectively. From cosmic ray studies of the prototype tower we measured the quantum yield of the scintillator PMT combination to be 15 photo-electrons per MeVee. To limit the DC anode current, we will reduce the yield to 5 photo-electrons/MeVee by placing an iris just in front of the PMT. Our design goal is to discriminate on 20 MeVee signals, or 100 photo-electrons. With this photo-electron yield, the singles measurements in March 2002 put a PMT gain limit of $3 \cdot 10^4$ for the proton elements farthest from the beam, at the design luminosity of $10^{37}/\mathrm{cm}^2/\mathrm{s}$. Based on the elastic calibration data of Fig. 37, in order to keep a 200 MeVee peak amplitude in channel 1000 of the ARS (dynamic range 0-1900), we require an external amplifier gain of 37. For the detectors closest to the beam line, we must reduce the PMT gain to $3 \cdot 10^3$–the digitized amplitudes will be accordingly reduced.

We have purchased all scintillator blocks and photo-multiplier tubes. The mechanical assembly for the 20 towers is under construction. We are designing a custom PMT base to provide an integrated amplifier with sufficient gain and bandwidth operating in the HV range 600–800 V. The base will also provide a low

bandwidth DC output to monitor the DC anode current.

Lead Fluoride Calorimeter (Rutgers, JLab, LPC, Saclay)

The calorimeter for the DVCS experiment will consist of 132 blocks of lead fluoride, each with dimension 30 mm × 30 mm × 184 mm. Lead fluoride is very dense ($\rho = 7.66$ g/cm^3), with a short radiation length ($X_0 = 0.95$ cm) and a small Moliere radius ($r_M = 2.22$ cm), which allows it to be built into a compact calorimeter. Each block will be viewed by a squarish fine-mesh Hamamatsu R7877 PMTs connected to an active base, providing the required gain and a DC anode current monitoring similarly to the proton array. Finally, each PMT will be read out by one ARS channel. A nine-cell prototype calorimeter was constructed and tested in Hall A during the March 2002 test run.

The calorimeter blocks for the test calorimeter were each viewed by a round, 28 mm diameter Photonis XP2972 PMT. The full DVCS calorimeter will be viewed by Hamamatsu R7700 U PMTS, which have the superior time resolution necessary to cope with the high rates of the DVCS experiment. A study of the wrapping and coupling of the PMTs to the blocks was performed in the EEL prior to construction of the test calorimeter. The study found that the light collection efficiency was maximized by wrapping the blocks in Tyvec paper, as compared to wrapping them in aluminized mylar and black paper. The PMTs for the test calorimeter were attached to the blocks using a UV curable glue, but because of the difficulty in changing out a non-working glued PMT, it was decided that the PMTs for the full DVCS array should be attached in some easily-removable way. This led to the development of a mechanical coupling scheme, similiar to that used in Hall B for the PRIMEX experiment. In this scheme, each lead fluoride block is fitted with a set of flanges on the front and rear, held tight around the block with two brass strips running the length of the block. The PMT fits snugly into the rear flange and is screwed into place. The Rutgers University shop is producing all of the flanges needed for the full DVCS calorimeter. The nine cell calorimeter was gain matched with a blue led before being installed in the Hall. This method of gain matching worked well, but was very time consuming, so for the full DVCS calorimeter array, an automated calibration scheme is being developed. In the automated calibration, an array of LEDs will be stepped around the face of the calorimeter with an X-Y scanner, produced and developed in cooperation between Saclay and the FESTO corporation.

During the DVCS test run, the nine-cell prototype calorimeter was installed in the focal plane of the left HRS, in the usual position of the gas Čerenkov detector (i.e. between S1 and S2). The LHRS angle and momentum was set to detect elastically scattered electrons at eight different kinematical settings ranging from 0.977 GeV to 3.980 GeV. To make sure that the elastically scattered electrons covered the calorimeter uniformly, Q3 was defocused by approximately 50%. Before extracting the energy resolution of the test calorimeter, the blocks were gain

matched again in software, by matching the edges of the ADC spectra for each block. The sum of the ADCs for the nine blocks was then cut on events which struck the center block (block 5) of the array and deposited more than 75% of their energy in the block. The resulting distribution was then fit with a Gaussian distribution to extract its mean and sigma. The resulting resolution as a function of energy is seen in Fig. 38. The curve shown in the figure is the result of a fit with the function $\sigma/E = a + b/\sqrt{E}$. The fit yields a resolution of $1.6\% \pm 3.6\%/\sqrt{E}$.

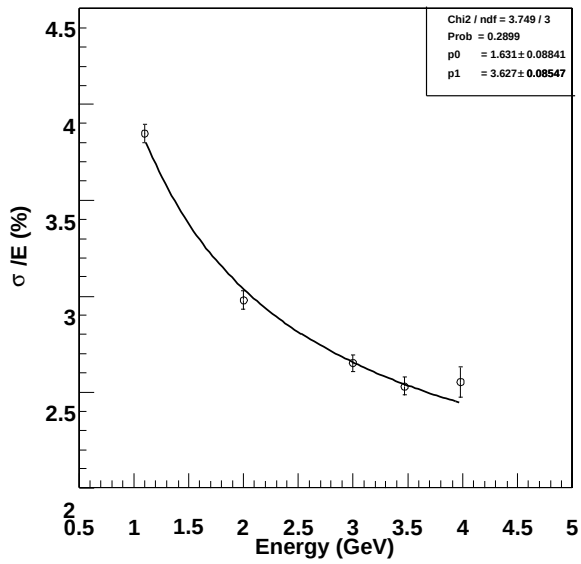

Figure 38: The resolution of the nine-cell PbF_2 test calorimeter as a function of energy. The data has been fit with the function $\sigma/E = a + b/\sqrt{E}$.

Data Acquisition System (LPC)

Unlike the dedicated DVCS detectors, the spectrometer's acquisition system consist of conventional ADCs and TDCs. Its primary role is to provide us with the first level trigger T1 when a good electron candidate is detected. However, the calorimeter and proton array information are recorded using a novel sytem: Analog Ring Samplers (ARS). These new devices based on a silicon chip developped by CEA/Saclay, have been studied, designed, and produced at the LPC. Each channel of the detectors are continuously sampled and stored on a 128-capacitor ring at a frequency of 1 GHz. The trigger signal T1 stops this process and freezes the information in the capacitors. A second level trigger T2 starts the extraction (1 MHz). Each of the 128 capacitors of the ring is digitized using a 12-bit ADC, yielding a 128 ns long waveform representing the signal during a predefined time window. Offline, these information are processed and used to extract the amplitudes and times of signals like conventional ADCs and TDCs. This is extremely

powerful to resolve pile-up events on which a careful waveform analysis can be performed to disentangle the signals arriving close in time, as shown on Fig. 39.

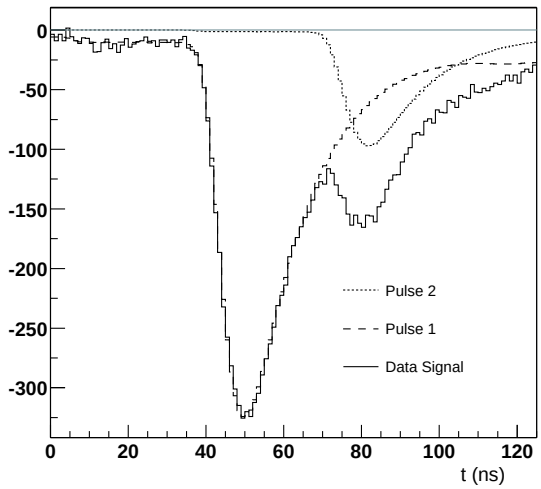

Figure 39: Typical waveform recorded by an ARS channel, yielding two pulses. A waveform analysis is performed to get the information about the two separate pulses.

Using ARS leads to an increase of the data rate roughly by a factor 64 compared to conventional electronics. It is therefore necessary to have a selective second level trigger, which is achieved by using the information of the electromagnetic calorimeter: the 132 channels are sent to a photon trigger module. If T1 is present, all 132 channels are first integrated, then digitized in parallel with 7-bit ADCs. For all combinations of 2×2 blocks on the calorimeter, the "sum-of-4" is calculated and compared to some predefined energy threshold (which can be rather high since DVCS photons are typically over 1.5 GeV for all kinematics). If at least one such combination passes the test, the second level trigger T2 is generated. However, if no high energy clusters are found, the system is cleared. All this process will only take 350 ns, keeping the dead time to a reasonable level if T1 is clean enough.

To this date, 360 ARS channels are available and ready to be shipped. The ARS decoding software is ready for the most part and has successfully been used for the analysis of the test run. The photon trigger module has been tested and will be fully equipped with integrating/digitizing modules before the end of 2002 and will be ready for a full-blown test at Jefferson Lab in February 2003.

3.2.3 Preparations for Hall A Parity-Violation Experiments

Contributed by K.D. Paschke

Polarized Source Development

The Hall A parity program uses parity-violating (PV) processes as a probe into the structure of nucleons and nuclei. The experiments in this program place very stringent demands on the polarized electron source in order to achieve the necessary statistical precision and systematic accuracy. The more demanding of the currently-scheduled experiments, E99-115 (HAPPEX-II), will measure PV scattering from Hydrogen at $Q^2 = 0.1$ GeV$^2/c^2$, with a final statistical precision of 60 parts per billion (ppb). Another PV experiment with conditional approval, PR-99-012 (Lead) is more demanding yet, with a goal of measuring the PV scattering asymmetry from Lead nuclei with a precision of 15 ppb in order to directly measure the extent of the neutron skin which is expected to exist in heavier nuclei.

These new Hall A PV experiments require high current ($\sim 100\mu$A) with high polarization. The presently available diode lasers are not able to provide sufficient power at a wavelength suitable for high electron polarization from the strained GaAs (840 nm), while the presently available Ti-Sapphire laser, built by the Polarized Source Group at Jefferson Lab, had exhibited excessive intensity jitter in previous usage. A commercial Ti-Sapphire laser has been purchased for G0 to meet similar requirements (high power at 840 nm with low 30 Hz intensity jitter). It has been shown in recent tests to produce the required power and exceed its intensity jitter specifications. A second laser has been ordered from the same vendor for the Hall A parity experiments, and the source group expects to take delivery in early 2003.

In order to limit systematic errors to negligible levels for these measurements, it is necessary to correct for systematic helicity-correlated (HC) differences in the beam. The largest corrections are for the charge asymmetry, which is a HC difference in integrated current between two helicity windows of a pair, and the HC position differences. With the highly-linear beam current monitors and phototubes of the integrating detectors, one expects to be able to correct for the charge asymmetry at the level of approximately 1%. Thus for HAPPEX-II, the charge asymmetry averaged over the entire data set must approach 2.0 parts per million (ppm), while for Lead, the requirement is 0.5 ppm. The correction due to position differences is less precise due to uncertainty in the coefficients relating position differences to measured asymmetry. Ideally, one would keep the size of the corrections at or below the size of the statistical uncertainty. The expected sensitivity to position on target is approximately 40 ppm/micron, leading to the requirement that for HAPPEX-II, the HC position difference on target should average to less than 1.5 nm.

The effort to control HC systematics at this level focuses on both designing and tuning the polarized source to minimize HC effects, and implementing feedback loops on the source which can be used to minimize real-time measurements of HC systematics. Collaboration members have been working closely with the source group on these efforts. Beam tests have been performed with measurements in

both Hall A and the injector to characterize performance of the source and the feedback mechanisms. We have also joined the effort on the Injector Test Stand (ITS) Laser table to study possible improvements in the source optics.

A corrector mechanism for charge asymmetry, the Intensity Attenuator (IA) system, has been developed. It consists of two aligned linear polarizers with a $\lambda/10$ plate and Pockels cell between them. Relatively small voltage changes (± 50 Volts) on the Pockels cell increase or decrease the intensity attenuation through this system at the few percent level. The real-time helicity signal is used to switch a power supply so that an adjustable voltage is applied during one helicity state and the Pockels cell is held at zero voltage for the complementary state. This system is placed upstream of most other optics, including the Circular Polarizing (CP) Pockels cell. The relatively low applied voltage reduces steering or ringing effects from the IA cell, so this system provides a clean method for reducing or increasing the input intensity for one helicity state relative to the other.

The IA system has been successfully used in an automated feedback loop to control charge asymmetry systematics. An example of the charge asymmetry during a run taken in June, 2002 and the running average of the charge asymmetry over that run is shown in Figure 40. These early tests indicate that the IA system is suitable for fine control of the charge asymmetry.

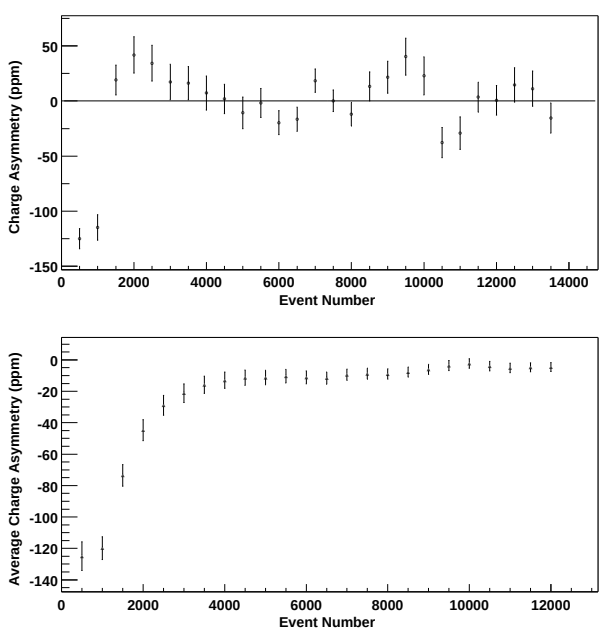

Figure 40: The control of the charge asymmetry and the convergence of the average charge asymmetry during a run from tests in June, 2002 demonstrate the effectiveness of feedback using the IA cell.

One drawback of the IA cell system is that the adjustment does not correct the fundamental cause of the charge asymmetry, which is predominantly a result of residual linear polarization in the laser incident on the strained GaAs photocathode. The voltage applied to the CP Pockels cell can be adjusted to reduce the fraction of linearly-polarized light, and thus control the charge asymmetry at the root of the problem. Such a correction should also help prevent unmeasured, higher-order effects such as spot size or shape asymmetries from becoming significant. For the sake of tradition, feedback using the CP Pockels cell high voltage is usually called "PITA" feedback, as it was the feedback system used during the original HAPPEX to control the Polarization Induced Transport Asymmetry (a cause of charge asymmetry). Development is continuing on a system which uses the IA cell on a time scale of a few minutes to minimize charge asymmetry, and uses the PITA feedback on a time scale of 8 hours to minimize the average IA cell setting, thus keeping all source systematics small while controlling charge asymmetry.

Development is also continuing for the control of the HC position differences. Studies in the ITS laser room will be done to investigate various approaches to minimizing the position differences before feedback. The use of a piezo-electric actuated mirror (PZT) as a corrector mechanism is also being studied. In several beam tests over the past year, the stability of the calibration constants and the dynamic range of the PZT system have been shown to be suitable. However, the system has also shown some undesirable characteristics, most notably a correlation between position and charge systematics of approximately 0.25ppm/nm.

In addition to controlling the charge asymmetry and position difference averages, it is necessary to control other systematics that may increase noise or otherwise complicate analysis. One such effect is seen in Figure 41, which shows the charge asymmetry as a function of time in the helicity window broken out by the time-ordering of the helicity states and the helicity of the window before the pair. The asymmetric pairs (for example, R followed by the pair RL) show a strong time dependence. This is consistent with a slow settle time in the CP Pockels cell voltage. Direct measurement indicates that the Pockels cell voltage is approximately 20 Volts different at the beginning of the integration period than at the end ($\sim 0.6\%$ variation from the nominal voltage), which would fully explain the behavior of the R(RL) and L(LR) curves at early times. A new high-voltage switch that should reduce these effects is currently being tested. However, there is an additional unexplained effect in the significant difference between the "symmetric" pairs R(LR) and L(RL). In these pairs, each helicity window is preceded by its complement, so any effect of a slow high-voltage transition should effect these measurements in precisely the same way. The cause of the observed difference is not presently understood.

During recent G0 tests, a significant (~ 300 ppm) charge asymmetry has been observed when the CP Pockels cell, and all HC feedback devices, were turned off. Without the CP Pockels cell, there should have been no helicity information in the

beam, so this result was considered very surprising. It was recently discovered by the G0 collaboration that eliminating in-time helicity signals sent over electronic cables to various DAQs in the injector (the G0 and Hall A parity injector DAQs and the Mott DAQ) eliminated this charge asymmetry. The mechanism by which the charge asymmetry was induced has not been explained. As a result of this discovery, there is a renewed commitment to limit the real-time helicity information to only the feedback systems and the CP Pockels cell at the source while a parity experiment is running.

Data Acquisition and Analysis

HAPPEX anticipates a pulse pair width of 500 ppm, and we wish to have non-statistical sources of noise be a negligible contribution. Assuming a reasonable dynamic range of approximately 30,000 ADC channels, one would like to have pedestal noise at or below 5 channels. This is comparable with the least-noisy pedestals seen during the original HAPPEX, so pedestal noise was a potential problem for HAPPEX-II. This noise is dominated by pick-up in the long cable runs between the spectrometer huts and the counting house DAQ. To avoid these long cable runs, an improved DAQ is being developed, which utilizes a crate in each spectrometer electronics hut to readout the detector phototubes as well as the crate in the counting house for readout of the beam monitors. Testing on the new DAQ elements is nearly complete.

2 MHz Voltage-to-Frequency (V2F) converters have been added to the parity DAQ to allow additional channels for signals that do not require the higher resolution provided by the HAPPEX integrating ADCs.

New versions of the old HAPPEX ADC timing board have been created. This

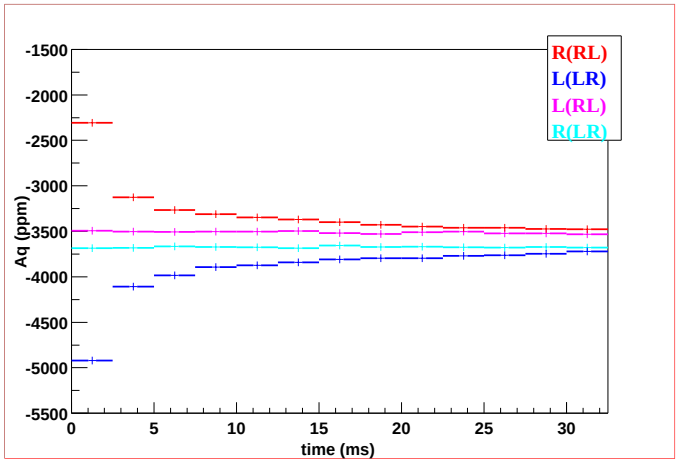

Figure 41: Time dependence of the charge asymmetry across the 33 ms helicity-flipping window.

board is used to gate the HAPPEX integrating ADCs and provide other DAQ control signals, based on an internal clock but triggered externally at the start of each helicity window. The new versions are largely functional copies of the old versions, with a few addition signal outputs useful for gating and latching scalers for the V2F readout. The new boards replace the old wire-wrap boards, which were becoming unreliable.

A new parity analysis package (PAN) has been developed, primarily written in C++ and making extensive use of the ROOT libraries. PAN was designed to serve as both a real-time on-line analysis tool, capable of providing online monitoring and controlling feedback systems, and an off-line analysis package. The online PAN functionality is nearing completion, while the off-line analysis functions are still under development. PAN incorporates a MySQL database of information for each run to track configuration changes and calibration parameters.

Detector and Beam Monitors

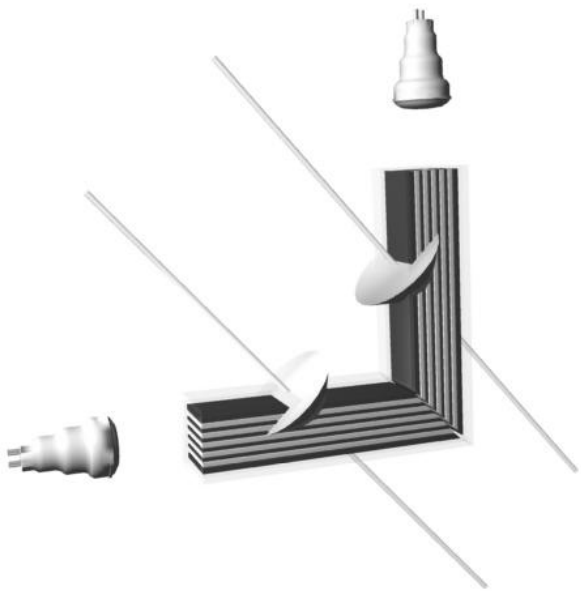

Figure 42: The two-segment HAPPEX detector.

The integrating electron calorimeters have been built for the upcoming PV experiments. These detectors collect Čerenkov light from the elastic scattered electrons, and the absence of scintillation makes them insensitive to soft pions and photons. They are composed of alternating layers of fused quartz and brass so they are suitably radiation-hard, and they are specified to measure the energy of incident electrons with a resolution below 20%. A possible false asymmetry systematic due to trace ferromagnetic components of the brass alloy has been

calculated to be negligible. The detectors are composed of two segments which will be aligned in the spectrometer focal plane to divide the Q^2 distribution. Each segment is instrumented with a single phototube. The combined detector will contain the distribution of elastically-scattered electrons while remaining separate from the inelastic distribution in the focal plane. The two segments connect to form an "L" shape, oriented so that the segments align with an edge of the Čerenkov cone for maximal light collection, as shown in Figure 42. One segment was installed in the Møller polarimeter in Hall A for in-beam tests. These tests verified that the energy resolution was below 20%, and that edge effects were suitably understood.

In order to provide both higher resolution and higher redundancy in the measurement of charge and position, cavity beam monitors similar to those used in Hall B have been developed for both G0 and the Hall A PV experiments. A set of the G0 monitors was installed on the Hall A beam line for a test during Summer, 2002. The test demonstrated that the monitors worked as expected. The instrumentation of the monitors, based on that used by Hall B, provided a logarithmic amplification for the position and charge readout. This has been shown to be unsuitable for the parity experiments, as the logarithmic readout introduces significant systematic error in the averaging over 30 Hz windows as well as a significant degradation in the resolution of the monitors. New readout electronics for these cavities are currently being developed based on an I/Q mixer, which obviates the need for an offset in the position measurements. Two sets of cavities (each reading out charge and x and y positions) will be installed between the H04A and H04B stripline BPMs, and a third set will be installed in the BSY region.

3.3 Software Developments

3.3.1 Software for High Voltage Control

Contributed by E. Chudakov

A new software package for HV control has been written, using Java programming language. This package was used in experiment E99-114 (RCS) in order to control about 1000 HV channels of the calorimeter and the veto counter. The package included a graphical user interface, a mapping for the detector channels to the set of HV crates and modules, a network communication package, programs to issue particular commands to HV crates and an alarm system. Networking can be done using two interfaces of LeCroy 1458 mainframes: the Ethernet interface and the serial interface. The Ethernet interface was used for RCS experiment because of its higher speed. All changes of the voltage settings were stored in a database. The GUI allowed to see the status of all the HV channels on the computer screen and check or change them, while it was also possible to load the settings from external files or from the database. An alarm was issued when the voltage or current values became different from the set ones. The HV mainframes were located close to the calorimeter, in a relatively high radiation environment, which caused them to trip often - at least once a day on average, therefore an automated alarm system and a constant control of the values were essential for the experiment.

Elements of this system were also used to perform slow control of other equipment at RCS. Work is in progress aiming to adapt the package to use ARCNET - another network protocol, commonly used with LeCroy 1458.

3.4 Look Into Future

3.4.1 Medium Acceptance Device

Contributed by J.J. LeRose

General characteristics

Central Momentum		6 GeV/c	
Configuration	35°	20°	12°
$\Delta P/P_0$		$\pm$ 15%	
y_0		$\geq \pm$ 6 cm	
θ_0	$\pm$ 198 mrad	$\pm$ 138 mrad	$\pm$ 68 mrad
ϕ_0	$\pm$ 35 mrad	$\pm$ 32 mrad	$\pm$ 23 mrad
$\Delta\Omega$	$\sim$ 28 msr	$\sim$ 18 msr	$\sim$ 6 msr
δy_0	2.6 mm	3.6 mm	4.6 mm
$\delta\theta_0$	1.9 mrad	1.3 mrad	0.6 mrad
$\delta\phi_0$	0.5 mrad	0.5 mrad	0.5 mrad
$\delta\sigma$	1.3E-3	1.0E-3	0.7E-3

Table 6: The table shows the estimated performance parameters based on Transport calculations of the optical properties. For y_0, as much as $\pm$ 20 cm makes it through the spectrometer, but the ϕ_0 centroid shifts. The error estimates assume a 0.5 mrad angle determination and 100 μm position determination.

The purpose of the Medium Acceptance Device, known as MAD, is to, among other things, provide a tool for high-x studies of the properties of nucleons with 11 GeV beam. Large acceptance in both solid angle and momentum with moderate momentum resolution are needed for the planned experiments.

The device is a magnetic spectrometer built from two combined function, quadrupole and dipole, superconducting magnets. The quadrupole components provide the focussing necessary to achieve the desired solid angle while the dipole components provide the dispersion needed for momentum resolution. The maximum central momentum is 6 GeV/c. The total bend angle is 35° with 10° bend in the first magnet and 25° bend in the second. The larger bend in the second magnet was chosen to prevent direct line of sight between the target and the detectors while keeping the dispersion reasonably small thereby reducing the size requirements on the detector package. Extra versatility can be achieved by varying the drift distance to the first magnet: larger drift distances allow smaller scattering angles at the cost of reduced acceptance. Depending on the details of the detector

package, scattering angles as small as 12° are possible.

The main new development in 2002 is the increase in the bend angle of the second magnet and the subsequent increase in the overall bend angle. This change was necessitated by the observation in GEANT simulations [46] that background rates in the detector resulting from direct line of sight to the target were unacceptable. Removing the direct line of sight reduced this rate by a factor of about five. The impact on magnet design and optical properties is minimal. There has also been some progress made on defining the way events can be interpreted optically.

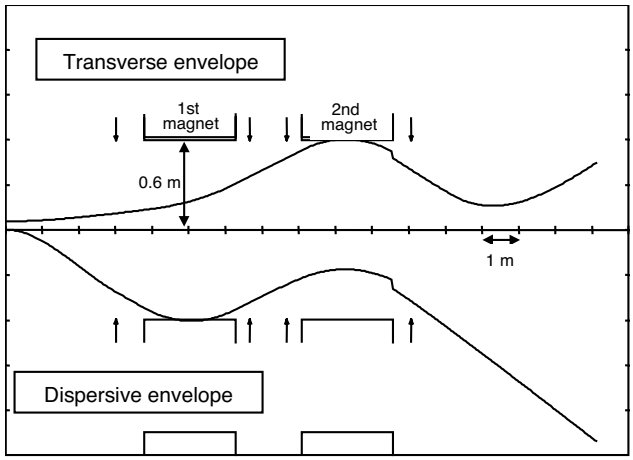

Figure 43: Transverse and dispersive envelopes.

Transport studies

The beam envelope, transverse and dispersive, calculated with 2nd order TRANSPORT for the 35° configuration is shown on Fig. 43. The optics is very much that of a quadrupole pair. The large acceptance is achieved by keeping the magnets as short as possible and as close together as possible. The first order transfer matrices for the 35° and 20° configurations are shown in Tab. 7 and Tab. 8. In both cases $< x|\theta\delta > \sim 17$, which drives the expected momentum resolution at $\delta\pm$ 15/12° configuration is shown in Tab. 9. In this case, $< x|\delta\theta > \sim 25$

	x	θ	y	ϕ	δ
x	-3.72	0.00	0.00	0.00	3.54
θ	-1.03	-0.27	0.00	0.00	103.0
y	0.00	0.00	1.00	5.15	0.00
ϕ	0.00	0.00	-1.05	-4.43	0.00

Table 7: The first order Transport matrix in natural units (m, rd) for the 35° configuration.

	x	θ	y	ϕ	δ
x	-2.51	0.00	0.00	0.00	3.29
θ	-0.70	-0.40	0.00	0.00	90.2
y	0.00	0.00	1.00	7.10	0.00
ϕ	0.00	0.00	-0.79	-4.58	0.00

Table 8: The first order matrix for the 20° configuration.

	x	θ	y	ϕ	δ
x	-2.51	0.00	0.00	0.00	3.29
θ	-0.70	-0.40	0.00	0.00	90.2
y	0.00	0.00	1.00	7.10	0.00
ϕ	0.00	0.00	-0.79	-4.58	0.00

Table 9: The first order matrix for the 12° configuration.

Raytracing studies

A working model of the MAD has been developed using the raytracing code SNAKE. The magnetic fields in the magnets are determined using TOSCA generated maps. Those maps were created by running TOSCA on the magnet with only the quadrupole coil energized and with only the dipole element energized. Two maps are thereby generated. Those two maps are then added together with scale factors to simulate tuning the various elements. Once the first order properties expected from the Transport studies are achieved a large number (2000) of random trajectories spanning the full acceptance of the spectrometer are traced through the spectrometer. These trajectories are then used as input to a fitting program (MUDIFI) that determines the best-fit polynomials reconstructing the target parameters ((δ, θ_0, y_0, and ϕ_0) of the trajectories based on their positions and angles (x_f, y_f, θ_f, and ϕ_f) in the detectors. The sensitivity to measurement errors in the detectors can then be explored in a Monte-Carlo fashion using a new set of trajectories generated in the same manner as those used in the fitting. These forward and reverse functions are available to anyone wishing to simulate their own experiment [47].

The discussion on the above website describes the difficulty encountered when trying to fit limited order polynomials to trajectories in a device with such large acceptance and speculates that that problem can be circumvented by subdividing the acceptance into smaller subsections. At this time that option has been explored with some success. Simply subdividing the momentum acceptance into 3 large bins gives very encouraging results. Using nothing more than 5th order polynomials the quality of the achieved fit is shown in Tab. 10 (note that the presented σ's represent the quality of the fitted polynomial NOT the expected resolution).

	-15% $< \delta <$ -5%	-5% $< \delta <$ +5%	+5% $< \delta <$ +15%
σ_δ	2.2×10^{-4}	4.2×10^{-4}	6.6×10^{-4}
σ_θ	1.6×10^{-4}	3.5×10^{-4}	4.5×10^{-4}
σ_ϕ	7.5×10^{-4}	1.2×10^{-3}	1.3×10^{-3}
σ_y	3.4×10^{-3}	5.3×10^{-3}	5.9×10^{-3}

Table 10: Expected resolutions: both δ and θ are reconstructed well better than the anticipated resolution; y and ϕ still require some work.

Outlook

The basic concept is well along and awaiting further engineering development. Much remains to be done in terms of a detailed engineering design which will doubtless have some feedback on the design characteristics of the finally achieved device.

Summaries of Experimental Activities

4 Summaries of Experimental Activities

4.1 Experiment E89-028

Polarization Transfer Measurements in the ^{2}H$(\vec{e}, e'\vec{p})$n Reaction

J.M. Finn, M.K. Jones and P.E. Ulmer, cospokespersons
for
the Hall A Collaboration.

This experiment tests the validity of deuteron models by providing data on the recoil polarization observables in ^{2}H$(\vec{e}, e'\vec{p})$n. In addition to enhancing our understanding of the deuteron structure and reaction mechanisms in $(e, e'p)$, the information gained here will be critical in interpreting the G_{En} experiment using the analogous ^{2}H$(\vec{e}, e'\vec{n})$p reaction [48]. This latter experiment will determine the ratio of the neutron form factors, G_{En}/G_{Mn}, assuming that nuclear effects in the deuteron are under control. The G_{En} measurement cannot test the model assumptions whereas experiment E89-028 can, by comparing measurements on hydrogen and deuterium targets.

E89-028 measured the recoil polarization observables of the ^{1}H$(\vec{e}, e'\vec{p})$ reaction and the ^{2}H$(\vec{e}, e'\vec{p})$n reaction in quasifree kinematics (*i.e.* $x_{Bj} = 1$) centered at zero recoil momentum ($p_m = 0$) at Q^2 values of 0.43, 1.0 and 1.6 (GeV/c)^2, near those of the Madey experiment. In addition, to test the model assumptions at more extreme kinematics, also sampled in the Madey experiment, we measured the ^{2}H$(\vec{e}, e'\vec{p})$n reaction at $p_m = 160$ MeV/c for $Q^2 = 1.0$ (GeV/c)^2 and $x_{Bj} = 1$. In Fig. 44 preliminary results for the double ratio, consisting of the ratio P'_x/P'_z for ^{2}H$(\vec{e}, e'\vec{p})$n divided by the same ratio for ^{1}H$(\vec{e}, e'\vec{p})$, are shown for the three measurements centered at $p_m = 0$. Only statistical error bars are shown in the figure; the systematic uncertainties are negligible compared to the statistical uncertainties. The ^{2}H$(\vec{e}, e'\vec{p})$n and ^{1}H$(\vec{e}, e'\vec{p})$ data were taken at exactly the same spectrometer settings, so that systematic errors would be minimized when measuring the ratio of polarization variables. Further, the beam polarization and FPP analyzing power cancel for this quantity. It can be seen that the present data represent a substantial improvement over the earlier MIT-Bates data [49].

The calculations shown are from Arenhövel [50]. The plane wave Born approximation (PWBA) calculation includes scattering from the neutron with detection of the spectator proton. (As our kinematics involve relatively high momentum transfers and are centered on $p_m = 0$, the PWBA calculation is nearly identical to the PWIA calculation which only includes scattering from the proton.) The distorted wave Born approximation (DWBA) includes pn final state rescattering (FSI). The DWBA+MEC+IC calculation includes also non-nucleonic currents (MEC and IC) and the full calculation (DWBA+MEC+IC+RC) further includes relativistic contributions of leading order in p/m to the kinematic wave function boost and to the nucleon current. The Bonn [51] two-body interaction and dipole nucleon form

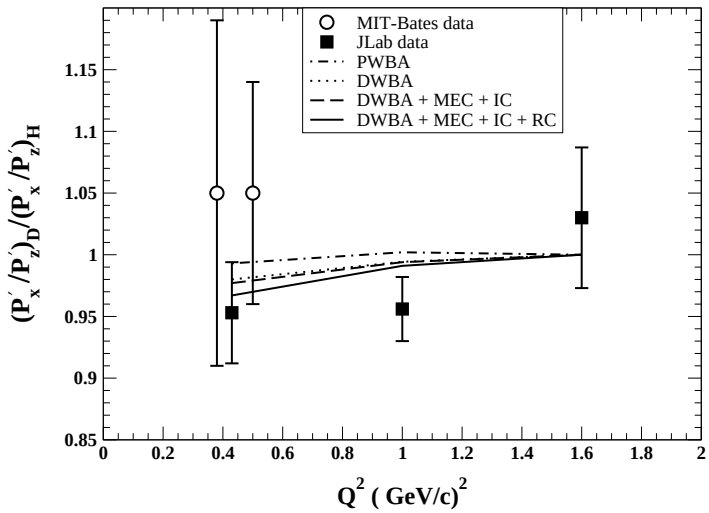

Figure 44: The double ratio, $(P'_x/P'_z)_D/(P'_x/P'_z)_H$, consisting of the ratio of transverse to longitudinal polarization for ^{2}H$(\vec{e}, e'\vec{p})$n divided by the same ratio for ^{1}H$(\vec{e}, e'\vec{p})$. The dot-dashed curve is for PWBA, the dotted curve is for DWBA, the dashed curve includes MEC and IC and the solid curve is the full calculation which also includes relativistic corrections (RC). The open circles are for the MIT-Bates data [49] and the filled squares are preliminary results from the present experiment.

factors were used. The models were acceptance averaged using MCEEP [25] via interpolation over a kinematic grid. Radiative folding was carried out within the framework of Borie and Drechsel [52]. The PWBA model gives nearly unity as can be expected; small differences from unity arise from acceptance averaging effects which are different for a bound, moving proton and a free, stationary proton. It can be seen that the full calculation agrees well with the data and, further that nuclear effects are quite small for these kinematics and decrease with Q^2. Therefore, one might expect that the neutron form factor extraction using the analogous ^{2}H$(\vec{e}, e'\vec{n})$p reaction would be trustworthy and especially so at higher Q^2.

In Fig. 45 the preliminary datum at $p_m = 160$ MeV/c and $Q^2 = 1.00$ (GeV/c)^2 is shown. Again, only the statistical uncertainty is plotted in the figure; the systematic uncertainty is negligible compared to the statistical uncertainty. In order to partially cancel various systematic errors, the polarization ratio at this kinematics is divided by the ratio at $p_m = 0$ and $Q^2 = 1.00$ (GeV/c)^2. Non-nucleonic currents have little effect whereas FSI and especially relativity have substantial effects. The datum deviates from the full calculation by $\sim 1.8\sigma$. Though the neutron form factor experiment samples values of p_m of order 160 MeV/c, the cross section weighting implies a relatively small contribution from such high values. In addition, the Madey experiment is centered on $p_m = 0$ and therefore samples protons on both sides of the momentum transfer direction, $\vec{q}$. Calculations from Arenhövel indicate that relativistic effects are of roughly equal magnitude and opposite sign for protons detected symmetrically about $\vec{q}$, so that the neutron

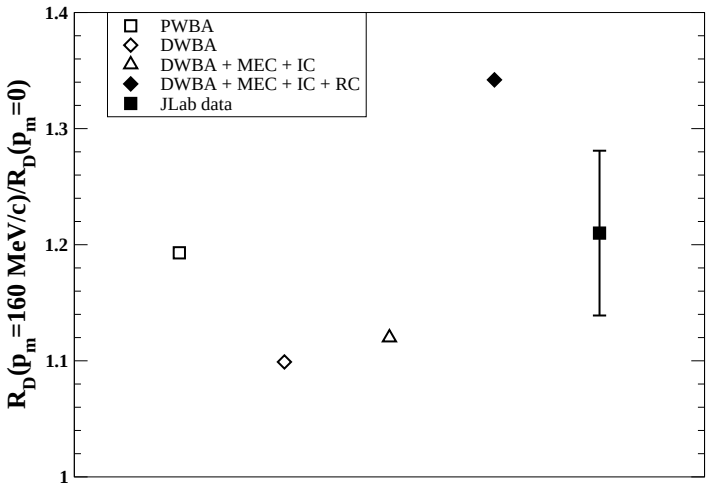

Figure 45: Preliminary results for the ratio of $(P'_x/P'_z)_D$ at $Q^2 = 1.0$ (GeV/c)^2 and $p_m = 160$ MeV/c to $(P'_x/P'_z)_D$ at $Q^2 = 1.0$ (GeV/c)^2 and $p_m = 0$ MeV/c. The p_m value of 160 MeV/c corresponds to the cross section weighted average whereas the central value was 174 MeV/c. The theoretical points shown here have been acceptance averaged and radiatively folded.

experiment is largely insensitive to these effects. It should be cautioned, however, that nuclear effects are likely to have a greater impact on the neutron electric form factor extraction due to its relatively small size compared with the proton electric form factor.

In conclusion, the polarization double ratio agrees reasonably well with the reaction model for the deuteron, indicating that the extraction of neutron form factors from the analogous ^{2}H$(\vec{e}, e'\vec{n})$p reaction is likely to be trustworthy. A draft manuscript for submission to Physical Review Letters was recently distributed to the experiment and Hall A collaborations for review.

4.2 Experiment E89-044

Selected Studies of the ^{3}He Nucleus through Electrondisintegration at High Momemtum Transfer

M. Epstein, A. Saha, and E. Voutier, Spokespersons,
and
the Hall A Collaboration

The aim of this experiment, is to investigate three specific aspects of the electromagnetic respone of ^{3}He through (e,e'p) coincidence measurements. In part I, which was described in last year's report, we are studying the single nucleon structure of ^3He at $|\vec{q}| = 1.5$ GeV/c in perpendicular kinematics at missing momenta (p_{miss}) up to 1 GeV/c. To this end we are doing a complete in-plane separation of the response functions, R_L, R_T and R_{L+TT} up to $p_{miss} = 0.55$ GeV/c. In part II, we probe the $|\vec{q}|$ dependence of the reaction by taking data in parallel kinematics to extract the R_L and R_T response functions. Data were taken for $p_{miss} = 0$ GeV/c up to $|\vec{q}| = 3$ GeV/c and for $|\vec{q}| = 1$ and 2 GeV/c at $p_{miss} = \pm\ 0.3$ GeV/c. In part III, we focus on the continuum region (large E_{miss}) to study correlated nucleon pairs. In this region, data were taken in perpendicular kinematics and allow a response function separation for selected large (E_{miss}, p_{miss}) regions. The data taking phase of E89-044 was completed in March, 2000.

The data of Part I comprise the Ph.D. thesis of Marat Rvachev of MIT and this work is almost completed. The data of part II are the basis for the Ph.D. thesis of Emilie Penel-Nottaris of ISN Grenoble and the data of part III will be incorporated in the Ph.D. thesis of Fatiha Benmokhtar of Rutgers University. Parts II and III are discussed in the following sections.

Parallel Kinematics Data

The parallel kinematics used for LT-separation of the cross-sections are presented in Table 11.

P_{miss} (MeV/c)	Q^2 (GeV^2)	q (GeV/c)	$\epsilon_{forward} - \epsilon_{backward}$
0	0.80	1.00	0.966 − 0.247
0	1.54	1.50	0.943 − 0.200
0	2.27	1.94	0.899 − 0.314
0	4.10	3.00	0.719 − 0.180
+300	0.94	1.00	0.968 − 0.338
-300	0.52	1.01	0.924 − 0.523
-300	1.45	1.94	0.891 − 0.204

Table 11: Parallel kinematics measured in the experiment.

Preliminary results are presented for forward kinematics at $p_{miss} = 0$ MeV/c (Figure 46). The absolute cross-section normalization does not take into account elastic scattering measurements, that were taken to determine target density, which could change these results by about 10%. These are compared to a plane wave model: K $\sigma_{cc1} \cdot S(P_{miss})$ with the De Forest σ_{cc1} prescription and the spectral function from G. Salme.

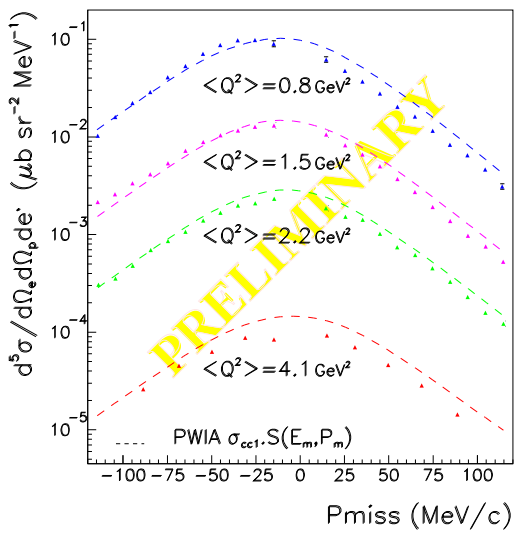

Figure 46: ^{3}He(e,e′p)d cross-sections for $p_{miss} = 0$ MeV/c.

Preliminary calculations by Jean-Marc Laget, not shown here, suggest that except around $Q^2 = 0.8$ GeV^2, final state interactions and meson exchange currents are not very important in this kinematic region. We anticipate complete data analysis and theoretical calculations later next year.

Continuum Data

Preliminary results have been extracted in the continuum region for the fixed momentum transfer, $|\vec{q}| = 1.5$ GeV/c, energy transfer ω around 0.83 GeV, missing energies up to 180 MeV, and missing momenta around 425 MeV/c and 575 MeV/c. Cross sections have been extracted for E_{miss} bins of 10 MeV and p_{miss} bins of 10 MeV/c. Fig. 4.2 shows a sample E_{miss} spectrum at $p_{miss} = 425$ MeV/c. Note the relatively large yield in the continuum for these kinematics. Fig. 4.2 shows the radiatively corrected cross section in the total phase space covered by this kinematics, and for two different p_{miss} regions. These results were obtained by using the simulation code MCEEP [25] to obtain a fit to the data including radiative tails, and then using the same code to extract the unradiated cross-sections. These

preliminary results are compared to plane wave impulse approximation (PWIA) calculations similar to those described above. One can see a systematic deviation from the spectator nucleon model which is currently investigated, as well as the onset of the pion production channel at large E_{miss}.

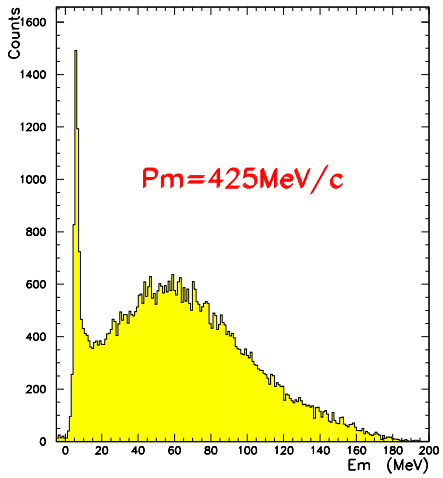

Figure 47: Missing energy spectrum.

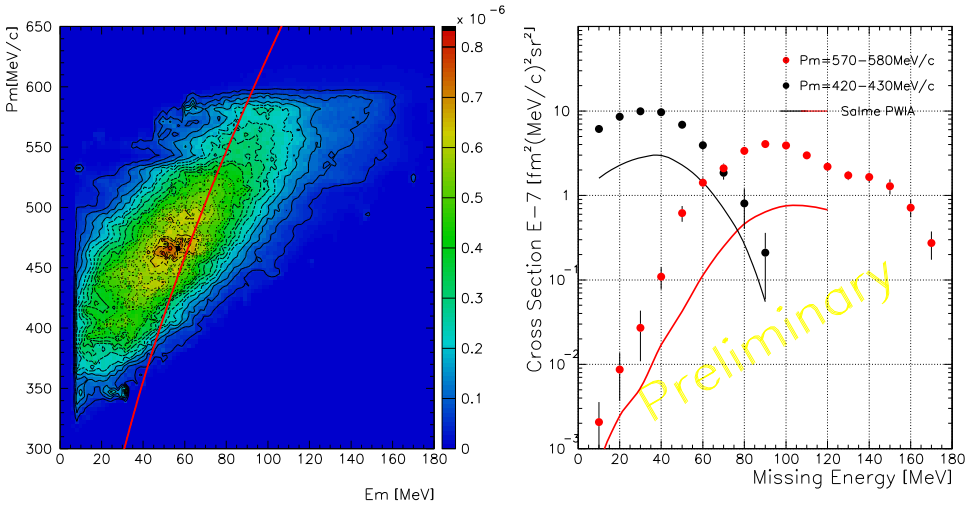

Figure 48: Continuum cross section data in the global (E_{miss}, p_{miss}) phase space of the considered kinematics (left) and for selected momentum transfer region as compared to a PWIA calculation; the red curve on the left panel indicate the correlation bewteen E_{miss} and p_{miss} if the interaction occurs on a quasi-deuteron inside the nucleus.

4.3 Experiment E91-011

Investigation of the N $\rightarrow \Delta$ Transition via Polarization Observables in Hall A

S. Frullani, J.J. Kelly, and A.J. Sarty, Spokespersons,
and
the Hall A Collaboration.

Recoil polarization observables can provide new insight into properties of nucleon resonances and the reaction mechanisms for electroproduction of mesons by providing access to interference between small amplitudes and dominant amplitudes. The dominant amplitude for pion electroproduction at the Δ resonance is the M_{1+} multipole, but there is much current interest in the smaller S_{1+} amplitude that arises from configuration mixing within the quark core [53], often described as quadrupole deformation, or from meson and gluon exchange currents between quarks [54], or coupling to the pion cloud outside the quark core [55,56]. Observables which depend upon real parts of interference products are sensitive to these quadrupole amplitudes, but reliable interpretation of such data requires understanding background contributions from nonresonant production mechanisms and from underlying nondominant resonances. Sensitivity to background amplitudes is provided by observables which depend upon the imaginary parts of similar interference products. Experiment 91-011 was designed to measure both types of observables for the $p(\vec{e}, e'\vec{p})\pi^0$ reaction using the focal-plane polarimeter.

Our implementation of the R-function method for the cross section analysis was discussed in the progress report for 2001. Cross sections were extracted for a $5 \times 2 \times 20 \times 12$ grid in (W, Q^2, x_{cm}, ϕ) where W is the invariant mass of the πN system, Q^2 is the photon virtuality, $x_{cm} = \cos(\theta_\pi)$ is obtained from the pion angle in the cm, and ϕ is the azimuthal angle. Results for $W = 1.22 \pm 0.02$ GeV and $Q^2 = 0.9 \pm 0.1$ (GeV/c)^2 are compared in Fig. 49 with several recent models [57–59] and with a multipole analysis described below.

Polarization observables and the corresponding response functions were extracted using the maximum likelihood method. The likelihood function for the response function analysis takes the form

$$L = \prod_{i=1}^{N} \frac{1}{2\pi}(1 + \epsilon_x \sin\phi_{fpp} + \epsilon_y \cos\phi_{fpp}) \tag{1}$$

where

$$\epsilon_\alpha = \xi_\alpha + A(\theta_{fpp}) \sum_\beta S_{\alpha\beta}(P_\beta + hP'_\beta) \tag{2}$$

is the azimuthal asymmetry for a polarization $\vec{\Pi} = \vec{P} + h\vec{P}'$ with helicity-independent and helicity-dependent contributions, $\vec{P}$ and $\vec{P}'$, in the πN cm system at the target transformed to the focal-plane coordinate system by the spin-transport

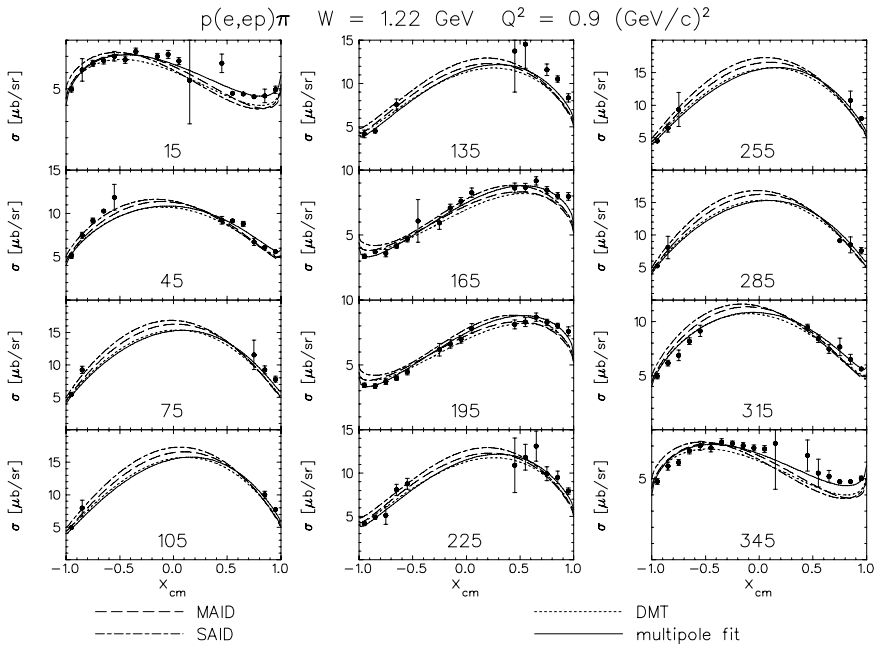

Figure 49: Preliminary cross section data are compared with recent models and a multipole fit. The panels are labeled by ϕ.

matrix $S_{\alpha\beta}$. The FPP analyzing power and false asymmetry are $A(\theta_{fpp})$ and ξ_α. The polarizations are then expanded in response functions, R_η, according to

$$\sigma P_\beta = \sum_\eta \nu_{\beta\eta}(\epsilon, \phi) R_\eta \tag{3}$$

where σ is the differential cross section and where the kinematic coefficients, $\nu_{\beta\eta}$, depend upon the transverse polarization of the virtual photon, ϵ, and the azimuthal angle, ϕ. Thus, for a fixed model of the differential cross section the logarithm of the likelihood function is linear in the polarized response functions with coefficients that are accumulated event by event. The data were binned with respect to (W, Q^2, x_{cm}); the bins for (W, Q^2) match the cross section analysis but the nonuniform spacing in x_{cm} is designed to better utilize the lower statistics of the polarization data. Acceptance-averaged response functions were then obtained by maximizing the likelihood with respect to the response functions and their uncertainties were obtained from the covariance matrix.

Polarized response functions for a representative bin, $W = 1.22 \pm 0.02$ GeV and $Q^2 = 0.9 \pm 0.1$ (GeV/c)^2, are shown in Fig. 50 where the first set contributes in plane while the second set is obtained from the out-of-plane acceptance. The labeling distinguishes L, T, LT, and TT contributions to the unpolarized (0) cross section and to sideways (S), normal (N), or longitudinal (L) components of recoil polarization with an h to indicate helicity dependence, if any. Linear combinations

that cannot be resolved without Rosenbluth separation are identified by L+T. These data are compared with the MAID2000, SAID, and DMT models. There is relatively little variation among models for those response functions that are dominated by multipole amplitudes for the Δ resonance but there are much larger variations for those, such as R_{LT}^N or R_{LT}^S, with significant background contributions from nonresonant mechanisms or nondominant (higher) resonances. The DMT model seems to provide the best overall fit to these data while the SAID model has the most difficulty with R_{LT}^N or R_{LT}^S, but none of these models provides a uniformly good fit to all response functions.

We have begun studying the sensitivity of the data to variations of the multipole amplitudes, but the results are still preliminary. The basic idea is to represent a multipole amplitude, $A_i(W, Q^2)$, in the form

$$A_i(W, Q^2) = A_i^{(0)}(W, Q^2) + \delta A_i(W, Q^2) \tag{4}$$

where $A^{(0)}$ is obtained from a suitable baseline model, here taken to be MAID2000, and δA is an adjustable parameter to be fitted to the data. The analysis fits all cross section and polarization response-function data that are available in a (W, Q^2) bin simultaneously. Adjustments to the magnetic, electric, and scalar amplitudes for a subset of the contributing partial waves are fit while maintaining the remaining amplitudes at their input (baseline) values. Examples of this procedure are shown in Fig. 51. The E_{0+} and S_{0+} amplitudes are highly correlated in the fit, so we somewhat arbitrarily chose to vary the real parts and not the imaginary parts; nor did we vary amplitudes for $\ell \geq 2$ at this stage. Although the wisdom of these selections will require further investigation, it is clear that the fit to data can be improved with relatively modest variations of the multipole amplitudes.

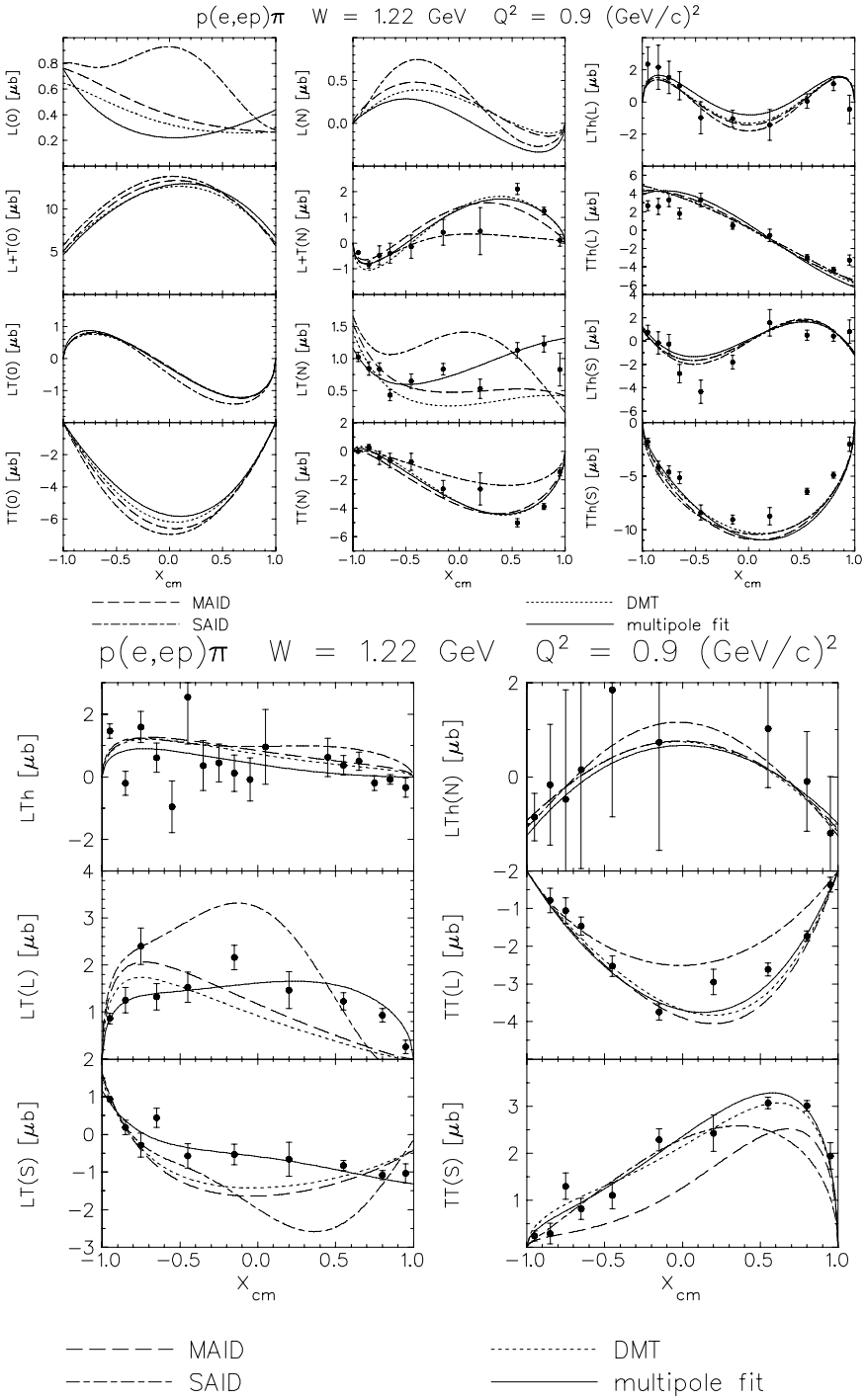

Figure 50: Preliminary data for response functions are compared with recent models and a multipole fit. The top set contribute within the scattering plane while the bottom set requires out-of-plane acceptance. The unpolarized cross sections were included in the multipole fit also but were not decomposed into response functions for this purpose.

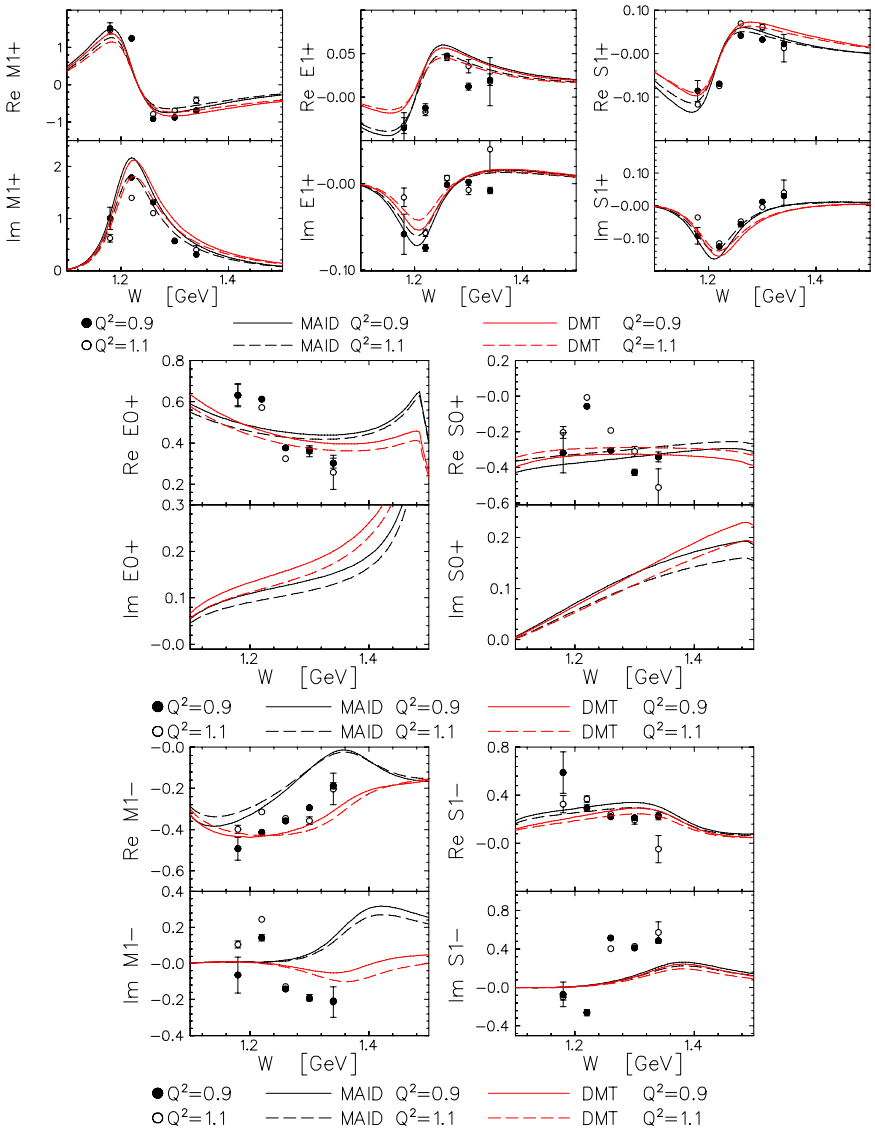

Figure 51: Preliminary 1+ multipole fits. Fitted amplitudes for $Q^2 = 0.9$ or $Q^2 = 1.1$ (GeV/c)^2 are shown as filled or open circles, respectively. Baseline (MAID2000) amplitudes for these sets are shown as solid or dashed curves. The corresponding amplitudes for the DMT model are shown in red.

4.4 Experiment E93-049

Polarization Transfer Measurements in the Reaction ^{4}He$(\vec{e}, e'\vec{p})^3$H in the Quasielastic Scattering Region

R. Ent and P.E. Ulmer, cospokespersons
for
the E93-049 Collaboration.

Polarization transfer in quasielastic nucleon knockout is sensitive to the properties of the nucleon in the nuclear medium including possible modification of the nucleon form factor and/or spinor. Experiment E93-049 measured the polarization transfer coefficients over the range of Q^2 from 0.5 to 2.6 (GeV/c)^2 and as a function of missing momentum in the range 0 to 240 MeV/c in order to determine the electric to magnetic form factor ratio for protons bound in the ^{4}He nucleus. ^{4}He was selected for study since its relative simplicity allows for realistic microscopic calculations and since its high density enhances any possible medium effects. Also, a variety of calculations indicate polarization observables for the ^{4}He$(\vec{e}, e'\vec{p})^3$H reaction have minimal influence from final state interactions (FSI) and meson exchange currents (MEC). It is precisely these effects (especially FSI) that have so far prevented a clean determination of nucleon medium modifications from unpolarized response functions in $(e, e'p)$ experiments. As the experiment was designed to detect differences between the in-medium polarizations and the free values, both ^{4}He and ^{1}H targets were employed (except at $Q^2 = 2.6$ (GeV/c)^2, where only ^{4}He data were acquired due to beam time constraints).

The quark-meson coupling (QMC) model of Lu *et al.* [60] suggests a measurable deviation of the ratio of the proton's electric (G_E) and magnetic (G_M) form factors from its free space value over the Q^2 range accessible by experiment. This calculation is consistent with present constraints on possible medium modifications for both G_E (from the Coulomb Sum Rule, with $Q^2 < 0.5$ (GeV/c)^2 [61–63]), G_M (from a y-scaling analysis [64], for $Q^2 > 1$ (GeV/c)^2), and limits on the scaling of nucleon magnetic moments in nuclei [65]. Similar effects have been calculated in the light-front constituent quark model of Frank *et al.* [66].

Our results are shown in Fig. 52 as R/R_{PWIA} for all four values of Q^2. Here, R is defined as

$$R = \frac{(P'_x/P'_z)_{^4\mathrm{He}}}{(P'_x/P'_z)_{^1\mathrm{H}}}. \tag{5}$$

for the data, whereas R_{PWIA} is the same ratio based on the relativistic plane-wave impulse approximation (RPWIA) calculation. The helium polarization ratio is normalized to the hydrogen polarization ratio measured at the same setting, since this double ratio is almost completely insensitive to all systematic uncertainties. As a cross check, the hydrogen results were also used to extract the free proton form factor ratio G_E/G_M and found to be in excellent agreement with previous

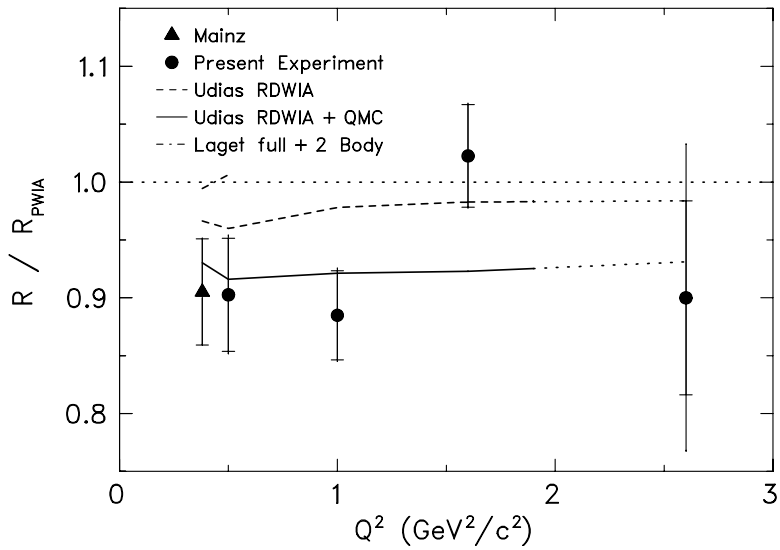

Figure 52: Superratio R/R_{PWIA} as a function of Q^2 for this experiment and for the Mainz experiment [69]. R is defined as the double ratio $(P'_x/P'_z)_{He}/(P'_x/P'_z)_H$. In PWIA (short-dashed curve) this superratio is identically unity, barring acceptance-averaging effects. The dashed curve shows the results of the full relativistic calculation of Udias *et al.* [70]. The dot-dashed curve shows the results of Laget's full calculation, including two-body currents [71]. The solid curve indicates the full relativistic calculation of Udias including medium modifications as predicted by a quark-meson coupling model [60]. For $Q^2 > 1.8$ (GeV/c)^2 the Udias calculations maintain a constant relativistic optical potential and are indicated as short-dashed curves. Lines connect the acceptance-averaged theory calculations and are to guide the eye only.

data [67,68]. In addition, our result at $Q^2 = 0.5$ (GeV/c)^2 closely coincides with the recent results at $Q^2 = 0.4$ (GeV/c)^2 of Mainz [69], also shown in Fig. 52.

The theoretical calculations by the Madrid group [70] and Laget [71] have been averaged over the experimental acceptance. At $Q^2 = 0.5$ and 1.0 (GeV/c)^2 the RPWIA calculation overestimates the data by $\approx 10\%$. The relativistic distorted-wave impulse approximation (RDWIA) calculation gives a slightly smaller ($\approx 3\%$) value of R but still overpredicts the data. After including the (density-dependent) medium-modified form factors as predicted by Lu *et al.* [60] in the RDWIA calculation, excellent agreement is obtained at both settings. In general, various choices for, *e.g.*, spinor distortions, current operators, and relativistic corrections, affect the theoretical predictions by $\leq 3\%$, and can presently not explain the disagreement between the data and the RDWIA calculations. In contrast, the datum at $Q^2 = 1.6$ (GeV/c)^2 is well described by the RPWIA and RDWIA calculations, whereas all calculations are consistent with the datum at $Q^2 = 2.6$ (GeV/c)^2.

The induced polarization, P_y, which is identically zero in the absence of FSI effects (in the one-photon exchange approximation) tests our assertion that FSI effects are, in fact, small. By averaging over the two beam helicities we have extracted P_y and it is seen to be both small and in agreement with the RDWIA

calculations.

In summary, we have measured recoil polarization in the ^{4}He$(\vec{e}, e'\vec{p})^3$H reaction in the range from $Q^2 = 0.5$ to 2.6 (GeV/c)^2. Within our model assumptions we find strong evidence for a medium modification; a calculation incorporating a predicted medium modification based on the quark-meson coupling model [60] gives a good description of our data. Moreover, the calculated induced polarizations agree well with our data, giving credibility to the validity of the treatment of FSI effects in the model. These data provide the most stringent test to date of the applicability of conventional meson-nucleon calculations. A draft manuscript for submission to Physical Review Letters has recently been distributed to the E93-049 Collaboration for review.

4.5 Experiment E93-050

Virtual Compton Scattering

C.E. Hyde-Wright
for
the Hall A VCS Collaboration

The $\mathrm{H}(e,e'p)\gamma$ reaction is a coherent superposition of radiation from the incident or scattered electron in elastic ep scattering (Bethe-Heitler–BH) and exclusive production of a photon on the proton, by absorption of a virtual photon (Virtual Compton Scattering–VCS). Experimentally, we separate the exclusive photon final state from π^0 electroproduction and other channels by reconstructing the missing mass of the unobserved particle(s) [72]. The kinematics of the VCS reaction are characterized by the invariant momentum transfer squared from the electron: $Q^2 = -q^2 = -(k-k')^2$, the invariant mass of the photon-proton system: $s = W^2 = (q+P)^2$, and the polar and azimuthal angles $\theta_{\gamma\gamma}$ and $\phi_{\gamma\gamma}$ of the outgoing photon relative to the direction $\vec{q}$ of the momentum transfered from the electron.

The virtual Compton amplitude includes a coherent sum of all possible intermediate states. In the low energy limit ($s \to M_p^2$, for arbitrary Q^2) the low energy theorems describe the VCS amplitude as a sum of the Born term (proton bremsstrahlung) plus a set of generalized polarizabilities.[73] The Q^2 variation of the generalized polarizabilities measures the spatial variation of the electric and magnetic polarization induced in the proton by external electric and magnetic fields. The VCS cross section can be expanded in powers of q' (the final CM photon energy) as follows:

$$\begin{aligned} d^5\sigma &= d^5\sigma^{BH+B} \\ &+ \frac{(2\pi)^5}{64M}\frac{k'_{\mathrm{lab}}}{k_{\mathrm{lab}}}\frac{q'}{\sqrt{s}}\left[v_{LL}\left(P_{LL}(Q^2) - P_{TT}(Q^2)/\epsilon\right) + v_{LT}P_{LT}(Q^2)\right] + \mathcal{O}(q'^2) \end{aligned} \tag{6}$$

In this expansion: v_{LL} and v_{LT} are kinematic factors; $d^5\sigma^{BH+B}$ is the cross section resulting from the coherent superposition of the Bethe-Heitler and Born amplitudes; and the structure functions P_Λ result from the interference of the Bethe-Heitler + Born amplitude with the leading order non-Born term in the VCS amplitude. The P_Λ are directly linked to the Q^2 dependent electric and magnetic polarizabilities α_E and β_M, respectively, as follows:

$$P_{LL} - P_{TT}/\epsilon = \frac{4M_p}{\alpha_{\mathrm{QED}}}G_E^p(Q^2)\alpha_E(Q^2) + \text{ Spin Polarizabilities} \tag{7}$$

$$P_{LT} = -\frac{2M_p}{\alpha_{\mathrm{QED}}}\sqrt{\frac{\mathbf{q}_{\mathrm{CM}}^2}{Q^2}}G_E^p(Q^2)\beta_M(Q^2) + \text{ Spin Polarizabilities} \tag{8}$$

In E93050, we took data below pion threshold ($M_p^2 < s < (M_p + m_\pi)^2$) at $Q^2 = 1.0$ and 1.9 GeV^2. In these measurements, a single electron arm setting spanned the entire region below threshold, and we moved the proton arm to span a large range in $\theta_{\gamma\gamma}$. At $Q^2 = 1$, we also measured a resonance excitation scan for nine central values of s from 1.3 GeV^2 to 3.6 GeV^2, with the coincidence angular kinematics centered on $\theta_{\gamma\gamma} = \pi$.

Below pion threshold, we extract the differential cross section by comparing the integrated yield in a bin with a simulated cross section including the Bethe-Heitler and Born terms[74] and the radiative tail (second photon emission) of the complete VCS process.[75] From the experimental cross sections, we use the expansion of Eq. 6 to extract the polarizability combinations $P_{LL} - P_{TT}/\epsilon$ and P_{LT}. We use these initial estimates of the Polarizabilities in the simulation cross section to iterate the analysis. In the polarizability analysis, it is convenient to define the following quantity:

$$\Delta\mathcal{M} \quad = \quad \left[d^5\sigma - d^5\sigma^{BH+B}\right] \frac{64M}{(2\pi)^5} \frac{k_{\rm lab}}{k - {\rm lab}'} \frac{\sqrt{s}}{q'} \tag{9}$$

In the low energy limit, $\Delta\mathcal{M}$ reduces to the polarizability structure functions:

$$\lim_{q' \to 0} \Delta\mathcal{M} \quad \longrightarrow \quad \Delta\mathcal{M}^{\rm LET} = \left[v_{LL}\left(P_{LL}(Q^2) - P_{TT}(Q^2)/\epsilon\right) + v_{LT} P_{LT}(Q^2)\right] \tag{10}$$

Fig. 53 illustrates the extraction of the structure functions $P_{LL} - P_{TT}/\epsilon$ and P_{LT} from our VCS data below pion threshold.

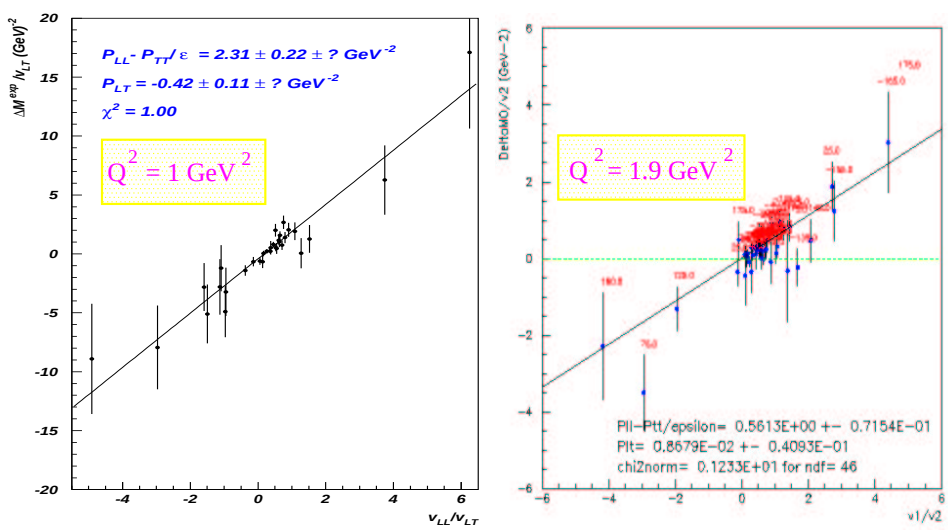

Figure 53: Low Energy Theorem extraction of structure functions $P_{LL} - P_{TT}/\epsilon$ and P_{LT} at $Q^2 = 1$ and 1.9 GeV^2. The two plots present $\Delta\mathcal{M}/v_{LT}$ as a function of the ratio v_{LT}/v_{TT}. (see Eq. 6–10). The extracted slope is P_{LT} and the intercept is $P_{LL} - P_{TT}/\epsilon$.

B. Pasquini *et al.* [76] developed a dispersion relation (DR) formalism for the analysis of Virtual Compton Scattering up to the Δ-resonance. In this formalism, the VCS scattering amplitude is predicted from the MAID[57] parameterization of pion electroproduction, π^0 exchange in the t-channel, and two low energy parameters $\Delta\alpha(Q^2)$ and $\Delta\beta(Q^2)$, which are the phenomenological contributions to these two polarizabilities, not otherwize constrained by the dispersion integrals over the pion electroproduction data.

Both below and above pion threshold, the DR formalism provides a rigorous description of the higher order terms beyond the polarizabilities in the VCS amplitude. We have included the DR formalism in our analysis of the VCS data at $Q^2 = 1.0$ GeV^2 from threshold through the Δ resonance. The analysis is consistent with the LET analysis of the data below pion threshold. Fig. 54 displays our preliminary results on the polarizabilities. The Dispersion Relations predict the values of all of the spin polarizabilities. In displaying our data, we use the Dispersion Relations to remove the spin contribution P_{TT}/ϵ. The data show that α_E follows the shape of $G_E(Q^2)$. For β_M, the data require a very large diamagnetic part at all Q^2.

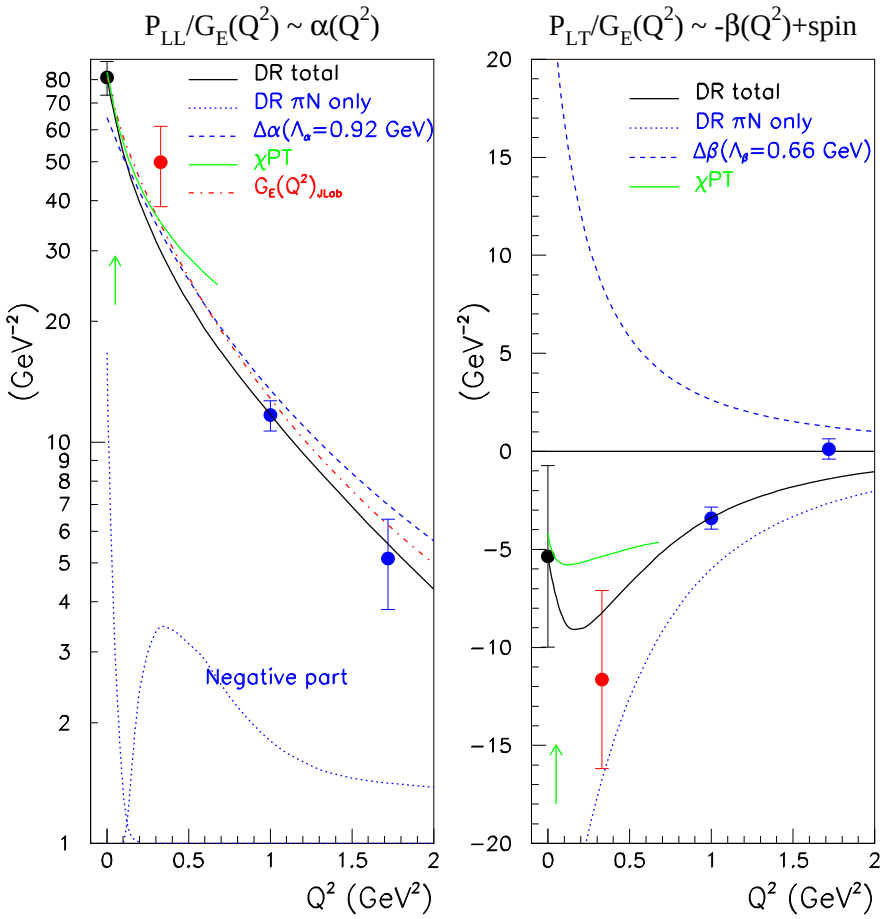

Figure 54: Q^2-dependent polarizabilities, including preliminary results from Jefferson Lab E93050 (blue points), Mainz VCS results from J. Roche *et al.* [78] (red point), world average of RCS results [77] (black point), and kinematics of Bates experiment (green arrow) [79]. The solid blue curves are the prediction of the Dispersion Relations, including just πN intermediate states. The contributions to α_E and β_M beyond πN intermediate states are parameterized by two dipole functions $\Delta\alpha_E(0)/[1+Q^2/\Lambda_\alpha^2]^2$ and $\Delta\beta_M(0)/[1+Q^2/\Lambda_\beta^2]^2$ (dashed blue curves). These are fit to the $Q^2 = 0$ GeV^2 and 1 GeV^2 points. The black lines are the full DR calculations. The DR curves show that the πN states, including the Δ, strongly overpredict the magnetic polarizability. A strong diamagnetic contribution is required from the sum over all other (higher energy) channels. The red curve is the proton electric form factor, normalized to the the $Q^2 = 0$ point. The green curve is the Chiral Perturbation Theory result [80].

4.6 Experiment E94-010

Measurement of the Neutron (^{3}He) Spin Structure Function at Low Q^2

S. Choi
for
G. Cates, J.-P. Chen and Z.-E. Meziani, Spokespersons,
and
the E94-010 Collaboration.

Data were taken in inclusive scattering of polarized electrons off a polarized ^{3}He target at six beam energies (0.86, 1.72, 2.58,3.34,4.24 and 5.06 GeV). The kinematics of this experiment covers the energy excitation range from the quasi-elastic peak to the beginning of the deep inelastic regime and a Q^2 range from 0.1 GeV^2 to 1.0 GeV^2. This is a measurement of spin dependent cross sections where the electron beam helicity was parallel or antiparallel to its momentum and the target spin parallel or perpendicular to the electron beam momentum. A first analysis was carried where the virtual photoabsorption cross section $\sigma_{TT}^{^3He}$ was extracted and the Q^2 dependence of the extended neutron GDH integral evaluated. A second analysis focused on determining the stucture functions $g_1^{^3He}(x, Q^2)$ and $g_2^{^3He}(x, Q^2)$ of ^{3}He and evaluating moments of the neutron structure functions.

The higher moments are especially dominated by the contribution from the resonance region covered in this measurement. The higher moments can also be calculated using the convergence of OPE expansion and lattice QCD at Q^2 as low as 1 GeV^2.

The data analysis is complete with a 5% systematic error on the absolute cross sections from an extended gas target. The original objective of studying the extended GDH sum has been achieved by the first publication [81].

In addition to the study of the extended GDH sum, we have evaluated various moments of the extracted structure functions in the small Q^2 region: $\Gamma_1(Q^2) = \int g_1(x, Q^2)dx$, $\Gamma_2(Q^2) = \int g_2(x, Q^2)dx$. Our results for Γ_1 on the neutron is used to study the evolution of the Bjorken sum at low Q^2 region when combined with Hall-B data on the proton. Γ_2 is known as the Burkhardt-Cottingham (BC) integral [95]. This integral is equal to zero in the high Q^2 regime (deep inelastic regime) and is Q^2 independent. We do not know how low in momentum transfer this sum rule should hold. Our preliminary result indicates a possible violation of the BC sum rule as Q^2 decreases below $Q^2 = 1$ GeV^2. The data are well described by the MAID calculation[82].

Another interesting integral is the d_2 matrix element defined as

$$d_2(Q^2) = \int_0^1 [2g_1(x, Q^2) + 3g_2(x, Q^2)]\, dx.$$

In the high Q^2 regime, using OPE, the d_2 matrix element can be shown to be a measure of the higher twist effect on the $g_2(x, Q^2)$ structure function. At small

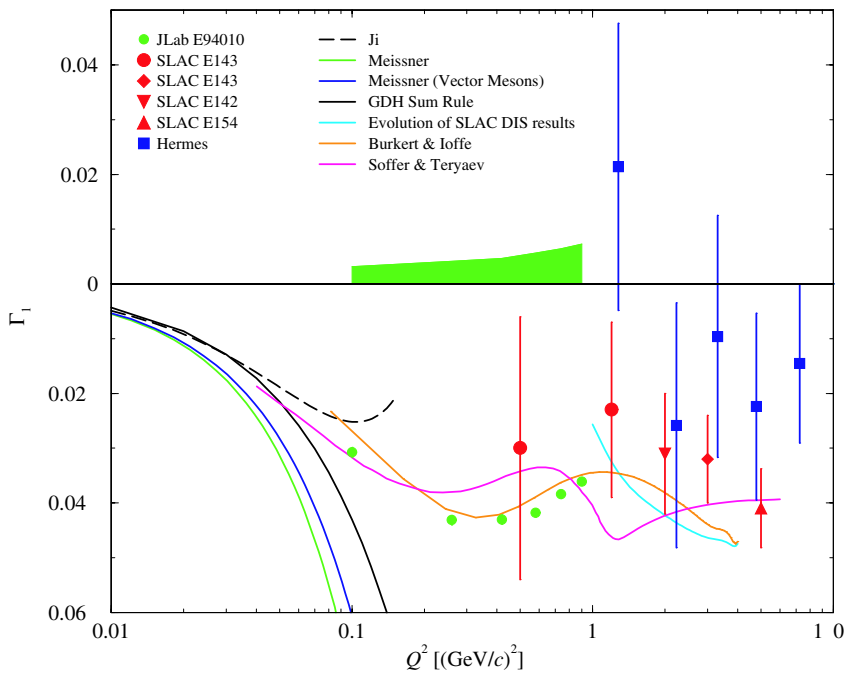

Figure 55: Integral of $g_1(x, Q^2)$ for the neutron at several fixed values of Q^2. The results of this experiment are shown in solid circles (green) and the band located around zero represents the size of systematic errors. The red solid circles are data from SLAC E143 [85] experiment dominated by the resonance region, the red solid triangle pointing down represents SLAC E142 [86] result while the red diamond shows SLAC E143 result [85]. The red solid triangle pointing up represents SLAC E154 [87] result. All blue square are Hermes experiment results [88]. At low Q^2 the solid lines corresponds to χPT calculations by Bernard *et. al.* [89] (green) without vector mesons and by Bernard *et. al.* [90] (blue curve) with vector mesons, respectively. The dashed line is a calculation by Ji *et. al.* [91,92] (black dashed line) using heavy baryon χPT. The solid black line represents the GDH result. At moderate and large Q^2 two calculations, one by Soffer and Terayev[93] (purple solide curve), the other by Burkert and loffe[94] (orange solid curve) are plotted. At large Q^2 the red line represents the evolution [96] of the world's deep-inelastic data due to the changing coupling constant α_S Soffer and Terayev assume that the integral over $g_1 + g_2$ varies smoothly from high Q^2 where $g_2 \approx 0$ down to $Q^2 = 0$. Using their simple prediction for this integral and subtracting the contribution from g_2 using the BC sum rule [95]. Burkert and loffe consider the contributions from the resonances using the code AO, and the nonresonant contributions using a simple higher-twist-type form fitted to the deep-inelastic data. Their model is constrained to fit both the GDH and the deep-inelastic limits, and it describes the data quite well.

Q^2, a region covered by our data, its conventional interpretation in terms of higher twist is not obvious but efforts to get its physical meaning at small Q^2 region are underway. A recent publication [83] gives a new insight in this regard at very low Q^2. Thus d_2 is also a quantity that can shed some light on the strong interaction in the nucleon as we study its Q^2 evolution. A second publication, almost in final draft, focuses on the study of the structure functions and their moments.

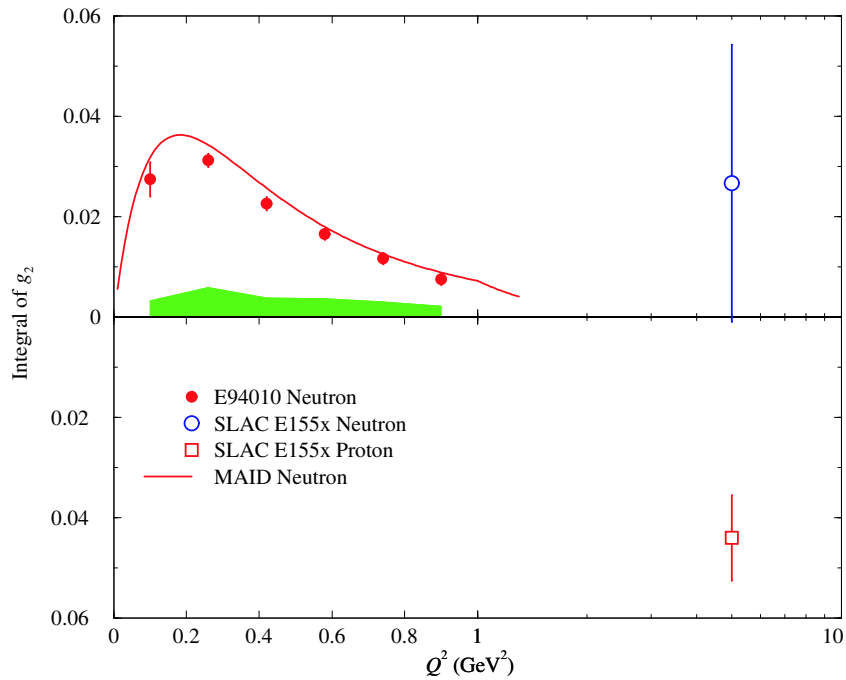

Figure 56: Integral of the neutron structure function $g_2(x, Q^2)$ extracted in E94-010 (red solid circles) at several Q^2 values reported along the SLAC E155X [98] proton (red open square) and neutron (blue open circle) results. The green band at zero represents the systematic uncertainty of this experimental result. The red curve is an evaluation of the integral using MAID [82]. Reasonable agreement between the data and the MAID prediction is observed.

A carefull analysis of the quasielastic data is underway by K. Slifer, a student of Temple University where the ultimate goal is to evaluate the extended GDH on ^3He. This sum rule is also interesting from the point of view of nuclear physics studies of ^{3}He. It allows us to investigate an important quantity in a nuclear system and has the advantage of being free from nuclear corrections uncertainties. After the completion of this analysis a full paper describing the complete experimental results of E94-010 including those of ^{3}He studies will be prepared by K. Slifer and will form his Ph.D. thesis.

Another paper is also in preparation for the investigation of spin duality of the structure function $g_1^{^3He}(x, Q^2)$. Even though preliminary, the measured $g_1(x, Q^2)$ for 0.5 GeV^2 $\leq Q^2 \leq$ 0.9 GeV^2 shows an impressive duality behavior similar to

that of $F_2(x, Q^2)$. The results from E01-012 [84] will cover Q^2 from 1 GeV^2 to 3 GeV^2 and enable a more detailed study of spin duality.

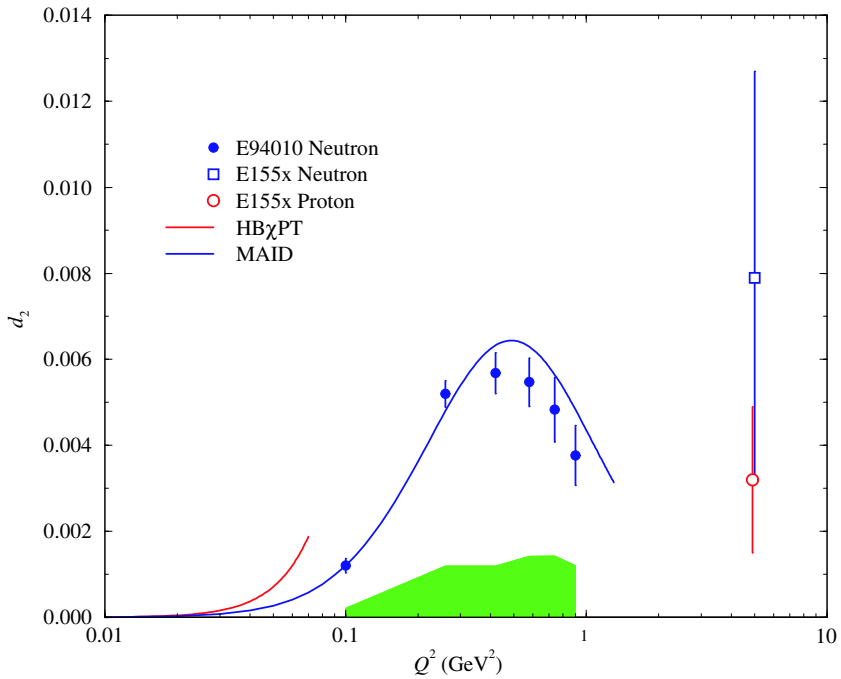

Figure 57: d_2 matrix element at several values of Q^2. The results of this experiment are shown as the red solid circles and the green band represents their corresponding sytematic uncertainty. The SLAC E155X [98] proton (red open circle) and neutron (blue open square) results are also shown. The blue curve corresponds to the MAID calculation[82]. The red curve is a Heavy Baryon χPT calculation[83] valid only a low Q^2. The Lattice prediction at $Q^2 = 5$ GeV^2 for the neutron d_2 matrix element not shown here is negative but close to zero. We note that all models predicts d_2^n to be negative or zero. The moderate Q^2 data of E94-010 show a positive d_2^n but decreasing perhaps to zero at high Q^2. The SLAC data also shows a positive d_2^n but with a rather large error bar.

4.7 Experiment E94-104

Charged Pion Photoproduction in Deuterium and ^{4}He at 1.2-5.6 GeV

H. Gao and R. J. Holt, Spokespersons
and
the Hall A Collaboration

The Hall A E94-104 collaboration performed the following measurements in early 2001, with a beam current of around 30 μA and beam energy from 1.2 to 5.6 GeV:

- Exclusive cross section measurement of $\gamma n \to \pi^- p$ with the liquid deuterium (LD2) target and $\gamma p \to \pi^+ n$ with the liquid hydrogen (LH2) target, at $\theta_{cm} = 50°, 70°, 90°$, proposed to investigate the scaling behavior predicted by the constituent counting rule [99];
- Coincidence cross section measurement of $\gamma n \to \pi^- p$ with ^{4}He target, at $\theta_{cm} = 50°, 70°, 90°$, proposed to study the nuclear transparency of ^{4}He and look for possible signs of color transparency.

Significant progress has been made in analyzing these data.

For coincidence ^{4}He data at $\theta_{cm} = 90°$, F. Xiong from MIT obtained the preliminary nuclear transparency results of ^{4}He by comparing the data from ^{4}He target to those from LD2. After Xiong's graduation in June, 2002 from MIT, D. Dutta from MIT/Duke took over the analysis and the final transparency results are expected in the near future. The plan is to have a paper ready for publication on the ^{4}He transparency result by the end of the year.

For the exclusive data with the LD2 and LH2 targets, results for the differential cross section were extracted at $\theta_{cm} = 90°$, based on which a paper was written for PRL submission. The analysis was mostly done by L.Y. Zhu from MIT. As shown in Fig. 58, the data show the global scaling behavior at high energies, as predicted by the constituent counting rule and as hinted by the previous π^+ data. But moreover, the data show possible oscillations around the scaling value, which may be caused by the interference [101,102] between hard and soft processes. Furthermore, the data also indicate a resonance structure at a center-of-mass energy near 2.2 GeV.

The cross section ratio of π^- to π^+ photoproduction can be calculated [106] based on one-hard-gluon-exhange diagrams as

$$\frac{d\sigma(\gamma n \to \pi^- p)}{d\sigma(\gamma p \to \pi^+ n)} \simeq \left(\frac{ue_d + se_u}{ue_u + se_d}\right)^2 , \tag{11}$$

where e_q is the charge of the quark q. The non-perturbative components are represented by the form factors which divide out when the ratio is taken. The

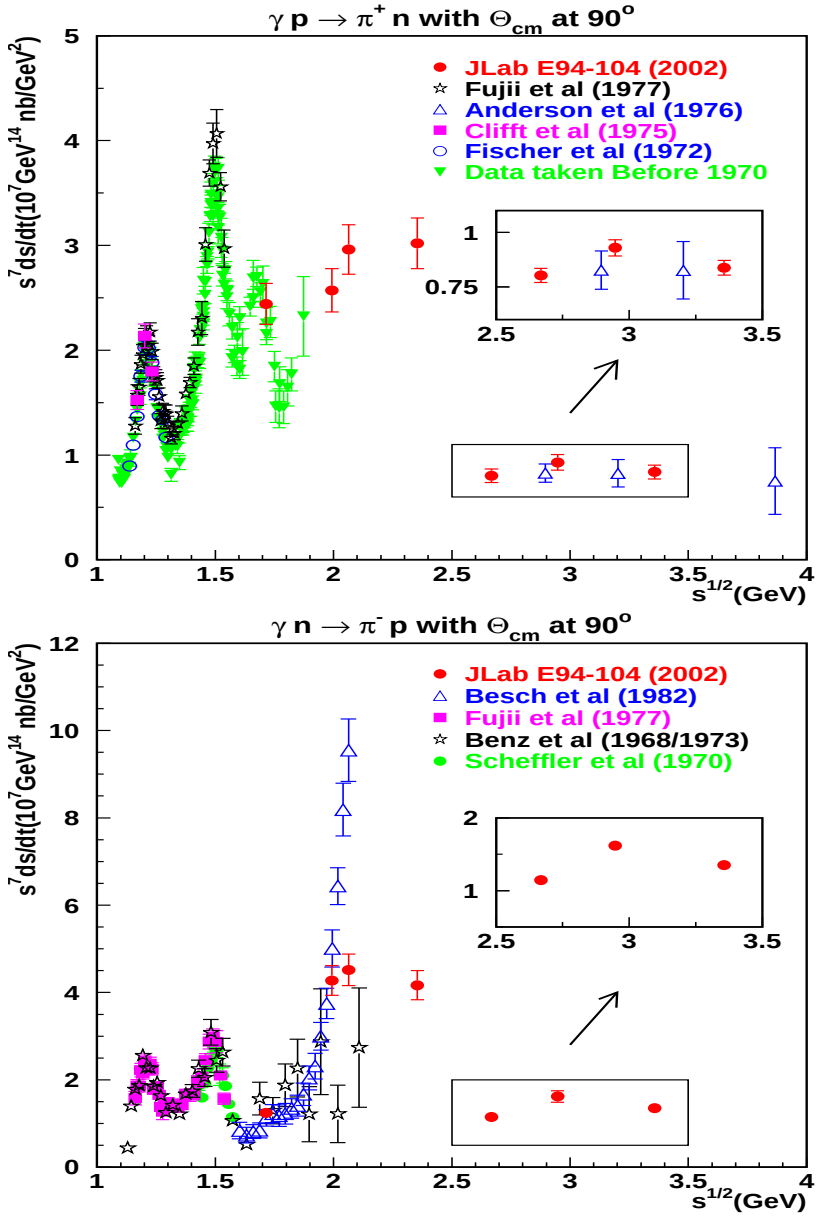

Figure 58: The scaled differential cross section $s^7 \frac{d\sigma}{dt}$ versus center-of-mass energy for the $\gamma p \to \pi^+ n$ (upper plot) and $\gamma n \to \pi^- p$ (lower plot) at $\theta_{cm} = 90°$. The data from JLab E94-104 are shown as solid circles. The error bars for the new data and Anderson *et al.*'s data [104], include statistical and systematic uncertainties, except that those in the insets only include point-to-point uncertainties to highlight the possible oscillatory scaling behavior. Other data sets are shown with only statistical errors. The open triangles in the lower plot were averaged from data at $\theta_{cm} = 85°$ and $95°$ [105].

calculation is expected to be valid only at high energy. As shown in Fig. 59, the calculation is approaching the data as the photon energy increases and the agreement is relatively good when $E_\gamma \geq 3.3$ where the scaling appears.

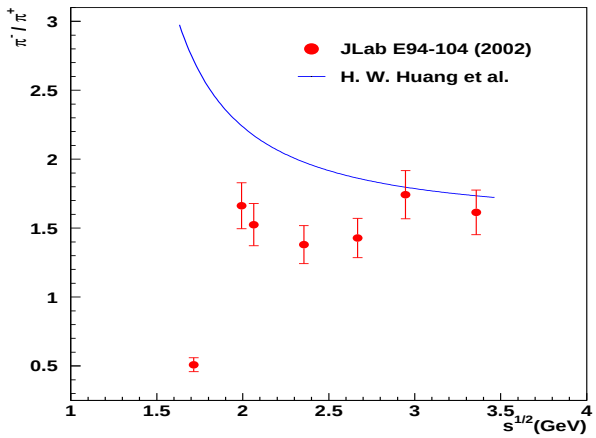

Figure 59: The cross section ratio of π^- to π^+ photoproduction versus center-of-mass energy

The data at other center-of-mass angles will be replayed and analyzed soon. It will be interesting to investigate the angular dependence of the above phenomena. A new experiment E02-010 was approved in Hall A to explore the possible oscillations around the scaling value with much finer binning in photon energies. The future 12 GeV energy upgrade at JLab will enable us to extend further these measurements and study the reactions across the charm threshold. Searching for new resonances around the charm production threshold, will help to check Brodsky and de Teramond's interpretation [107] that the oscillatory scaling behavior in pp elastic scattering arises from the opening of new charm resonance states.

4.8 Experiment E97-103

Search for Higher Twist Effects in the Neutron Spin Structure Function $g_2^n(x, Q^2)$

T. Averett and W. Korsch, Spokespersons

Experiment E97-103 was successfully completed in the late summer of 2001. Spin asymmetries were measured using longitudinally polarized electrons scattered from either longitudinal or transversely polarized ^{3}He in the inclusive reaction $^3\vec{H}e(\vec{e}, e')$. From these measured asymmetries, the neutron spin structure function $g_2^n(x, Q^2)$ can be obtained. Data were collected at five values of Q^2 (0.58, 0.80, 0.96, 1.14, 1.36 GeV^2) at fixed $x \sim 0.2$, and with $W^2 > 4$ GeV^2. The two Hall A HRS spectrometers were used independently, with separate data acquisition systems, for detecting the scattered electrons. The Hall A polarized ^{3}He target was used and reached the highest average polarization (over 40%) ever achieved with $10 - 12$ μA of beam on target. The ^{3}He nuclei were polarized through spin exchange collisions with optically-pumped, polarized rubidium atoms. The polarization direction could be oriented parallel or perpendicular to the beam line and three 30 Watt diode lasers (Coherent FAP systems) were used in each configuration for optical pumping. Target polarization was measured with using NMR and EPR systems.

By measuring both the parallel and perpendicular spin asymmetries, $A_{\|}$ and $A_{\perp}$, one can obtain the g_1 and g_2 structure functions. A correction is made to the ^{3}He results to obtain the structure functions for the neutron.

$$g_1(x, Q^2) = \frac{F_1(x, Q^2)}{D'} \left[A_{\|} + A_{\perp} \tan\theta/2\right]$$

$$g_2(x, Q^2) = \frac{F_1(x, Q^2)}{D'} \frac{y}{2\sin\theta} \left[A_{\perp} \frac{E + E'\cos\theta}{E'} - A_{\|} \sin\theta\right]$$

$$D' = \frac{(1-\epsilon)(2-y)}{y(1+\epsilon R(x, Q^2))}$$

$$\epsilon = 1/(1 + 2(1 + \nu^2/Q^2)\tan^2\theta/2)$$

$$y = \nu/E$$

The g_1 structure function has been accurately measured at SLAC (deep-inelastic) and Jefferson Lab (E94-010, quasi-elastic and resonance regions) and is directly related to the spin decomposition of the nucleon in terms of quark flavors. For g_2 however, one must look beyond simple parton model interpretations. It is generally described in the framework of the Operator Product Expansion, where the hadronic matrix element which describes the physics of g_2 is expanded in a series of operators and unknown coefficients grouped according to their *twist* [108]. The twist describes the degree to which a term contributes to the matrix element, where terms with successively higher twist are suppressed by additional factors

of $1/\sqrt{Q^2}$. Leading twist (twist=2) describes the case where the virtual photon probes a single, non-interacting quark. This contribution is also the leading contribution to the g_1 structure function. The twist=3 contributions arise when the virtual photon interacts with a quark that is simultaneously exchanging a gluon with another quark. These twist=3 terms do not contribute to g_1, which means that a precise measurement of g_2 allows one to isolate and quantify the most basic quark-quark interactions within the nucleon.

Based on the Operator Product Expansion, Wandzura and Wilczek [109] derived the following expression for the *twist=2* part of g_2:

$$g_2^{ww}(x, Q^2) = -g_1(x, Q^2) + \int_x^1 dy \frac{g_1(y, Q^2)}{y}$$

Thus, by measuring g_2 precisely and subtracting the leading g_2^{ww} contribution, one is left with only the twist=3 and higher contributions to g_2.

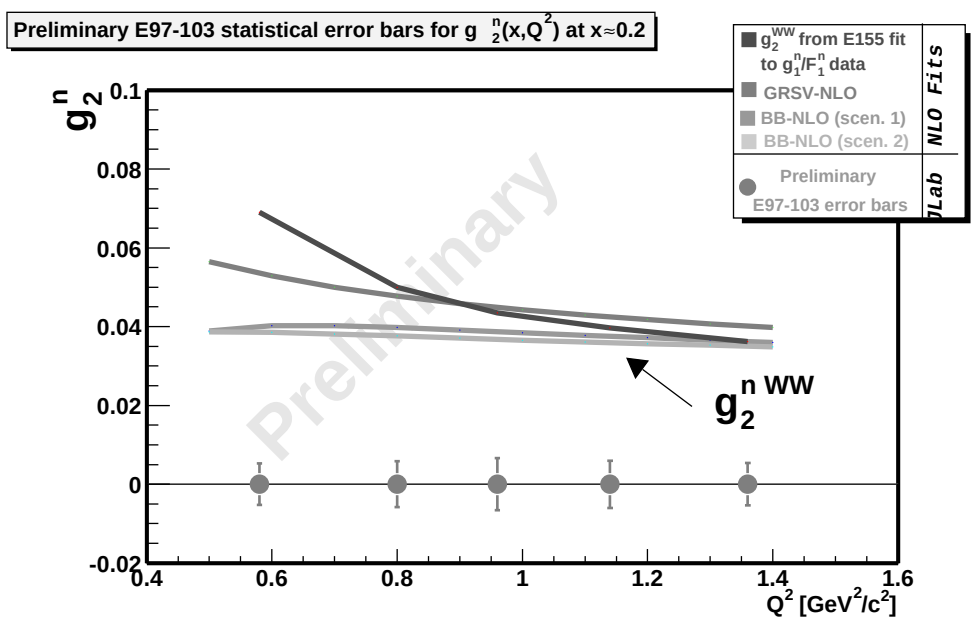

Figure 60: Preliminary results from E97-103 showing errors only. Also shown are calculations of the g_2^{ww} using various fits to the world data on g_1.

The raw asymmetries measured in this experiment were at the 10^{-3} to 10^{-4} level and great care was taken to ensure there were no significant false asymmetries. In particular, a third DAQ system based on the HAPPEX system was used to continuously monitor the beam charge asymmetry. This information was fed to the polarized source every ten minutes, where a feedback system was used to zero the charge asymmetry with a rotatable half-wave plate at the source laser. Charge asymmetries were consistently kept well below the 50 ppm level. Data

were also taken during the commissioning period using quasi-elastic scattering from thin carbon targets. The asymmetry from the carbon target was measured to be -67 ± 46 ppm in the left spectrometer, and -52 ± 45 in the right, which gives us confidence in our control of false asymmetries.

The data collected in E97-103 will allow us to calculate g_2^n at five values of Q^2, each with an absolute statistical error $< 10^{-2}$, which is an order of magnitude improvement over existing data from SLAC (Experiment E155x, preliminary results). Analysis of the raw data has been completed and a clean set of asymmetries has been extracted. Current analysis is focusing on radiative corrections, which will be followed by a study of the dilution factor and systematic errors. It is expected that near final results will be obtained in early 2003, with a publication expected before summer of 2003. Preliminary results showing errors only is shown in Fig. 60 along with g_2^{ww} calculated using various parameterizations of the world g_1 data [110–112].

4.9 Experiment E97-111

Systematic Probe of Short-Range Correlations via the Reaction ^{4}He(e,e′p)^{3}He

B. Reitz
for
the Hall A and E97–111 Collaborations.

Experiment E97-111 took data in September and October 2000. The goal of the experiment is to provide cross sections for the reaction $^4\mathrm{He}(e,e'p)^3\mathrm{H}$ at recoil momenta up to 500 MeV/c in various kinematics. Many calculations have predicted a sharp minimum in the spectral function of $^4\mathrm{He} \rightarrow t + p$ for those recoil momenta. The location of this minimum, as well as the height of the second maximum are sensitive to the details of the nucleon–nucleon interaction used in those calculations, whereas the occurrence of the minimum itself is a feature of most of the exact calculations available.

The minimum is predicted to occur at relatively large values of p_m, therefore we are especially sensitive to the short–range part of the nucleon–nucleon interaction. Theoretical calculations appear to verify this. The data will provide a testing ground for exact nuclear-structure calculations with realistic forces.

The experiment is also designed to study the effects of reaction dynamics such as final state interactions, meson-exchange currents, and isobar configurations to the cross section. Because the spectral function goes to zero at some value of p_m in the examined region, the observed cross section must be due to those contributions. Therefore the spectral function has been measured for the same region of p_m in a variety of configurations, to study several proposals how to suppress reaction mechanism contributions. Part of the data was taken in the constant-q-ω approach, where p_m is varied by changing the recoil momentum of the proton, leaving the electron kinematics unchanged. The second part of the data was taken in parallel kinematics, where the momentum of the proton is parallel to the momentum transfer axis. Details of the kinematical settings have been published in the previous Hall A annual status report.

The first–pass online analysis did not show a clear signature of the expected minimum, but did also not rule it out completely. Data on elastic electron scattering off ^{3}He, taken at the same kinematics during the experiment, have been analyzed, with respect to obtaining absolute yield factors. The effect of different beam currents on the target density have been studied. Electronic dead time studies have been performed. Optics and pointing data have been analyzed, and the optics database has been optimized, the detector and spectrometer offsets have been determined. Therefore the necessary tools and preparations for the next replay are nearly finished, and the next replay of the data should start end of this year. In parallel studies of trigger and tracking efficiencies are necessary and ongoing for the next iteration of the analysis.

4.10 Experiment E98-108

Electroproduction of Kaons upto Q^2= 3 (GeV/c)^2

P. Markowitz and M. Coman for O.K. Baker, C.C. Chang, S. Frullani, M. Iodice
and
the Hall A and E98-108 Collaborations [1]

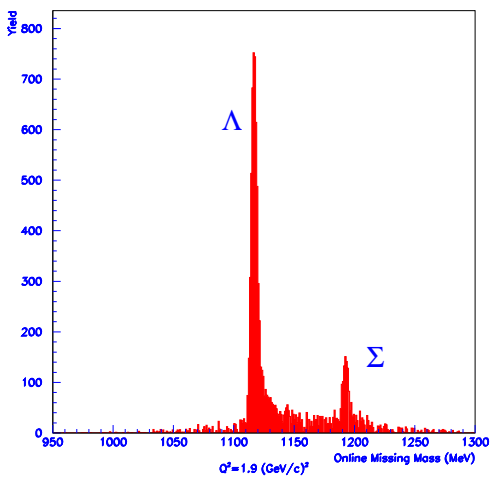

Figure 61: The online missing mass yield taken in March 2002 at $Q^2 = 1.9$ (GeV/c)^2, $W = 1.95$ GeV and $t = t_{min}$.

The E98-108 collaboration [2] collected data initially in January, March and April 2001 and finished running in March 2002. [Shown above in Fig. 4.10 is the online missing mass spectra from the first of the March 2002 kinematics.] At a total of 30 kinematics points, the experiment measured the $H(e, e'K^+)Y$ cross section. Kinematics used momentum transfers of 1.90 and 2.35 (GeV/c)^2 and invariant masses between 1.8 and 2.2 GeV to measure the cross section as a function of ε (the photon longitudinal polarization), as well as measurements left and right of the direction of $\vec{q}$. Preliminary σ_L, σ_T, and σ_{LT} cross sections have been extracted from the data. The transverse cross section σ_T, and longitudinal-transverse interference cross section σ_{LT} is used to constrain the reaction mechanism. The behavior of the longitudinal cross section σ_L is mapped as a function of the Mandelstam variable t at fixed Q^2. The kaon form factor is expected to be senstivity to σ_L, albeit in a model dependent way. The data will allow the kaon electroproduction reaction mechanism to be determined and eventually allow the kaon form factor to be modelled as well.

[1] http://www.jlab.org/ markowit/index.html
[2] O. K. Baker, C. C. Chang, S. Frullani, M. Iodice, P. Markowitz, spokespersons

The doctoral students analyzing the data (Marius Coman of Florida International University) is presently focussing on the systematic analysis (acceptance, normalizations, efficiencies and calibrations). For example, target "boiling" corrections are typically 4–6%, while VDC efficiency corrections (both for the detector firing all four planes and for reconstructing one unique track) typically total 20%. The wire chamber efficiency, electronic and computer deadtimes, and cut efficiencies have been determined. Radiative corrections have been done using the MCEEP simulation code; a comparison to the SIMC simulation code is underway.

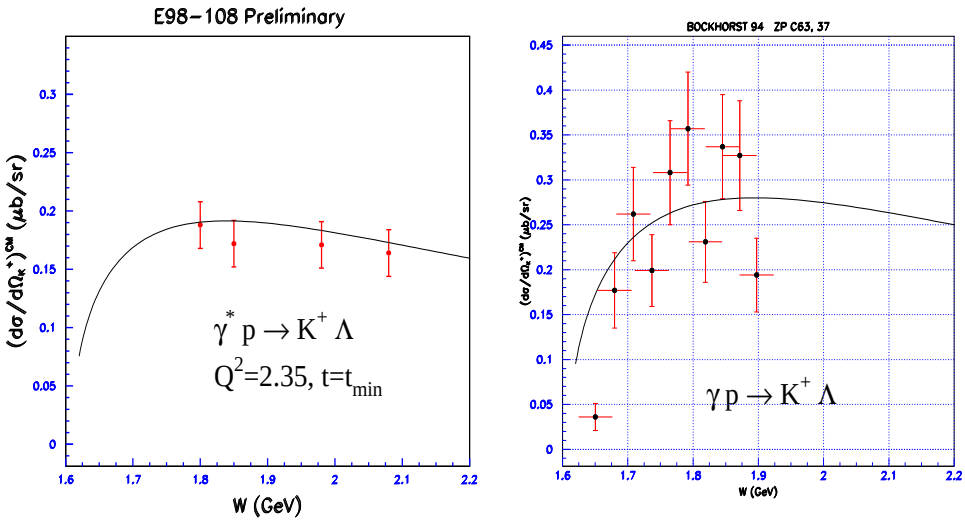

Figure 62: Shown on the left are the preliminary H(e,e′K$^+$) cross section results as a function of the invariant mass, W. On the right is the published real photon data of Bockhorst *et al.* from SAPHIR plotted with the same empirical fit to the W-dependence.

The experiment required building two new aerogel Čerenkov radiation detectors with indices of refraction of 1.015 and 1.055. The first detector, due to the low index of refraction, required special handling of the delicate aerogel radiator. The first detector fired only on pions or lighter particles, but not on kaons or protons. The second aerogel was built primarily by the MIT group and fired on either kaons or protons but not pions. The use of two aerogels in anticoincidence is a novel PID idea. The response of the two new aerogels as a function of momenta has been studied in detail for protons, kaons and pions.

The preliminary cross section results as a result of the invariant mass W are shown in Fig. 4.10. The left panel shows the Hall A data at Q^2=2.35 (GeV/c)^2 along with an empirical curve describing the W-dependence in terms of phase space and a resonance at 1.72 GeV. The right panel shows the real photon data (Q^2=0) published by the SAPHIR [113] collaboration. The same dependence is shown in both plots, indicating that the W-dependence is understood. The error bars will decrease by a factor of 4–5 when the analysis is final.

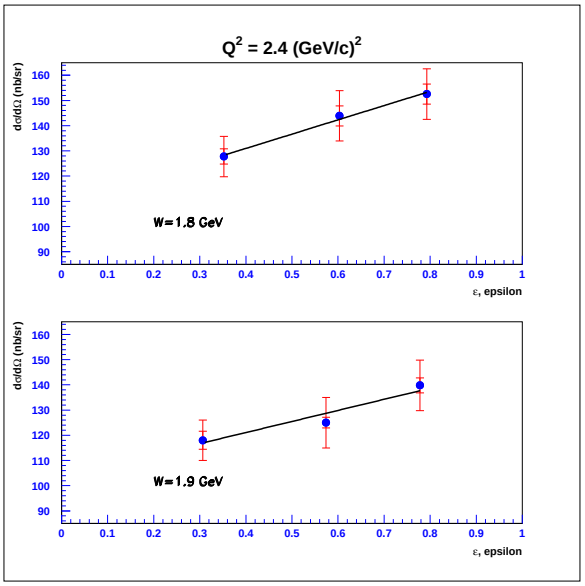

Figure 63: Shown are the preliminary H(e,e′K$^+$) separated cross section versus $/varepsilon$. Final error bars will be 4–5 times smaller.

The preliminary separated cross sections for two values of W, 1.9 and 2.4 GeV are plotted versus ε in Fig. 4.10. The four-momentum transfer squared was $Q^2 = 2.4$ (GeV/c)^2. The quality of the data can be seen from the linearity of the points. Presented uncertainties are overly cautious; again, the error bars will decrease by a factor of 4–5 when the analysis is final. There is no previous separation at this Q^2 to compare to.

4.11 Experiment E99-114

Exclusive Compton Scattering on The Proton

Ch. Hyde-Wright, A. Nathan, B. Wojtsekhowski
and
the Hall A Collaboration

Real Compton scattering or RCS ($\gamma + p \rightarrow \gamma + p$) at high energy ($s$) and high momentum transfer (t) is a potentially powerful probe of the short-distance structure of the nucleon. It is a natural complement to other studies of nucleon structure, including high Q^2 measurements of the elastic electric and magnetic form factors, virtual Compton scattering, and deep inelastic scattering. In this experiment we realized a full survey of Compton scattering from the proton up to an energy 5.4 GeV.

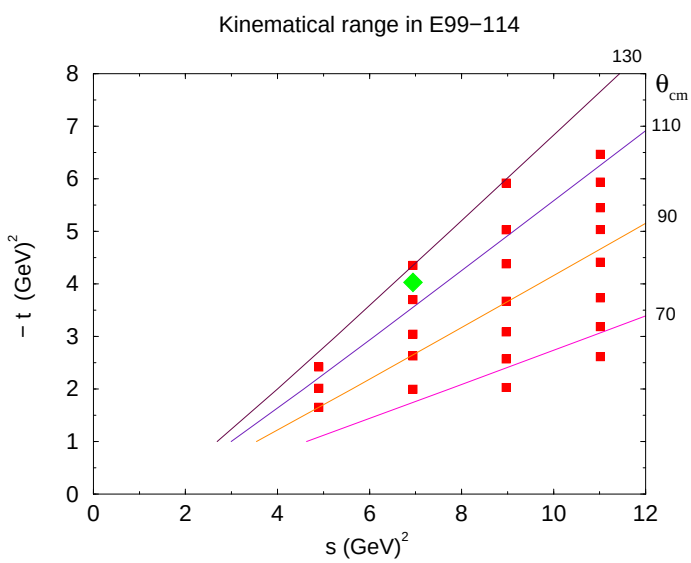

Figure 64: Kinematic coverage of E99-114 measurements.

The goals of the RCS experiment are to study the reaction mechanism and to measure new form factors of the proton. These will be accomplished through accurate determination of the unpolarized scattering cross section over a broad range of s and t and a measurement of the longitudinal polarization transfer K_{LL} at a single kinematic point. Together, these measurements should provide a stringent test of the two competing reaction mechanisms. In the handbag mechanism, there is a single active quark that couples to both the incoming and outgoing photon and which couples to the proton via the overlap of soft components of the proton wave function, leading to new form factors that are similar to but distinctly different form those measured in elastic electron scattering. In the pQCD mechanism, all

three valence quarks actively participate in the reaction, which is mediated by the exchange of two hard gluons. The two mechanisms differ in their predictions of the absolute scale of the cross section, the scaling behavior of the cross section at fixed θ_{cm} and fixed t, and in the magnitude and even the sign of various polarization observables. The analysis of the experiment should shed light on all these aspects of RCS.

This experiment is the subject of four Ph.D. theses: M. Roedelbronn (UIUC), D. Hamilton (Glasgow), A. Danagulian (UIUC), and V. Mamyan (Yerevan). The very preliminary results of the experiment were presented in the workshop "Exclusive Processes at High Momentum Transfer" at JLab in May 2002. We took the complete E99-114 data set in January-February of 2002. Data were obtained in a total of 24 kinematic settings. Figure 4.11 indicates the values of s and t of the data points.

The electron beam intensity for some of these points was 40 μA or 4 times larger

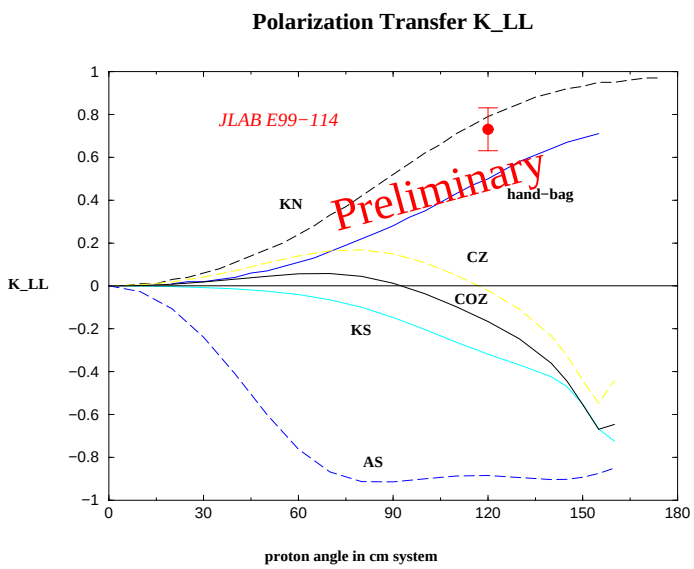

Figure 65: Polarization transfer in the RCS process. The labels on the curves are KN for the asymmetry in the hard subprocess; the pQCD calculations [115] with AS for asymptotic distribution amplitudes, CZ for Chernyak-Zhitnitsky, COZ for Chernyak-Ogloblin-Zhitnitsky, and KS for King-Sachrajda; hand-bag for calculations in Soft overlap approach [116].

than projected in the proposal. The photon flux was up to 1200 times higher than in the Cornell experiment [114]. A partial but crude analysis of the raw data was done on line. The analysis of the polarization transfer part of the data is in progress. The preliminary result on parameter K_{LL} is shown in Fig. 4.11. This indicates an agreement with the handbag (or soft overlap) calculation but not with the pQCD calculation.

4.12 Experiment E99-117

Precision Measurement of the Neutron Asymmetry A_1^n at Large x
Using CEBAF at 6 GeV

X. Zheng
for
J.-P. Chen, Z.-E. Meziani, and P. Souder, Spokespersons
and
the Hall A Collaboration

During experiment E99-117 we have measured the neutron spin asymmetry $A_1^n(x, Q^2)$ at three deep inelastic (DIS) kinematics : $x_{Bj} = 0.33$, 0.48, 0.61, with $Q^2 = 2.7$, 3.6, 4.9 $(\mathrm{GeV/c})^2$, respectively. It ran successfully in Hall A during the period June 01, 2001 to July 31, 2001. Data were collected on the electron parallel and perpendicular asymmetries of $\vec{e} - {}^3\vec{\mathrm{He}}$ deep inelastic scattering. The polarized electron beam was used at a beam energy 5.7 GeV and a polarization of $P_b \sim 80\%$. The Hall A polarized ^{3}He target was used with an (in beam) polarization of $P_t > 40\%$. The scattered electrons were detected by the two HRS spectrometers at symmetric positions, at either $\pm 35°$ or $\pm 45°$. The asymmetries A_1, A_2 and the ratio of structure functions g_1/F_1, g_2/F_1 were evaluated from the measured asymmetries following

$$
\begin{aligned}
A_1 &= \frac{A_\parallel}{D} - \frac{\eta A_\perp}{d} \\
\frac{g_1(x,Q^2)}{F_1(x,Q^2)} &= \frac{1}{D'}\Big[A_\parallel + \tan(\theta/2)\cdot A_\perp\Big] \\
A_2 &= \frac{\xi A_\parallel}{D(1+\eta\xi)} + \frac{A_\perp}{d(1+\eta\xi)} \\
\frac{g_2(x,Q^2)}{F_1(x,Q^2)} &= \frac{1}{D'}\frac{y}{2\sin\theta}\Big[\frac{E+E'\cos\theta}{E'}A_\perp - \sin\theta\cdot A_\parallel\Big]
\end{aligned}
$$

In order to cancel possible systematic effects due to the electron beam helicity and target spin direction, the beam helicity and the target spin directions in the parallel settings were reversed. The measured asymmetries from all four possible configurations were averaged to obtain the final result. The beam helicity was also reversed for the perpendicular settings, but the target spin direction was not, due to hardware limitations. The sign of the asymmetries in each configuration of beam and target spin directions was determined by measuring well known asymmetries. In our case, the $\vec{e} - {}^3\vec{\mathrm{He}}$ elastic longitudinal asymmetry was measured to determine the sign convention for the parallel settings of our DIS measurements. The $\Delta(1232)$ transverse asymmetry was measured to determine the sign for the perpendicular settings of our DIS measurements. The third and final round of analysis has been completed. For the asymmetry analysis, we have carefully

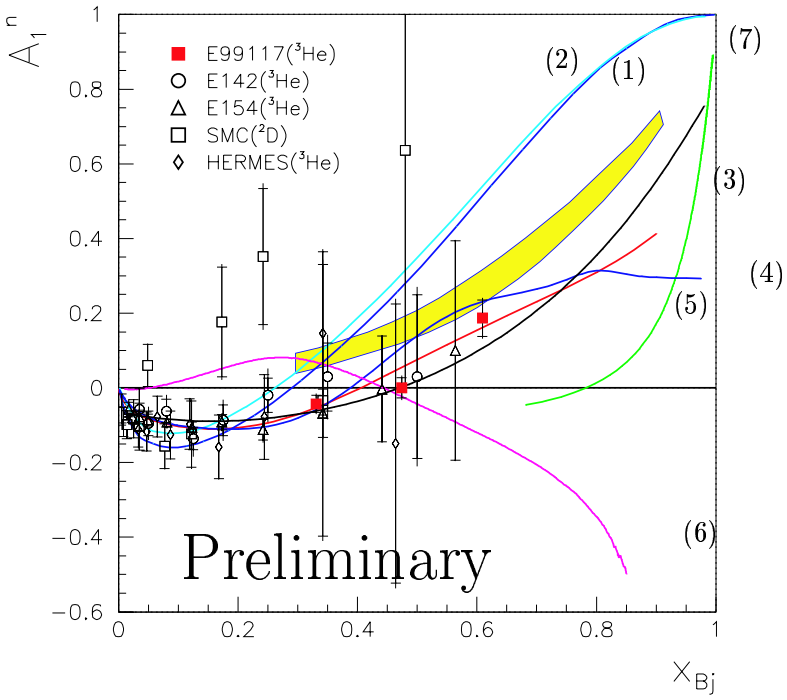

Figure 66: A_1^n results compared with theoretical predictions. Curves: predictions of g_1^n/F_1^n from pQCD HHC based BBS parametrization (1) and LSS(BBS) parameterization (2), g_1^n/F_1^n from LSS 2001 parametrization at $Q^2 = 5$ (GeV/c)^2 (3); predictions of A_1^n from constituent quark model (light shaded band), statistical model at $Q^2 = 4$ (GeV/c)^2 (3), local duality (4), chiral soliton model at $Q^2 = 3$ (GeV/c)^2 (5), and E155 fit at $Q^2 = 4$ (GeV/c)^2 (6). Data from Hermes and SLAC are original values without being re-analyzed for the new nuclear corrections.

checked various effects in the helicity dependent deadtime corrections, PID efficiencies, acceptance effects, and BPM corrections. Radiative corrections for the asymmetries $A_{\parallel}^{^3\mathrm{He}}$, $A_{\perp}^{^3\mathrm{He}}$ have been performed. The internal radiative corrections were performed using POLRAD 2.0, with the most up-to-date world fit for the proton, deuteron structure functions, EMC effects, and the neutron data from this experiment. The external radiative corrections were done using a single arm Monte-Carlo (SAMC) program, an improved version of E94-010 simulation code. The error due to radiative corrections was studied by using various world fits for the structure functions.

A full error analysis has been performed for A_1^n showing that the total error bar is still dominated by statistical accuracy of the measurement.

For the cross section analysis, we used SAMC program to simulate both elastic and inelastic analysis. The latest version of Hall A HRS transport functions were used. R-function was used for acceptance evaluation. Radiative effects were taken into account using the procedure first described by Mo& Tsai. Results of $\vec{e} - {}^3\vec{\mathrm{He}}$ elastic analysis show good agreement with the simulation. The asymmetry agrees with the simulation at a level of $|(A_{\parallel}^{el} - A_{\parallel}^{el,MC})|/A_{\parallel}^{el} < 4\%$ and the cross section agrees at the level of $|(\sigma^{el} - \sigma^{el,MC})|/\sigma^{el} < 5\%$. This agreement is well within the expected systematic uncertainty. For the deep inelastic analysis, we used F2NMC95 and R1998 to determine the the cross section. The elastic and quasi-elastic tails were simulated using the peaking approximation. The inelastic cross

section results agree with the simulation at a level of $|(\sigma^{dis} - \sigma^{dis,MC})|/\sigma^{dis} < 10\%$, for all three kinematics. We therefore used the world fit of $F_1^{^3\mathrm{He}}$ to obtain $g_1^{^3\mathrm{He}}$ from $g_1^{^3\mathrm{He}}/F_1^{^3\mathrm{He}}$ results.

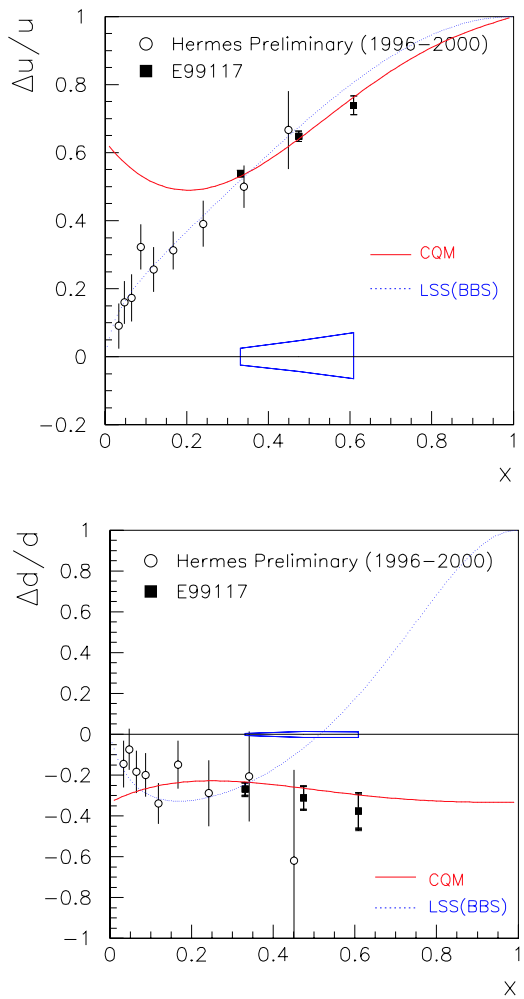

Figure 67: $(\Delta u + \Delta\bar{u})/(u + \bar{u})$, $(\Delta d + \Delta\bar{d})/(d + \bar{d})$ Hermes data error bars are statistical only. Error band in the middle shows the uncertainty due to neglecting s, $\bar{s}$ contribution.

We have obtained good precision results for the longitudinal asymmetry and structure functions ratio $A_{\parallel}^{^3\mathrm{He}}$, $A_1^{^3\mathrm{He}}$, $g_1^{^3\mathrm{He}}/F_1^{^3\mathrm{He}}$, and A_1^n, g_1^n/F_1^n. The data at $x_{Bj} = 0.48$ and 0.61 have improved the statistical accuracy of world data by one order of magnitude. We also have obtained results for the transverse asymmetry and structure functions ratio $A_{\perp}^{^3\mathrm{He}}$, $A_1^{^3\mathrm{He}}$, $A_2^{^3\mathrm{He}}$, $g_2^{^3\mathrm{He}}/F_1^{^3\mathrm{He}}$, and A_2^n, g_2^n/F_1^n. Although with less statistics, the precision of the neutron transverse results is comparable with the latest world data from E155x.

In Figure 66 we compare the A_1^n results with several calculations. Firstly, the datum at $x = 0.33$ agrees with the world data. Secondly, the three new data points

show a zero crossing point at $x \approx 0.48$ and the datum at $x = 0.61$ is significantly positive. The new data show a clear trend of A_1^n turning positive at large x_{Bj}. Pion asymmetries were obtained as a byproduct of the experiment.

Combined with the world g_1^p/F_1^p data and the d/u ratio, we have extracted polarized parton distribution functions $(\Delta u + \Delta\bar{u})/(u + \bar{u})$, $(\Delta d + \Delta\bar{d})/(d + \bar{d})$. In Figure 4.12 we show the results of flavor decomposition of polarized quark distributions. The error band in the middle shows the effect of neglecting strangeness contribution Δs and s, estimated using CTEQ6M pdf's. To compare with CQM predictions, which are only for valence quarks $\Delta u_V/u_V$ and $\Delta d_V/d_V$, we again used CTEQ6M pdf's to estimate the effect of neglecting sea quarks and obtain

$$\Delta u_V/u_V = \Big(\frac{\Delta u + \Delta\bar{u}}{u + \bar{u}}\Big)^{+0.03}_{-0.015}, \qquad \Delta d_V/d_V = \Big(\frac{\Delta d + \Delta\bar{d}}{d + \bar{d}}\Big)^{+0.069}_{-0.035} \tag{12}$$

4.13 Experiments E00-007 & E00-107

Proton Polarization Angular Distribution in Deuteron Photodisintegration /
Proton Polarization in Deuteron Photodisintegration
at $E_\gamma > 3$ GeV and $\theta_{\rm cm} = 90°$

R. Gilman, R. Holt, X. Jiang, Z.-E. Meziani, and K. Wijesooriya, Spokespersons,
and
the Hall A Collaboration.

The experiments were scheduled to run on an accelerated schedule, being scheduled in early September 2002 to run for 23 days starting September 20. There were 42 days from the notification that the experiments could run to the end of run party. While the experiments lost large amounts of time, arising from several problems, E00-007 was completed, and a start was made on E00-107.

The experiments were slowed up by several problems, mostly with the cryotarget. Only loop 2 of the cryotarget was used, initially with LH_2 for *ep* calibrations of the polarimeter, and later with LD_2 for γd physics data. The ^{12}C optics target was initially unavailable due to positioning problems. Target positioning difficulties coupled with apparently poor beam tunes from the accelerator, believed to be related to preparations for G0 beam delivery to Hall C, led to intermittently large backgrounds and poor data quality in some kinematics; these settings were repeated. The experiment was also slowed by a low maximum current from the high-polarization diode laser, until it was replaced for the last four days of the experiment. In contrast, the experiment was helped by excellent uptimes, often over 7 hours per shift, and high beam polarization. Several Moller polarimeter measurements showed beam polarization was consistently near 80%.

The initial data taking consisted of about 10% (relative) calibrations of the focal plane polarimeter (FPP) analyzing power, at momenta of 2.4, 2.2, 2.0, and 1.7 GeV/c. (No results are available to be quoted at this time.) These measurements used coincident *ep* scattering at 4.056 GeV beam energy. To improve the polarimeter performance, the left arm was configured as shown in Table 12, with two analyzers to improve the efficiency of detecting scattered particles. In this configuration, the front straw chambers determine both whether particles have scattered from the front analyzer, and the trajectory into the rear analyzer. By splitting the analyzer into two shorter halves, the inefficiencies that result from absorption of protons in a single thick analyzer are reduced.

After finishing the 4 GeV *ep* calibrations, about one shift was needed to switch cryotarget loop 2 from LH_2 to LD_2, and to change the beam energy from 4.056 GeV to 2.056 GeV. For four days, $\vec{\gamma}d \to \vec{p}n$ data, along with some background and optics target data, were taken with low currents, until the injector diode laser was replaced with a spare. Recoil polarization data were obtained at five center-of-mass angles, 37°, 53°, 70°, 90°, and 110°. Data for 110° were low enough in momentum to be taken with only the standard carbon FPP analyzer, obviating an

ep calibration for this point. Estimated absolute statistical uncertainties on the polarization observables p_y, C_x, and C_z are in the range 0.05 - 0.10. At this point, the additional uncertainty from extra backgrounds from the target cells, related to the beam tuning and the cells being skewed relative to the beam, are not certain. Systematic uncertainties should be smaller than the statistical uncertainties.

Detector	**Function**
VDCs	tracking
S1	trigger
A1	π rejection
S0	trigger
CH_2	FPP front analyzer
straw chambers 1 and 2	FPP tracking
S2	-
Carbon	FPP rear analyzer
straw chambers 3 and 4	FPP tracking
π rejector / lead glass	-

Table 12: The left arm detector stack used in the experiment.

Data taking is complete for E00-007, as the PAC approved beam time and goals of the experiment have been essentially obtained. The final analysis of the *ep* calibration and the γd data for this experiment will likely require several months.

Due to the loss of beam time, no data were taken for E00-107 at 3 GeV, the main goal of this experiment, during this run period. The 2.4 GeV/c *ep* calibration point does calibrate the polarimeter for the 3 GeV, 90° datum requested for E00-107. Also, the 90° datum at 2 GeV was taken in part to satisfy the PAC request that we measure a lower energy, 90°, data point to check the dual FPP data against our earlier data [117] with only the carbon analyzer, to assure the quality of the dual analyzer data.

4.14 Experiment E00-102

Testing The Limits of The Single Particle Model In ^{16}O$(e, e'p)$

W.L. Hinton
for
the Hall A and E00-102 Collaborations

The E00-102 collaboration completed taking data in December 2001 [118]. The goals of this experiment are to determine:

- the limits of validity of the single-particle model of valence proton knockout
- the effects of relativity and spinor distortion on valence proton knockout using the diffractive character of the A_{LT} asymmetry;
- the bound-state wave function and spectroscopic factors for valence knockout;

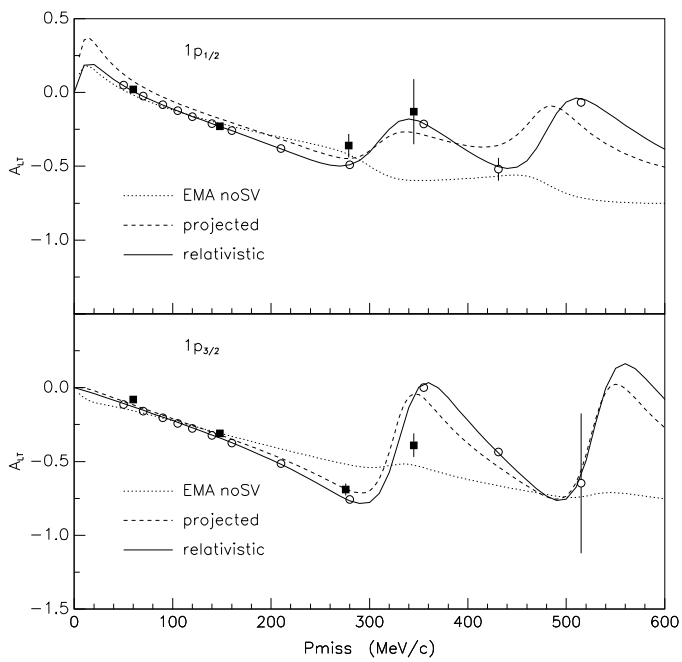

Figure 68: Projected A_{LT} data in comparison to calculation of Udias et al. The solid squares are the E89-003 data obtained in slightly different kinematics. The open circles represent the anticipated data from E00-102. Figure courtesy J.M. Udias

This experiment is the second phase of ^{16}O(e,e'p) measurements, the first phase was completed by E89-003 up to p_{miss} =0.345GeV/c [15,119,120]. The data set contains the 1p-shell, $1s_{1/2}$ state and continuum. The R_{LT} response and A_{LT}

asymmetry will be separated for -0.515 GeV/c $<$ p_{miss} $<+0.515$ GeV/c for the 1p-shell states. Figure 68 shows A_{LT} as a function of missing momentum for the 1-p shell states. The figure compares data from E89-003, Udias theoretical calculation and the anticipated data points from E00-102. The cross section will be determined out to p_{miss} = 0.750 GeV/c to determine the point where the two-nucleon effects become important and single-nucleon knockout calculations fail.

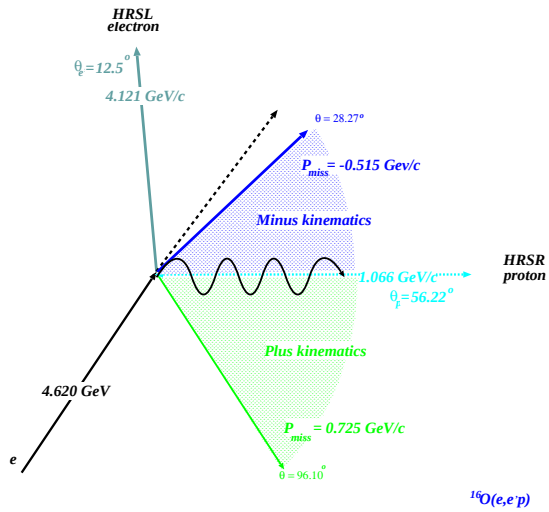

Figure 69: The experiment kinematics. HRS_l was fixed at 12.5^o throughout the experiment. HRS_r rotated about the $\vec{q}$.

The beam energy was fixed at 4.620 GeV/c giving $\vec{q} = 1.066$ and $\theta_q = 56.22^o$ The electron arm, HRSL, was fixed for the entire experiment at 12.5^o and 4.121 GeV/c central momentum. This allow the e lectron arm to be used as a continuously as a luminosity monitor. The proton arm, HRSR, angle was varied from 28.27^o to 96.10^o. This covers a missing momentum range from -0.515 GeV/c to +0.755 GeV/c. Figure 69 shows a drawing of the kinematics setup of this experiment.

The target was a three foils waterfall target [121,122]. The foils were separated by 25.4 mm each at an angle of 57.4^o with respect to the beam direction. Each foil was 125 mg/cm^2 thick. The hydrogen in the water will be used to calibrate kinematics and for normalization using the ^{1}H(e,e'p) and ^{1}H(e,e') known cross sections.

The detector stacks for both arm were used in their normal configurations. Both arms contained an addition S0 scintilator for the purpose of checking trigger efficiency. The pion rejector was used in HRSL for an additional particle identification check of π^-.

The version of ESPACE has been updated for the analysis to version 3.0. Optimization has been completed for the various detectors. The optics for the HRSR and HRSL has been checked and determined to be correct. The mispointing has been determined and corrected in the header files for each kinematic setting. HRSL was used as a check for the HRSR mispointing since the spectrometer did not move during the experiment. The data quality has been checked using a database which was generated from the end of run information and scaler information for each run. At this point the first pass of ESPACE is under way. The first task will be to calculate the H(e,e'p) and H(e,e') cross sections. After this we will begin to replay the ^{16}O data to calculate the cross sections and R_{LT} and A_{LT} for each kinematic point.

4.15 Experiment E01-001

New Measurement of (G_E/G_M) for the Proton

J. Arrington and R. E. Segel, for the E01-001 Collaboration.

Historically, the proton electric and magnetic form factors have been extracted from elastic cross section measurements using the Rosenbluth technique. The form factors have been extracted out to $Q^2 \approx 9$ (GeV/c)^2, but for large Q^2 values, the cross section is almost completely dominated by G_M, and the uncertainties on G_E become extremely large. Recoil polarization measurements of elastic scattering are sensitive to the ratio of electric to magnetic form factors, and thus provide much more precise information on the electric form factor at high Q^2 values. Recent measurements in Hall A [67,68,123] have for the first time used recoil polarization measurements to extract the ratio of G_E/G_M at high Q^2. These new results have greater precision than the previous Rosenbluth extractions at high Q^2 values, but are inconsistent with the old results, even in the region where both techniques have high precision. Figure 70 summarizes the present situation. Assuming that the polarization transfer results are correct, this disagreement indicates either a fundamental difference in the two techniques for extracting the form factors, or a significant problem with the previous cross section measurements [124].

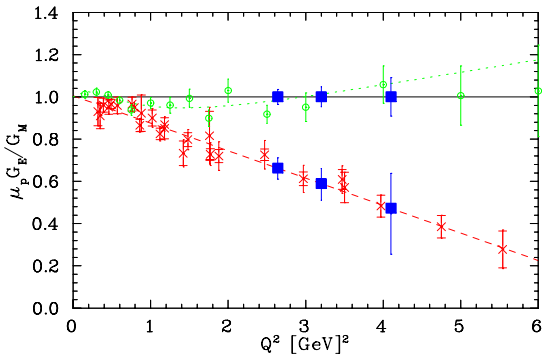

Figure 70: Projected uncertainties for E01-001 (blue squares), along with a global analysis of the Rosenbluth data (green circles), and the polarization transfer measurements from Hall A (red crosses).

E01-001 was designed to check the consistency of the recoil polarization and Rosenbluth techniques by making a high precision Rosenbluth separation in the region where the two techniques disagree. The experiment ran in May of 2002, and took data at Q^2=2.64, 3.2, and 4.1 (GeV/c)^2. Figure 71 shows the ϵ points measured at each of the three Q^2 values. In addition, coincidence elastic measurements were taken at two kinematics. These measurements will be used to check spectrometer efficiencies, radiative corrections, and the background of the inclusive spectra. Because of lost beamtime and problems with some of the data collected, we have reduced statistics and background runs at the highest Q^2. While

the errors for the high Q^2 point will be ~50% larger than originally desired, the lower Q^2 points have just a 5-10% reduction in their precision, and will still be able to distinguish form factor scaling from the linear falloff observed in the polarization transfer results to better than six standard deviations. Figure 70 shows the existing polarization transfer data [67,123], a global analysis of the Rosenbluth data [125], and the projected uncertainties for E01-001. The projected data are shown for two different values of the extracted ratio: $\mu_p G_E/G_M = 1$ and $\mu_p G_E/G_M = 1 - 0.13(Q^2 - 0.04)$.

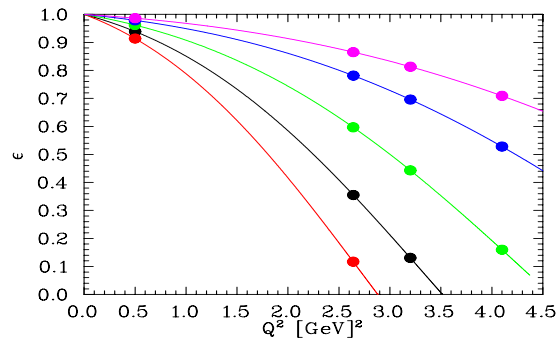

Figure 71: Kinematics for E01-001. Each line represents a different beam energy, and the solid points are the ϵ values measured.

In order to minimize the sensitivity of the experiment to systematic uncertainties, E01-001 used a modified Rosenbluth separation technique that is dramatically less sensitive to sources of uncertainty in previous measurements. First, while the left arm was used to measure one of the high Q^2 points, the right arm took data at $Q^2 = 0.5$. Because of the small epsilon range covered in the low Q^2 measurement (Fig. 71), and the fact the the form factors are well known in this region, this data can be used as a relative luminosity monitor. The other unusual feature of E01-001 was that the elastic cross section is measured by detecting the struck proton, rather than the scattered electron. At fixed Q^2, the proton momentum is constant, so there are no momentum-dependent errors. In addition, the cross section for the proton is nearly independent of ϵ (maximum variation of ~30% for E01-001), while the electron cross section varies by a factor of 50-100. This means that the data can be taken with constant beam current and rate, reducing our sensitivity to target heating effects, dead time corrections, and rate-dependent tracking or trigger efficiencies.

The main disadvantage of detecting the proton is that the measurement becomes limited by the size of the background at large Q^2. The main background is from pion production from real photons generated as the beam passes through the target. The protons associated with the pion photoproduction can be close to the elastic peak, and even with tight cuts to minimize the background, this contribution must be modeled and subtracted. Figure 72 shows the data for the

middle Q^2 point at the most forward angle, where the background is the largest. In addition to the data, the figure shows the simulated proton elastic peak, as well as the simulation of the background from pion photoproduction. The elastic peak and background yields are normalized to the measured spectrum, and both have an additional smearing, applied to reproduce the resolution of the elastic peak. The background deviates from the calculation at lower proton momentum because only single pion production is simulated. Other backgrounds can generate protons at lower momenta and these processes are not included in the simulation. We will be able to use the coincidence runs that were taken to isolate the elastic peak from the background spectrum, in order to ensure that we have the correct shape for the background in the region where it cannot be cut away from the elastic peak.

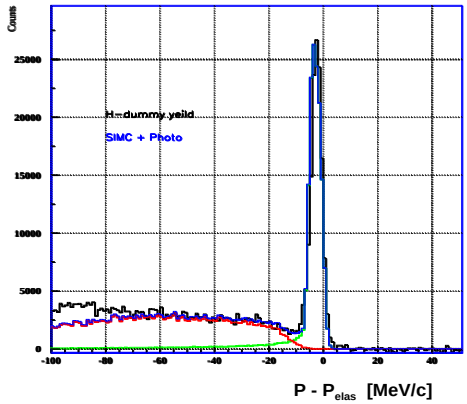

Figure 72: Proton momentum, relative to expected momentum for elastic scattering. The solid line is the data, while the green and red lines represent the simulated elastic peak and background spectrum (the blue line is the total spectrum).

The discrepancy under investigation (Fig. 70) yields a difference of ~6% in the measured cross sections and deadtime, efficiencies, radiative corrections, and background subtractions can all have effects of this size and must be included before meaningful form factor ratios can be extracted. We are currently finalizing the calibration and the efficiency measurements so that they can be implemented for the full analysis of the experiment.

4.16 Experiment E01-020

$(e, e'p)$ Studies of the Deuteron at High Q^2

W. Boeglin, M. Jones, A. Klein, P. Ulmer, E. Voutier, Spokespersons
and
the Hall A and E01-020 Collaborations

The goal of the experiment E01-020 is to provide a systematic study of the $D(e, e'p)n$ reaction down to very short distance scales. It covers kinematic settings from below to above the quasifree peak over a wide range of four-momentum transfers, Q^2 (see Fig. 73).

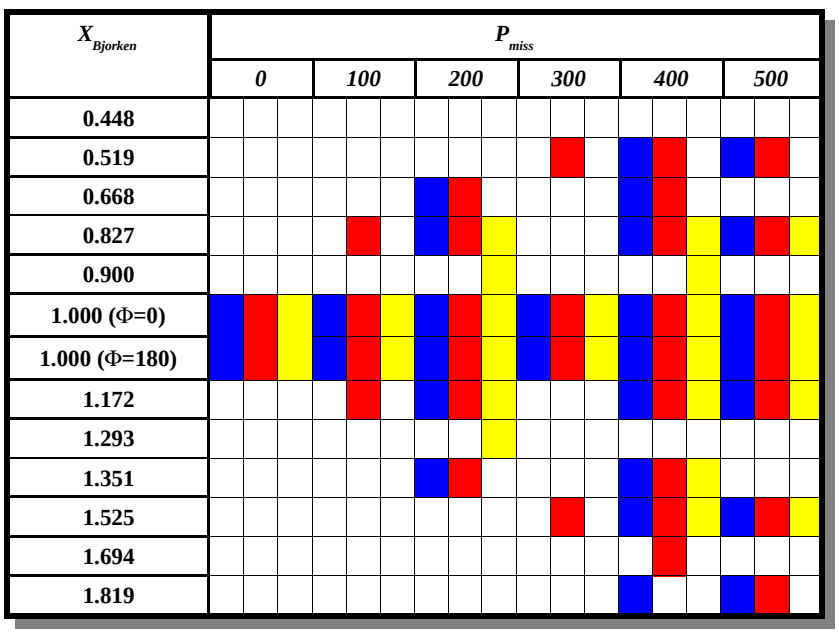

Figure 73: Kinematic setting measured; the various colors represent the Q^2 values: $Q^2 = 0.8$ $(GeV/c)^2$ (blue), $Q^2 = 2.35$ $(GeV/c)^2$ (red) and $Q^2 = 3.5$ $(GeV/c)^2$ (yellow).

For protons detected along $\vec{q}$ each kinematic setting is chosen to emphasize different aspects of the reaction mechanism. For energy transfers below the quasifree peak ($x > 1$), non-nucleonic effects (IC and MEC) are expected to be minimized since the energy transfer is relatively low. For protons detected along $\vec{q}$, FSI are also expected to be minimized since they would shift strength predominantly from high to low recoil momentum and the one-body response falls off sharply with recoil momentum. Thus, these kinematics are expected to be mainly sensitive to aspects of the deuteron's short-range structure.

By examining (for fixed Q^2 and recoil momentum) the angular distribution of neutrons in the final hadronic center-of-mass system, one can quantitatively study

FSI. Such a quantitative study will be facilitated via comparison to a generalized eikonal approximation, expected to be especially valid at high momentum transfers (and consequent high neutron-proton relative energies in the final state). The angular distribution is expected to show a large peak near 90° about the $\vec{q}$ direction. The success of theories in predicting this shape will give us confidence in correcting for FSI effects in extracting the deuteron structure. This understanding will also be useful for studies of short range correlations using $(e, e'p)$ on heavier nuclei.

Finally, a separation of the R_{LT} interference response function will be performed in quasifree kinematics over a large range of Q^2 and recoil momenta to test the validity of relativistic models. Proper treatment of relativity is essential at kinematics where we will probe the deuteron's short-range structure.

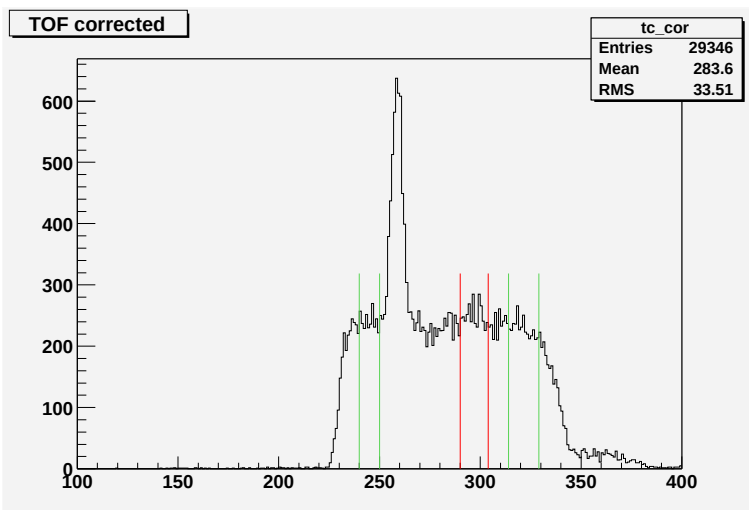

Figure 74: Time of flight spectrum for the Q1_f40l kinematics (Q^2 = 0.8 (GeV/c)^2).

During a first measurement period in May and June, 2002 we took data for $Q^2 = 0.8$ (GeV/c)^2 and $Q^2 = 2.35$ (GeV/c)^2. The detailed kinematic settings are shown in Fig. 73. We are currently working on a first pass analysis of these data.

The $Q^2 = 3.5$ (GeV/c)^2 measurements are being taken in a running period from October to November, 2002 which would complete the data taking phase of this experiment. As an illustration of the results we obtained we show the 'online' corrected coincidence time of flight spectra taken for identical values of x, p_{miss} and ϕ, the out-of-plane angle (where $x = 1$, $p_{miss} = 400$ MeV/c and $\phi = 0°$). The markers indicate the timing cuts. The central pair (red) indicate the real coincidence cut and the two pairs of markers to the left and to the right are used for accidentals subtraction. Fig. 74 shows the spectrum for $Q^2 = 0.8$ (GeV/c)^2. The large peak is an artifact of the TDC/trigger electronics.

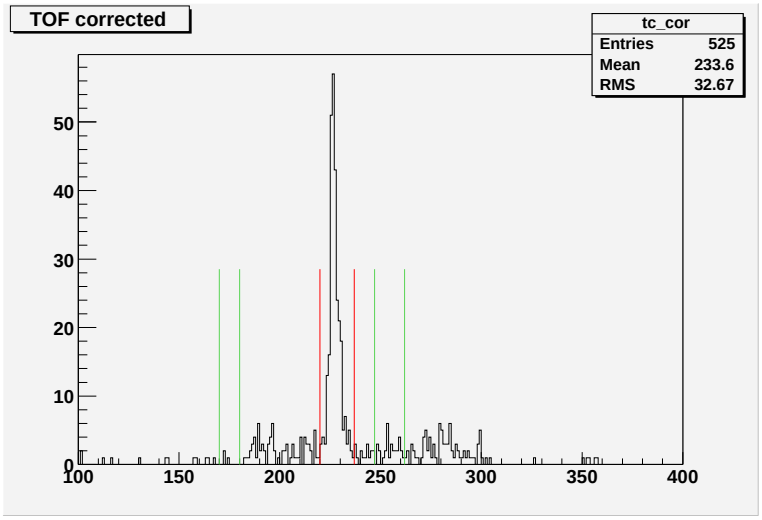

Figure 75: Time of flight spectrum for the Q3_f40l kinematics (Q^2= 3.5 $(GeV/c)^2$).

Fig. 75 is the same spectrum taken at $Q^2 = 3.5$ $(GeV/c)^2$. The two spectra nicely illustrate the effect of the accidentals reduction due to the large incident energy and the large momentum transfer.

4.17 The 12 GeV Upgrade

12 GeV Hall A Upgrade Status Report

Z.-E. Meziani
on behalf of
The Hall A Collaboration

In preparation for the Jefferson Lab 12 GeV upgrade conceptual design report (CDR), around mid-March, Jefferson Lab requested from the community involved in each Hall to prepare a CDR describing the physics driving the upgrade of each Hall, the equipment needed to achieve the physics goals set forward, and an estimate of the costs of the proposed project. Each Hall CDR was to be completed by the end of summer 2002 with the plan that selected examples from each CRD were to be included in the JLab 12 GeV upgrade CDR.

In the period between March and June of 2002, leading to the Jefferson Lab Users Meeting, three meetings (see the call for these meetings and their agendas in appendix, A, B and C) were organized and held at Jefferson Lab. These meetings helped outline the physics ideas and identify the required equipment to perform the key experiments which are expected to drive the physics program. The aim was to motivate and define the needed experimental equipment beyond what's already available in the Hall, and produce a CDR for Hall A.

The meetings were well attended and many physics ideas and their corresponding proposed measurements were discussed during the physics sessions. The participants confirmed the need for a medium acceptance spectrometer (MAD) and were very active in the discussions to define the required experimental equipment. A GEANT simulation of the spectrometer led to an optimized design of the spectrometer for background reduction compared to earlier design versions. Then during the intrumentation sessions, a serious effort went into the design of the detector packages to be used in MAD with the criteria to match the physics requirements of the proposed experiments.

During the annual users meeting held in June, a last Hall A workshop was held as a parallel session of the main meeting and a summary of the Hall A physics and instrumentation outcome was presented in the plenary session summary. The articulated physics goals in the presentation are summarized as,

1. Close a chapter in nucleon valence quark structure study with precision inclusive and semi-inclusive reactions.

2. Make a significant contribution to the study of the Generalized Parton Distributions (GPDs) with Real Compton Scattering (RCS), Deep Virtual Compton Scattering (DVCS) and form factor measurements;

3. Extensively enhance our understanding in the transition region (between perturbative QCD and strong-QCD).

4. Explore the hadron structure in the nuclear medium.

5. Search for new physics with selected precision tests of the electroweak standard model.

Writing assignments were agreed upon early in the process (see Appendix D), thus the next three months following the last workshop a complete version of the CDR was produced and made available on September 8, 2002. Details of the physics program and its corresponding instrumentation can be found in the CDR [46]. The next step in the process of the 12 HeV upgrade is a review of the proposed physics and instrumentation in January by the Program Advisory Committee (PAC). The collaboration is already preparing for it.

Finally on behalf of our collaboration I would like to thank all the contributors to the CDR and Jian Ping Chen for an outstanding job of organizing and leading the effort in such a short notice.

Appendix A

From: Jian-Ping Chen <jpchenJLAB.ORG>
Organization: Jefferson Lab
To: <hallaJLAB.ORG> and other recipients
Date: Tuesday, March 19, 2002 2:27 PM
Subject: Program for March22 workshop on Hall A 12 GeV upgrade (Corrected)
Dear Colleague,
Please find below a program for the March 22 workshop on Hall A 12 GeV upgrade. The physics topics will include Inclusive Scattering, Semi-Inclusive Reactions, Exclusive Reactions, Nuclear Medium and Charm Production. To fit all the physics discussions in one morning, all talks will be short. Each topic will have an overview/summary talk (15 minutes) follow by individual experimental talk (5 minutes), which should have what are the planned measurements with projected results and requirements on instrumentation. There will be some time for discussion at the end of each topic.
The equipment currently under discussion are a Medium Acceptance Device (MAD) with associate detectors and a calorimeter. You are invited to participate in the workshop and to contribute to the discussions and the work towards a Conceptual Design Report (to be completed by the end of the summer).

Looking forward to seeing you at the workshop.

Jian-ping

Program for the Hall A 12 GeV Upgrade Workshop
L102-104, CEBAF Center, Jefferson Lab
Friday March 22, 2002

Morning: Physics and Requirements

8:30	Welcome and General Remark	C. de Jager
8:40	Inclusive Structure Functions	W. Melnitchouk
8:55	A1p at high x	G. Warren
	d2n(g2n)	T. Averett
	Spin Structure at High s	A. Deur
	Spin Duality	N. Liyanage
9:15	Discussion	
9:30	Semi-inclusive Reactions	A. Afanasev
9:45	Kinematics/pion prod/delta_d	X. Jiang
	d_bar/u_bar	H. Gao
	Lambda pol./Transversity*	J. C. Peng
	Pion Structure Function	K. Wijesooriya
10:05	Discussion	
10:20	break	
10:40	Exclusive Reactions	C. Hyde-Wright
10:55	RCS	B. Wojtsekhowski
	Photoproduction	X. Jiang
	Gep/Gmp at high Q2	A. Saha
	Gen at high Q2	B. Reitz
11:15	Discussion	
11:30	Nuclear Medium at high Q2	M. Sargisian
11:45	x>1	W. Bertozzi
	Hadronization in Nuclear Medium	K. Wang
	Pion Photoproduction	H. Gao
	Color Transparency	A. Saha
12:05	Discussion	
12:20	Charm threshold prod	K. Griffioen/E. Chudakov
12:40	Discussion	
12:50	Lunch	

Afternoon: Instrumentation

2:00	Discussion on requirements	Z. Meziani/All
2:30	MAD design	P. Brindza
2:45	MAD optics	J. LeRose
3:00	MAD simulations	J. LeRose/Z. Meziani/A. Gasparian
3:30	MAD detectors	
	Scintillators	T. Averett
	Drift Chambers	N. Liyanage
	Shower Counters	A. Gasparian/W. Bertozzi
	Gas Cerenkov Counter	Z. Meziani
	Aerogel Cerenkov Counter	H. Gao
	Hadron PID/RICH	F. Galibaldi
	Muon Detector	E. Chudakov
	DAQ system	
4:45	break	
5:05	Calorimeter	C. Hyde-Wright
5:20	Discussion,distribution of tasks;forming working groups	
6:00	Adjourn	

Appendix B

From: Jian-Ping Chen <jpchenJLAB.ORG>
Organization: Jefferson Lab
To: <halla_12gevJLAB.ORG>
Date: Thursday, May 9, 2002 7:18 PM
Subject: Program for May 13 workshop on Hall A 12 GeV upgrade
Dear Colleague,
Please find below the program for the May 13 workshop on Hall A 12 GeV upgrade.

The physics discussion will be in the morning and instrumentation discussion in the afternoon. The physics topics will include Inclusive Scattering, Semi-inclusive Reactions, Exclusive Reactions, Nuclear Medium and Charm Production. Each topic will have a summary talk and a theory talk as well followed by discussions. All the physics experiments will be written in a Hall A conceptual design report (CDR). Then selected examples will be included in the JLab CDR. The new equipment currently under discussion are a Medium Acceptance Device (MAD) with associate detectors, a calorimeter, and possible upgrade of a beam polarimetry.

You are invited to participate in the workshop and contribute to the discussions and the work towards a Conceptual Design Report (to be completed by the end of the summer).

Hope to see you then.

Jian-ping

Hall A 12 GeV Upgrade Workshop
L102-104, CEBAF Center, Jefferson Lab
Monday, May 13, 2002

Morning: Physics Discussion

8:30	Welcome and General Remark	C. de Jager
8:45	Highlight of Physics with 12 GeV Upgrade	X. Ji
9:00	Inclusive Structure Functions (Theory)	W. Melnitchouk
9:15	Inclusive Structure Functions	W. Melnitchouk
9:30	Discussion	
9:45	DIS-Parity	
9:55	Semi-inclusive Reactions (Theory)	A. Afanasev
10:10	Semi-inclusive reactions	H.Gao
10:30	Discussion	
10:45	break	
11:00	Exclusive Reactions	C. Hyde-Wright
11:20	Discussion	
11:35	NuclearMedium at high Q2	D. Higinbotham
11:55	Discussion	
12:10	Charm threshold prod/Discussion	E. Chudakov
12:30	Lunch	

Afternoon: Instrumentation

1:30	MAD design	P. Brindza
2:00	MAD optics	J. LeRose
2:15	MAD simulations	O. Hansen
2:30	MAD detectors	
	Overview	B. Wojtsekhowski
	Scintillators	T. Averett
	Drift Chambers	N. Liyanage
	Shower Counters	E. Chudakov
	Gas Cerenkov Counter	Z. Meziani
	Hadron PID	F. Garibaldi

	Aerogel Cerenkov Counter	H. Gao
	FPP	S. Nanda
	DAQ system	B. Reitz
4:10	Beamline and Polarimeters	A.Saha/E.Chudakov/S.Nanda
4:30	break	
4:45	Calorimeter	C. Hyde-Wright
5:05	Discussion	
6:00	Adjourn	

Appendix C

From: Jian-Ping Chen <jpchen@JLAB.ORG>
Organization: Jefferson Lab
To: <halla_12gev@JLAB.ORG>
Date: Monday, June 3, 2002 3:41 PM
Subject: preliminary agenda for the Hall A parallel session on 12 GeV upgrade at the User meeting

Dear Colleague,
Please find below a preliminary program for the Hall A parallel session on 12 GeV upgrade on June 11 during the user meeting. There will be summary talks for each physics topic, followed by discussions. At the end of the morning session, there will be theory summary talks with discussion.
The discussion will be focussed on selecting highlights to be included in the JLab CDR, and the equipment needed to accomplish the physics goal. The new equipment currently under discussion are a Medium Acceptance Device (MAD) with associated detectors, a calorimeter, and upgrade of beam polarimetries.
You are invited to participate in the workshop and contribute to the discussions and the work towards a Conceptual Design Report (to be completed by the end of the summer). If you see any changes needed in the agenda, or you have any suggestions, please let me know. For the ones your name is on the program, please let me know ASAP if you can not make it or would like to have somebody else to give the talk.

Thanks.

Jian-ping

Users Meeting Hall A parallel session for 12 GeV Upgrade
L102-104, CEBAF Center, Jefferson Lab
Tuesday June 11, 2002,

Morning: Physics Discussion

8:30	Welcome and General Remark	C. de Jager
8:45	Inclusive Structure Functions	J. Gomez
9:00	Discussion	
9:20	Semi-inclusive Reactions	H. Gao
9:35	Discussion	
9:55	Exclusive Reactions	C. Hyde-Wright
10:10	Discussion	

10:30 Break

10:50	Nuclear Medium at high Q2	D. Higinbotham
11:05	Discussion	
11:25	Charm production	E. Chudakov
11:30	Discussion	
11:40	Theory Summary and Discussion	Afanasev/Carlson/Melnitchouk...
12:10	Discussion	

12:30 Lunch

Afternoon: Instrumentation

1:30	MAD design update	P. Brindza
1:50	MAD optics update	J. LeRose
2:05	GEANT and background	E. Chudakov
2:20	MAD simulations	O. Hansen
2:30	MAD detector update	
	Overview	B. Wojtsekhowski
	Scintillators	T. Averett
	Drift Chambers	N. Liyanage
	Shower Counters	E. Chudakov
	Gas Cerenkov Counter	S. Choi
	DAQ system	B. Reitz

3:30	Break	
3:50	MAD hadron detectors update	
	Hadron PID	F. Garibaldi
	Aerogel Cerenkov Counter	L. Zhu
	FPP	S.Nanda
4:30	Polarimeters update	S.Nanda
4:50	Calorimeter update	C. Hyde-Wright
5:05	Discussion	
6:00	Adjourn	

Appendix D

From: Jian-Ping Chen <jpchenJLAB.ORG>
Organization: Jefferson Lab
To: <halla_12gevJLAB.ORG>
Date: Monday, May 20, 2002 6:50 PM
Subject: CDR write-up for Hall A 12 GeV upgrade

Dear Colleague,

The 2nd workshop on Hall A 12 GeV upgrade on May 13th was successful and thanks to all of your hard work, a lot of progress were made for the Hall A upgrade CDR. Next step, we would like to have the revised version incorporate all the comments and feedback to be completed before the June User meeting. To accomplish that, we ask all the section coordinators to send in the revised sections by May 29 (Wed.) so that we will have about a week time to edit all sections. Each section coordinator should coordinate with all the contributors and section editors to complete the changes in time. All contributors are strongly encouraged to make your changes and submit to your section coordinator ASAP to give your section editor and coordinator time to incorporate all the changes. Please start with the current version on the web site: http://hallaweb.jlab.org/12GeV/cdr/Sections/.
Attached is a list of coordinators/editors (for the ones whose name appear first time, please let me know if there is any difficult for you).
Suggestions and comments are appreciated.

Thanks for your contributions and efforts.

Jian-ping Chen

A. Introduction and Executive Summary Chapters, writing and editing: Z. Meziani and X. Ji
Hopefully will have a edited version of
introduction and first draft of executive summary

B. Physics Chapter:

1) Inclusive, coordinator: J. Gomez; editors: W. Melnitchouk, X. Ji;
(Note: I'll suggest to have DIS parity to be included in this section);
2) Semi-inclusive, coordinator: H. Gao; editors: A. Afanasev, W. Melnitchouk, C, Carlson;
3) Exclusive, coordinator: C. Hyder-Wright; editor: A.Radyushkin;
4) Nuclei, coordinator: D. Higinbotham; editors: M. Sargisian, F. Gross;
5) Charm: coordinator: E. Chudakov; editor:

Physics overall coordinator and editors: (Z. Meziani, F. Gross, X. Ji and A. Radyushkin)
you may start to edit the physics chapter now already, but will get a newer version by May 31.

C. Instrumentation chapter:

1) Physics Requirements Lead to Instrumentation (especially MAD), writing: J. P. Chen;
editing: D. Higinbotham, Z. Meziani;

2) MAD Spectrometer, writing: P. Brindza; editing: J. LeRose;
3) MAD Optics, writing: J. LeRose; editing: ?
4) MAD simulation, coordinating, writing overview and editing: O. Hansen;
5) MAD detectors, coordinating , writing overview and editing: B. Wojtsekhowski;
checking: E. Chudakov, J. Segal;
6) DAQ System for MAD, writing and checking: R. Michaels and B. Reitz;
7) Calorimeter: writing: C. Hyde-Wright; checking: S. Nanda;
8) Beamline, coordinating and editing: A. Saha;
Instrumentation overall coordinating and editing: D.Higinbotham.

Overall editing: K. de Jager and J. P. Chen.

References

5 References

[1] M. Baylac *et al.*, Phys. Lett. **B539**, 8-12 (2002).

[2] Hall A Status Report, Edited by A. Sarty and K. de Jager, March 2002. S. Escoffier, Ph.D. Thesis, Université Paris Sud, Orsay (2002).

[3] The Hall A 12 GeV Upgrade, Conceptual Design Report, (2002).

[4] `http://hallaweb.jlab.org/equipment/targets/cryotargets/`.

[5] R. Suleiman, HAPPEXII internal report.

[6] M. Seely, private communication.

[7] Technical notes in `http://www.jlab.org/e94010/`; `http://hallaweb.jlab.org/physics/experiments/he3/`.

[8] JLab Experiment E94-010, Spokespersons, Z.-E. Meziani, G. Cates and J.-P. Chen; M. Amarian *et al.*, accepted for publication in Phys. Rev. Lett. (2002) Nucl-ex/0205020.

[9] W. Xu *et al.*, Phys. Rev. Lett. 85, 2900 (2000); F. Xiong *et al.*, Phys. Rev. Lett. 87, 242501 (2001).

[10] JLab Experiment E99-117, Spokespersons, J.-P. Chen, Z.-E. Meziani and P. Souder; `http://hallaweb.jlab.org/physics/experiments/he3/A1n/index.html`.

[11] JLab Experiment E97-103, Spokespersons, T. Averett and W. Korsch; `http://hallaweb.jlab.org/physics/experiments/he3/g2/temp/`

[12] P. Ulmer, private communication.

[13] N. Liyanage, private communication

[14] G. Chang, GEANT model HAGMC.

[15] A. Saha, contact person, Study of the Quasi elastic (e,e'p) reaction in ^{16}O at High Recoil Momentum, JLab experiment E89-003.

[16] P. Markowitz, contact person, Electro production of Kaons up to $Q^2 = 3$ $(\mathrm{GeV}/c)^2$, JLab experiment E98-108.

[17] E.S. Smith *et al.*, Nucl. Instrum. Methods **A 432**, 265 (1999).

[18] B.D. Anderson *et al.*, "Basic Instrumentation for Hall A at Jefferson Lab", to be submitted to Nucl. Instrum. Methods.

[19] ELJEN technology, `http://www.eljentechnology.com`.

[20] PHOTONIS, `http://www.photonis.com`.

[21] G. Ron, "Efficient light collection in scintillator counters", Hall A Internal Report, August, 2001.

[22] `http://hallaweb.jlab.org/news/minutes/transferfuncs.html`

[23] `http://hallaweb.jlab.org/root/`

[24] ESPACE CVS repository, accessible via SSH (JLab CUE account required), `:ext:cvs.jlab.org:/group/halla/analysis/cvs`, module `espace`.

[25] P.E. Ulmer, computer program MCEEP, *Monte Carlo for* $(e, e'p)$ *Experiments*, JLAB Technical Note # 91-101 (1991).

[26] M. Bertz, COSY INFINITY version 7, Michigan State University NSCL Technical Report MSUCL-977, (1995).

[27] http://www.physics.odu.edu/~ ulmer/mceep/mceep.html.
[28] http://hallaweb.jlab.org/news/minutes/tranferfuncs.html.
[29] P.E. Ulmer *et al.*, Phys. Rev. Lett. **89**, 062301-1 (2002).
[30] V.L. Rvachev, T.I. Sheiko, V. Shapiro and I. Tsukanov, Comp. Mech. **25**, 305 (2000).
[31] E. Schulte *et al.*, Phys. Rev. **C66**, 042201(R) (2002); E. Schulte, Ph.D. Thesis, University of Illinois, Urbana-Champaign (2002).
[32] JLab Experiment E01-109, C. F. Perdrisat, V. Punjabi, M. K. Jones and E. Brash.
[33] L. S. Azghirey *et al.*, to be published in the proceedings of SPIN 2002 at BNL.
[34] A. V. Radyushkin, Phys. Rev. **D58**, 114008 (1998).
[35] E. Chudakov *et al.*, Study of Hall A Photon Spectrometer, Hall A internal report, (1998).
[36] JLab Experiment E99-114, Spokespersons, C. Hyde-Wright, A. Nathan and B. Wojtsekhowski.
[37] F. Garibaldi *et al.*, "A Proximity Focusing RICH Detector for Kaon Physics at Jefferson Lab Hall A", Proceedings of RICH2002 Workshop, Pylos (Greece), June 2002, to be published in NIM.
[38] Hall A Report 2001.
[39] F. Cusanno *et al.*, "Quantum Efficiency Measurement System for Large Area CsI photodetectors", Proceedings of RICH2002 Workshop, Pylos (Greece), June 2002, to be published in NIM.
[40] ALICE Collaboration, Technical Design Report of the High Momentum Particle Identification Detector, CERN/LHCC98-19, ALICE TDR1, August 1998.
[41] JLab Experiment E02-013, Spokespersons, G. Cates, K. McCormick, B. Reitz and B. Wojtsekhowsk.
[42] JLab Experiment E02-108, Spokespersons, W. Bertozzi, D. Higinbotham, B. Norum, S. Širca and Z.-L. Zhou.
[43] JLab Experiment E02-101, Spokespersons, W. Bertozzi, B. Norum, T. Tamae and K. Wang.
[44] JLab Experiment E01-015, Spokespersons, W. Bertozzi, E. Piasetzky, J. Watson and S. Wood.
[45] JLab Experiment E01-014, Spokespersons, J. Annand, D. Higinbotham, R. Lindgren and V. Nelyubin.
[46] Hall A 12 GeV Upgrade Conceptual Design Report, September 8, 2002; `http://hallaweb.jlab.org/12GeV/`.
[47] `http://hallaweb.jlab.org/news/minutes/mad`
[48] S. Kowalski and R. Madey, cospokespersons, "The Electric Form Factor of the Neutron from the ^{2}H$(\vec{e}, e'\vec{n})$p Reaction," JLab Experiment No. E93-038.
[49] B. Milbrath *et al.*., Phys. Rev. Lett. **80**, 452 (1998); erratum, Phys. Rev. Lett. **82**, 2221 (1999).

[50] H. Arenhövel (private communication).
[51] R. Machleidt, K. Holinde and Ch. Elster, Phys. Rep. **149**, 1 (1987).
[52] E. Borie and D. Drechsel, Nucl. Phys. **A167**, 369 (1971).
[53] N. Isgur, G. Karl, and R. Koniuk, Phys. Rev. **D 25**, 2394 (1982).
[54] A.J. Buchmann, arXiv:hep-ph/9909385 (unpublished).
[55] M. Fiolhais, G. Golli, and S. Sirca, Phys. Lett. **B373**, 229 (1996).
[56] S.S. Kamalov and S.N. Yang, Phys. Rev. Lett. **83**, 4494 (1999).
[57] D. Drechsel, O. Hanstein, S.S. Kamalov, L. Tiator and S.N. Yang, Nucl. Phys. **A645**, 145 (1999); `http://www.kph.uni-mainz.de/MAID`.
[58] R.A. Arndt, W.J. Briscoe, R.L. Workman and I.I. Strakovsky, `http://www.gwdac.phys.gwu.edu`.
[59] S.S. Kamalov, S.N. Yang, D. Drechsel, O. Hanstein, and L. Tiator, Phys. Rev. **C 64**, 032201(R) (2001).
[60] D.H. Lu, K. Tsushima, A.W. Thomas, A.G. Williams and K. Saito, Phys. Lett. **B417** (1998) 217; Phys. Rev. C **60** (1999) 068201.
[61] J. Jourdan, Phys. Lett. **B353** (1995) 189.
[62] J. Morgenstern and Z.-E. Meziani, Phys. Lett. **B515** (2001) 269.
[63] J. Carlson, J. Jourdan, R. Schiavilla, and I. Sick, to be submitted.
[64] I. Sick, Comm. Nucl. Part. Phys. **18** (1988) 109.
[65] T.E.O. Ericson and A. Richter, Phys. Lett. **B183** (1987) 249.
[66] M.R. Frank, B.K. Jennings, and G.A. Miller, Phys. Rev. C **54** (1996) 920.
[67] M.K. Jones *et al.*, Phys. Rev. Lett. **84** (2000) 1389.
[68] O. Gayou *et al.*, Phys. Rev. C **64** (2001) 038202.
[69] S. Dieterich *et al.*, Phys. Lett. **B500** (2001) 47.
[70] J.M. Udias *et al.*, Phys. Rev. Lett. **83** (1991) 5451; J.A. Caballero, T.W. Donnelly, E. Moya de Guerra, and J.M. Udias, Nucl. Phys. **A632** (1998) 323; J.M. Udias and J.R. Vignote, Phys. Rev. C **62** (2000) 034302.
[71] J.-M. Laget, Nucl. Phys. **A579** (1994) 333.
[72] E93-050 web page: `hallaweb.jlab.org/physics/experiments/E93-050/vcs.html`
[73] P. A. Guichon, G. Q. Liu and A. W. Thomas, Nucl. Phys. **A591**, 606 (1995); P.A. Guichon, and M. Vanderhaeghen Prog. Part. Nucl. Phys. **41**, 125 (1998).
[74] VCSSIM code, L. Van Hoorebeke, Gent University, Gent, Belgium.
[75] M. Vanderhaeghen *et al.*, Phys. Rev. **C62**, 025501 (2000)
[76] B. Pasquini *et al.*, Eur. Phys. J. A **11**, 185 (2001) [arXiv:hep-ph/0102335].
[77] V. Olmos de Leon *et al.*, Eur. Phys. J. A **10**, 207 (2001).
[78] J. Roche *et al.*, [VCS Collaboration], Phys. Rev. Lett. **85**, 708 (2000)
[79] J. Shaw, R. Miskimen, co-spokespersons, M.I.T.-Bates experiment 97-03.
[80] Thomas R. Hemmert, Phys Rev **D 62**, 014013 (2000).
[81] M. Amarian *et al.*, accepted by Phys. Rev. Lett.
[82] D. Drechsel, S. Kamalov and L. Tiator, Phys. Rev. D **63**, 114010 (2001).
[83] C.W. Kao, T. Spitzenberg and M. Vanderhaeghen, `hep-ph/0209241` (2002).

[84] JLab Experiment E01-012, Spaokespersons, J.-P. Chen, S. Choi and N. Liyanage.
[85] SLAC E143 Collaboration, K. Abe *et al.*, Phys. Rev. D **58**, 112003 (1998).
[86] E142, P. L. Anthony *et al.*, Phys. Rev. Lett. **71**, 959 (1993); Phys. Rev. **D54**, 6620 (1996).
[87] E154, K. Abe *et al.*, Phys. Rev. Lett. **79**, 26 (1997).
[88] HERMES Collaboration, K. Ackerstaff *et. al.*, Phys. Lett. B **444**, 531 (1998).
[89] V. Bernard, N. Kaiser and Ulf-G. Meissner, Phys. Rev. D **48**, 3062 (2993); Int. J. Mod. Phys. E **4** 1 (2000).
[90] V. Bernard, T. Hemmert and Ulf-G. Meissner, Phys. Lett. B **545**, 105 (2002).
[91] X. Ji, C. Kao and and J. Osborne, Phys. Lett. B**472**, 1 (2000).
[92] X. Ji and J. Osborne, J. Phys. G **27**, 127 (2001).
[93] J. Soffer and O. V. Teryaev, Phys. Lett. B **545**, 323 (2002).
[94] V. D. Burkert and B. L. Ioffe, Phys. Lett. **B296**, 223 (1992); CEBAF Preprint PR-93-034.
[95] H. Burkhardt and W. N. Cottingham, Ann. Phys. **56**, 453 (1970).
[96] S. A. Larin and J. A. M. Vermaseren, Phys. Lett. **B259**, 345 (1991) and references therein; S. A. Larin, Phys. Lett. **B334**, 192 (1994).
[97] Z. P. Li and Zh. Li, Phys. Rev. **D50**, 3119 (1994).
[98] P. L. Anthony *et al.*, `hep-ph/0204028` (2002).
[99] S.J. Brodsky and G.R. Farrar, Phys. Rev. Lett. **31**, 1153 (1973); Phys. Rev. D **11**, 1309 (1975); V. Matveev *et al.*, Nuovo Cimento Lett. **7**, 719 (1973).
[100] H. Xiang, "Measurement of π^- and π^+ Photoproduction in Deuterium at Large Momentum Transfer for E=1.7 $\sim$ 5.6 GeV", Proceedings of QNP2002, (2002).
[101] S.J. Brodsky, C.E. Carlson, and H. Lipkin, Phys. Rev. D **20**, 2278 (1979).
[102] J.P. Ralston and B. Pire, Phys. Rev. Lett. **65**, 2343 (1990); J.P. Ralston and B. Pire, Phys. Rev. Lett. **61**, 1823 (1988).
[103] Z. Bar-Yam *et al.*, Phys. Rev. Lett. **19**, 40 (1967).
[104] R.L. Anderson *et al.*, Phys. Rev. D **14**, 679 (1976).
[105] H.-J. Besch *et al.*, Z. Phys. C **16**, 1 (1982).
[106] H.W. Huang, private communication; H.W. Huang and P. Kroll, Eur. Phys. J. C **17**, 423 (2000); A. Afanasev, C.E. Carlson, and C. Wahlquist, Phys. Lett. B **398**, 393 (1997).
[107] S.J. Brodsky and F.F. de Teramond, Phys. Rev. lett. **60**, 1924 (1988).
[108] R.L. Jaffe and X. Ji, Phys. Rev. **D43**, 724 (1991).
[109] S. Wandzura and F. Wilczek, Phys. Lett. **B72**, 195 (1977).
[110] P.L. Anthony *et al.*, Phys. Lett. **B493**, 19 (2000).
[111] M. Gluck, E. Reya, M. Stratmann, and W. Vogelsang, Phys. Rev. **D63**, 094005 (2001).
[112] J. Blumlein and H. Bottcher, Nuc. Phys. **B636**, 225 (2002).
[113] Bockhorst *et al.*, Zeit. Phys. **C 63**, 37 (1994).
[114] M.A. Shupe *et al.*, Phys. Rev. **D 19**, (1979) 1929.

[115] T. Brooks and L. Dixon, Phys. Rev. **D 62**, (2000) 114021.
[116] H.W. Huang, P. Kroll, T. Morii, Eur. Phys. J. **C 23**, (2002) 301.
[117] K. Wijesooriya *et al.*, Phys. Rev. Lett. **86**, 2975 (2001).
[118] A. Saha, W. Bertozzi, L.B. Weinstein, and K.G. Fissum, Experimental Proposal E00-102, Jefferson Laboratory (2000).
[119] J. Gao *et al.*, Phys. Rev. Lett. **84**, 3265 (2000).
[120] N. Liyanage *et al.*, Phys. Rev. Lett. **86**, 5670 (2001).
[121] F. Garibaldi *et al.*, Nucl. Instr. Meth. in Phys. Res. **A 314**, 1 (1992).
[122] E. Cisbani *et al.*, *A waterfall target system for Hall A at Jefferson Lab*, INFN/ISS **97/04** (1997).
[123] O. Gayou *et al.*, Phys. Rev. Lett. **88**, 092301 (2002).
[124] J. Arrington, arXiv:hep-ph/0209243.
[125] R. C. Walker *et al.*, Phys. Rev. **D49**, 5671 (1994).

Hall A Collaboration Member List

6 Hall A Collaboration Member List

Bryon Anderson	*Kent State University*
Mattias Andersson	*University of Lund*
Konrad A. Aniol	*California State University*
John Annand	*University of Glasgow*
David S. Armstrong	*College of William and Mary*
John Arrington	*Argonne National Laboratory*
Todd Averett	*College of William and Mary*
Maud Baylac	*Jefferson Laboratory*
Elizabeth Beise	*University of Maryland*
Fatiha Benmokhtar	*Rutgers University*
Jacques Berthot	*Université Blaise Pascal, Clermont-Ferrand*
Pierre Bertin	*Université Blaise Pascal, Clermont-Ferrand*
Bill Bertozzi	*Massachusetts Institute of Technology*
Louis Bimbot	*Institut de Physique Nucléaire, Orsay*
Tim Black	*Massachusetts Institute of Technology*
Werner Boeglin	*Florida International University*
Ed Brash	*University of Regina*
Vincent Breton	*Université Blaise Pascal, Clermont-Ferrand*
Herbert Breuer	*University of Maryland*
Etienne Burtin	*DAPNIA/SPhN, CEA, Saclay*
John Calarco	*University of New Hampshire*
Alexandre Camsonne	*Université Blaise Pascal, Clermont-Ferrand*
Larry Cardman	*Jefferson Laboratory*
Gordon D. Cates	*University of Virginia*
Christian Cavata	*DAPNIA/SPhN, CEA, Saclay*
Zengwei Chai	*Massachusetts Institute of Technology*
George Chang	*University of Maryland*
Ting Chang	*University of Illinois*
Nicholas Chant	*University of Maryland*
Jian-Ping Chen	*Jefferson Laboratory*
Seonho Choi	*Temple University*
Eugene Chudakov	*Jefferson Laboratory*
Steve Churchwell	*Duke University*
Evaristo Cisbani	*INFN/Sezione Sanità*
Leon Cole	*Hampton University*
Marius Coman	*Florida International University*
Francesco Cusanno	*INFN/Sezione Sanità*
Dan Dale	*University of Kentucky*
Nathalie Degrande	*Gent State University*

Raffaele De Leo	*INFN/Sezione Bari*
Alexandre Deur	*University of Virginia*
Nicole d'Hose	*DAPNIA/SPhN, CEA, Saclay*
Sonja Dieterich	*Rutgers University*
Rachele di Salvo	*INFN/Sezione Roma2*
Pibero Djawotho	*College of William and Mary*
Frank Dohrmann	*Argonne National Laboratory*
Jean-Eric Ducret	*DAPNIA/SPhN, CEA, Saclay*
Dipangkar Dutta	*Massachusetts Institute of Technology*
Kim Egiyan	*Yerevan Physics Institute*
Martin B. Epstein	*California State University*
Mike Finn	*College of William and Mary*
Kevin Fissum	*University of Lund*
Helene Fonvieille	*Université Blaise Pascal, Clermont-Ferrand*
Bernard Frois	*DAPNIA/SPhN, CEA, Saclay*
Salvatore Frullani	*INFN/Sezione Sanità*
Haiyan Gao	*Duke University*
Franco Garibaldi	*INFN/Sezione Sanità*
Ashot Gasparian	*Hampton University*
Olivier Gayou	*Massachusetts Institute of Technology*
Shalev Gilad	*Massachusetts Institute of Technology*
Ron Gilman	*Rutgers University*
Alexander Glamazdin	*Kharkov Institute of Physics and Technology*
Charles Glashausser	*Rutgers University*
Javier Gomez	*Jefferson Laboratory*
Victor Gorbenko	*Kharkov Institute of Physics and Technology*
Tim Gorringe	*University of Kentucky*
Keith Griffioen	*College of William and Mary*
David Hamilton	*University of Glasgow*
Ole Hansen	*Jefferson Laboratory*
David Hayes	*Old Dominion University*
Bill Hersman	*University of New Hampshire*
Doug Higinbotham	*Jefferson Laboratory*
Wendy Hinton	*Old Dominion University*
Richard Holmes	*Syracuse University*
Harry Holmgren	*University of Maryland*
Maurik Holtrop	*University of New Hampshire*
Edik Hovhannisyan	*Yerevan Physics Institute*
Calvin Howell	*Duke University*
Garth Huber	*University of Regina*
Charles Hyde-Wright	*Old Dominion University*

Hassan Ibrahim	*Old Dominion University*
Sebastian Incerti	*Temple University*
Mauro Iodice	*INFN/Sezione Sanità*
Riccardo Iommi	*INFN/Sezione Sanità*
Dave Ireland	*University of Glasgow*
Kees de Jager	*Jefferson Laboratory*
Stephanie Jaminion	*Université Blaise Pascal, Clermont-Ferrand*
Steffen Jensen	*California Institute of Technology*
Xiangdong Jiang	*Rutgers University*
Cathleen Jones	*California Institute of Technology*
Mark K. Jones	*Jefferson Laboratory*
Seigo Kato	*Yamagata University*
Mina Katramatou	*Kent State University*
James Kellie	*University of Glasgow*
James Kelly	*University of Maryland*
Sophie Kerhoas	*DAPNIA/SPhN, CEA, Saclay*
Armen Ketikyan	*Yerevan Physics Institute*
Kouichi Kino	*Tohoku University*
Ioannis Kominis	*Princeton University*
Wolfgang Korsch	*University of Kentucky*
Serge Kox	*Institut des Sciences Nucléaires, Grenoble*
Alexander Kozlov	*University of Regina*
Kevin Kramer	*College of William and Mary*
Laird Kramer	*Florida International University*
Krishna S. Kumar	*University of Massachusetts*
Gerfried Kumbartzki	*Rutgers University*
Geraud Lavessiere	*Université Blaise Pascal, Clermont-Ferrand*
John LeRose	*Jefferson Laboratory*
Mark Leuschner	*University of New Hampshire*
David Lhuillier	*DAPNIA/SPhN, CEA, Saclay*
Richard Lindgren	*University of Virginia*
Ken Livingston	*University of Glasgow*
Nilanga Liyanage	*University of Virginia*
George Lolos	*University of Regina*
Robert Lourie	*Renaissance Technology*
Richard Madey	*Kent State University*
Kazushige Maeda	*Tohoku University*
Mark Manley	*Kent State University*
Demetrius Margaziotis	*California State University*
Pete Markowitz	*Florida International University*
Jacques Marroncle	*DAPNIA/SPhN, CEA, Saclay*

Jacques Martino	*SUBATECH, IN2P3, Nantes*
Samvel Mayilyan	*Yerevan Physics Institute*
Kathy McCormick	*Kent State University*
David Meekins	*Jefferson Laboratory*
Zein-Eddine Meziani	*Temple University*
Bob Michaels	*Jefferson Laboratory*
Brian Milbrath	*Eastern Kentucky University*
Wilson Miller	*University of Virginia*
Joseph Mitchell	*Renaissance Technology*
Bryan Moffit	*College of William and Mary*
Peter Monaghan	*Massachusetts Institute of Technology*
Jean Mougey	*Institut des Sciences Nucléaires, Grenoble*
Sirish Nanda	*Jefferson Laboratory*
Alan Nathan	*University of Illinois*
Vladimir Nelyubin	*Gatchina*
Damien Neyret	*DAPNIA/SPhN, CEA, Saclay*
Dima Nikolenko	*Budker Institute of Nuclear Physics*
Blaine Norum	*University of Virginia*
Zisis Papandreou	*University of Regina*
Kent Paschke	*University of Massachusetts*
Emilie Penel-Notarris	*Institut des Sciences Nucléaires, Grenoble*
Lubomir Penchev	*College of William and Mary*
Charles Perdrisat	*College of William and Mary*
Gerassimos G. Petratos	*Kent State University*
Artush Petrosyan	*Yerevan Physics Institute*
Eli Piasezky	*Tel Aviv University*
Stephane Platchkov	*DAPNIA/SPhN, CEA, Saclay*
Roman Pomatsalyuk	*Kharkov Institute of Physics and Technology*
Vina Punjabi	*Norfolk State University*
Thierry Pussieux	*DAPNIA/SPhN, CEA, Saclay*
Issam Qattan	*North-Western University*
Gilles Quéméner	*Institut des Sciences Nucléaires, Grenoble*
Igor Rachek	*Budker Institute of Nuclear Physics*
Ronald Ransome	*Rutgers University*
Brian Raue	*Florida International University*
Juerg Reinhold	*Florida International University*
Bodo Reitz	*Jefferson Laboratory*
Yves Roblin	*Jefferson Laboratory*
Rikki Roche	*Florida State University*
Mike Roedelbronn	*University of Illinois*
Oscar Rondon	*University of Virginia*

Guenther Rosner	*University of Glasgow*
David Rowntree	*Massachusetts Institute of Technology*
Gary Rutledge	*TRIUMF*
Marat Rvachev	*Massachusetts Institute of Technology*
Franck Sabatie	*DAPNIA/SPhN, CEA, Saclay*
Arun Saha	*Jefferson Laboratory*
Teijiro Saito	*Tohoku University*
Adam J. Sarty	*Saint Mary's University*
Ralph Segel	*Northwestern University*
Albert Shahinyan	*Yerevan Physics Institute*
Simon Sirca	*Massachusetts Institute of Technology*
Karl Slifer	*Temple University*
Timothy Smith	*University of New Hampshire*
Patricia Solvignon	*Temple University*
Pavel Sorokin	*Kharkov State University*
Paul A. Souder	*Syracuse University*
Steffen Strauch	*George Washington University*
Riad Suleiman	*Massachusetts Institute of Technology*
Vincent Sulkovsky	*College of William and Mary*
Jeff Templon	*NIKHEF*
Tatsuo Terasawa	*Tohoku University*
Luminita Todor	*Carnegie Mellon University*
H. Tsubota	*Tohoku University*
Hiroaki Ueno	*Yamagata University*
Paul E. Ulmer	*Old Dominion University*
Guido Urciuoli	*NFN/Sezione Sanità*
Antonin Vacheret	*DAPNIA/SPhN, CEA, Saclay*
Luc Van de Hoorebeke	*Gent State University*
Robert Van de Vyver	*Gent State University*
Pascal Vernin	*DAPNIA/SPhN, CEA, Saclay*
Branislav Vlahovic	*North Carolina Central University*
Hakob Voskanyan	*Yerevan Physics Institute*
Eric Voutier	*Institut des Sciences Nucléaires, Grenoble*
Richard Walter	*Duke University*
Kebin Wang	*University of Virginia*
John Watson	*Kent State University*
Dan Watts	*University of Glasgow*
Larry Weinstein	*Old Dominion University*
Richard Wilson	*Harvard University*
Krishni Wijesooriya	*Argonne National Laboratory*
Bogdan Wojtsekhowski	*Jefferson Laboratory*

Hong Xiang	*Massachusetts Institute of Technology*
Feng Xiong	*Massachusetts Institute of Technology*
Wang Xu	*Massachusetts Institute of Technology*
Jianguo Zhao	*General Electric*
Xiaochao Zheng	*Massachusetts Institute of Technology*
Zilu Zhou	*Massachusetts Institute of Technology*
Jindong Zhu	*Massachusetts Institute of Technology*
Lingyan Zhu	*Massachusetts Institute of Technology*
Xiaofeng Zhu	*College of William and Mary*
Piotr Zolnierczuk	*University of Kentucky*

Publications

7 Publications

7.1 Journals

i) Polarization measurements in neutral pion photoproduction
K. Wijesooriya *et al.*, Physical Review **C 66** (2002) 034614.

ii) Measurement of G_{E_p}/G_{M_p} in $\vec{e}p \longrightarrow e\vec{p}$ to $Q^2 = 5.6$ GeV^2
O. Gayou *et al.*, Physical Review Letters **88** (2002) 092301.

iii) First electron beam polarization measurements with a Compton polarimeter at Jefferson Laboratory
M. Baylac *et al.*, Physics Letter **B 539** (2002) 8.

iv) ^{2}H(e,e′p)n reaction at high recoil momenta
P. Ulmer *et al.*, Physical Review Letters **89** (2002) 062301.

7.2 Hall A Internal Reports

i) Optics calibration of the Hall A High Resolution Spectrometers using the C optimizer
N. Liyanage, **JLAB-TN-02-012** (2002).

ii) Systematic uncertainties in E89-003: a report to the Hall A Collaboration
K. Fissum and P. Ulmer, **JLAB-TN-02-015** (2002).

iii) High luminosity operation of a large solid angle neutron detector array in Jefferson Lab's Hall A
C.C. Chang, O. Filoti, D.W. Higinbotham, C.W. de Jager, E. Jans, M. Jones, R. Lindgren, P. Markowitz, R. Michaels, E. Piasetzky, A. Shahinyan, S. Sirca, K. Wang, J. Watson, K. Wijesooriya, B. Wojtsekhowski, S. Wood, I. Yaron and L. Zhu, **JLAB-TN-02-018** (2002).

iv) A lead fluoride calorimeter for Hall A
K. McCormick and S. Nanda, **JLAB-TN-02-030** (2002).

v) Calibration of spectrometer central angles using Hall A HRS in ^{1}H(e,e′p)
H. Ibrahim, P. Ulmer and N. Liyanage, **JLAB-TN-02-032** (2002).

Conferences

8 Conferences

i) Few-body form factor measurements in Hall A of Thomas Jefferson National Accelerator Facility
Kathy McCormick, *XVIIIth Winter Workshop on Nuclear Dynamics*, Nassau (Bahamas), January 20-27, 2002.

ii) Nucleon electromagnetic form factors
Ed Brash, *IXth International Conference on the Structure of Baryons*, Jefferson Lab (Newport-News, Virginia, USA), March 3-8, 2002.

iii) The spin structure of the neutron and ^{3}He at low Q^2 and the extented GDH sum rule
Gordon Cates, *IXth International Conference on the Structure of Baryons*, Jefferson Lab (Newport-News, Virginia, USA), March 3-8, 2002.

iv) Virtual Compton scattering
Helene Fonvieille, *IXth International Conference on the Structure of Baryons*, Jefferson Lab (Newport-News, Virginia, USA), March 3-8, 2002.

v) Virtual Compton scattering: preliminary results from Jefferson Lab
Luc van Hoorebeke, *IXth International Conference on the Structure of Baryons*, Jefferson Lab (Newport-News, Virginia, USA), March 3-8, 2002.

vi) Deuteron photodisintegration at high momentum transfer
Xiaodong Jiang, *IXth International Conference on the Structure of Baryons*, Jefferson Lab (Newport-News, Virginia, USA), March 3-8, 2002.

vii) Results of exclusive kaon electro-production
Pete Markowitz, *IXth International Conference on the Structure of Baryons*, Jefferson Lab (Newport-News, Virginia, USA), March 3-8, 2002.

viii) Polarization transfer in the ^{4}He($\vec{e}$,e$'\vec{p}$)^{3}He reaction
Steffen Strauch, *IXth International Conference on the Structure of Baryons*, Jefferson Lab (Newport-News, Virginia, USA), March 3-8, 2002.

ix) Virtual Compton scattering and neutral pion electro-production from the proton in the nucleon resonance region
Luminita Todor, *IXth International Conference on the Structure of Baryons*, Jefferson Lab (Newport-News, Virginia, USA), March 3-8, 2002.

x) Bound nucleon properties through ^{3}He(e,e$'$p) at high Q^2
Emilie Penel-Nottaris, *European Workshop on the QCD Structure of the Nucleon*, Ferrara (Italy), April 3-6, 2002.

xi) Measurement of the neutron electric form factor G_E^n at high Q^2
Kathy McCormick, *Workshop on Testing QCD through Spin Observables in Nuclear Targets*, Charlottesville (Virginia, USA), April 18-20, 2002.

xii) Precision measurement of the neutron asymmetry A_1^n in the valence quark region
Xiaochao Zheng, *Workshop on Testing QCD through Spin Observables in Nuclear Targets*, Charlottesville (Virginia, USA), April 18-20, 2002.

xiii) Measurement of the extented GDH sum of the neutron at low Q^2 with polarized ^{3}He target
Seonho Choi, *Spring Meeting of the American Physical Society*, Albuquerque (New Mexico,USA), April 20-23, 2002.

xiv) Search for higher twist effects in the spin structure function $g_2^n(x, Q^2$
Kevin Kramer, *Spring Meeting of the American Physical Society*, Albuquerque (New Mexico,USA), April 20-23, 2002.

xv) Proton elastic form factor ratio by recoil polarization at Q^2 of 5.6 GeV^2
Vina Punjabi, *Spring Meeting of the American Physical Society*, Albuquerque (New Mexico,USA), April 20-23, 2002.

xvi) Probing the $N \to \Delta$ transition via measurements of the polarization responses in the $^1H(\vec{e},e'\vec{p})\pi^0$ reaction
Adam Sarty, *Spring Meeting of the American Physical Society*, Albuquerque (New Mexico,USA), April 20-23, 2002.

xvii) Precise measurement of quasielastic transverse asymmetry and neutron magnetic form factor G_M^n from $\overrightarrow{^3He}(\vec{e},e')$
Wang Xu, *Spring Meeting of the American Physical Society*, Albuquerque (New Mexico,USA), April 20-23, 2002.

xviii) Polarization measurements in π^0 photo-production
Krishni Wijesooriya, *Spring Meeting of the American Physical Society*, Albuquerque (New Mexico,USA), April 20-23, 2002.

xix) Precision measurement of the neutron asymmetry A_1^n at large Bjorken x
Xiachao Zheng, *Spring Meeting of the American Physical Society*, Albuquerque (New Mexico,USA), April 20-23, 2002.

xx) Neutron spin structure experiments at Jefferson Lab
Piotor Zolnierczuk, *X^{th} International Workshop on Deep Inelastic Scattering*, Cracow (Poland), April 30 - May 4, 2002.

xxi) Probing the deuteron at high-T
Ron Gilman, *Workshop on Exclusive Processes at High Momentum Transfer*, Jefferson Lab (Newport-News, Virginia, USA), May 15-18, 2002.

xxii) Proton elastic form factor ratio
Charles Perdrisat, *Workshop on Exclusive Processes at High Momentum Transfer*, Jefferson Lab (Newport-News, Virginia, USA), May 15-18, 2002.

xxiii) Proton polarization in neutral pion photo-production
Krishni Wijesooriya, *Workshop on Exclusive Processes at High Momentum Transfer*, Jefferson Lab (Newport-News, Virginia, USA), May 15-18, 2002.

xxiv) Kaon electro-production on protons at JLab in Hall A
Mauro Iodice, *VIIth Conference on Electron-Nucleus Scattering*, Marciana Marina - Isola d'Elba (Italy), June 24-28, 2002.

xxv) Proton knock-out in Hall A
Kees de Jager, *VIIth Conference on Electron-Nucleus Scattering*, Marciana Marina - Isola d'Elba (Italy), June 24-28, 2002.

xxvi) Proton elastic form factor: the JLab data
Charles Perdrisat, *VIIth Conference on Electron-Nucleus Scattering*, Marciana Marina - Isola d'Elba (Italy), June 24-28, 2002.

xxvii) An electron-ion collider based at CEBAF
Kees de Jager, *IInd International Symposium on the Gerasimov-Drell-Hearn Sum Rule and the Spin Structure of the Nucleon*, Genova (Italy), July 3-6, 2002.

xxviii) Spin structure of the neutron at low Q^2
Karl Slifer, *IInd International Symposium on the Gerasimov-Drell-Hearn Sum Rule and the Spin Structure of the Nucleon*, Genova (Italy), July 3-6, 2002.

xxix) Real Compton scattering on the proton
Bogdan Wojtsekhowski, *IInd International Symposium on the Gerasimov-Drell-Hearn Sum Rule and the Spin Structure of the Nucleon*, Genova (Italy), July 3-6, 2002.

xxx) Photopion production at Jefferson Lab
Haiyan Gao, *IInd Asia Pacific Conference on Few-Body in Physics*, Shanghai (China), August 27-30, 2002.

xxxi) Neutron spin structure with polarized ^{3}He at Jefferson Lab Hall A
Ron Gilman, *IInd Asia Pacific Conference on Few-Body in Physics*, Shanghai (China), August 27-30, 2002.

xxxii) Polarization measurements in π^0 photo-production from the proton
Ron Gilman, *IInd Asia Pacific Conference on Few-Body in Physics*, Shanghai (China), August 27-30, 2002.

xxxiii) Detailed study of the few nucleon systems at Jefferson Lab
Arun Saha, *IInd Asia Pacific Conference on Few-Body in Physics*, Shanghai (China), August 27-30, 2002.

xxxiv) Few-body (e,e′p) and (e,e′d) experiments in Jefferson Lab Hall A
Douglas Higinbotham, *XVIIIth European Conference on Few-Body Problems in Physics*, Bled (Slovenia), September 8-14, 2002.

xxxv) Measuring G_E^n at high momentum transfers
Bodo Reitz, *XVth International Spin Physics Symposium*, Brookhaven National Laboratory, Upton (New York, USA), September 9-14, 2002.

xxxvi) Proton elastic form factor ratio: the JLab polarization experiments
Charles Perdrisat, *XVth International Spin Physics Symposium*, Brookhaven National Laboratory, Upton (New York, USA), September 9-14, 2002.

xxxvii) The study of ^{3}He nucleus in perpendicular kinematics at high momenta
Konrad Aniol, *XVIth International Conference on Particles and Nuclei*, Osaka (Japan), September 30 - October 4, 2002.

xxxviii) Virtual Compton scattering and the generalized polarizabilities of the proton
Charles Hyde-Wright, *Fall Meeting of the Division of Nuclear Physics - American Physical Society*, National Superconducting Cyclotron Laboratory, East Lansing (Michigan, USA), October 9-12, 2002.

xxxix) Experimental study of nuclear few-body systems at Jefferson Lab
Arun Saha, *CFIF Fall Workshop on Nuclear Dynamics from Quarks to Nuclei*, Lisbon (Portugal), October 31 - November 2, 2002.

Thesis

9 Thesis

i) Extractions of proton form factors with ratio constraint
Shaohong Li, University of Regina, April 2002.

ii) Polarization transfer in the reaction ^{4}He($\vec{e}$,e'$\vec{p}$)^{3}H in the quasielastic scattering region
Sonja Dieterich, The State University of New Jersey, May 2002.

iii) A precision measurement of the transverse asymmetry A_{T^v} from quasi-elastic $\overrightarrow{^3\mathrm{He}}(\vec{e},e')$ process, and the neutron magnetic form factor G_m^n at low Q^2
Wang Xu, Massachusetts Institute of Technology, June 2002.

iv) Precision measurement of the spin-dependent asymmetry in the threshold region of quasielastic $\overrightarrow{^3\mathrm{He}}(\vec{e},e')$
Feng Xiong, Massachusetts Institute of Technology, September 2002.